UNIVERSITAT POLITÈCNICA DE VALÈNCIA

DEPARTAMENT DE COMUNICACIONS
Photonics Research Labs. (PRL)

Encoding optical FBG sensors to enhance the capacity of optical sensing systems

Ph.D. THESIS

by
Andrés Triana

Advisors:
PhD. Margarita Varón
PhD. Daniel Pastor Abellán

Valencia, July 2018

A mi familia.

There is a crack in everything,

that's how the light gets in.

Leonard Cohen.

Agradecimientos

Quiero dedicar esta pequeña sección para agradecer a todos aquellos que me han acompañado durante los últimos años, a quienes de una u otra manera han contribuido a la elaboración de este trabajo, a todos ¡muchas gracias!.

En primer lugar, agradezco a mis directores de tesis: Margarita y Daniel. Quienes siempre se preocuparon por guiar, a través de su ejemplo, mi camino en la investigación. Agradezco infinitamente el tiempo que han dedicado a enseñarme, la paciencia con que lo han hecho y la pasión por la investigación que han infundido en mí. Ha sido un verdadero privilegio aprender junto a ustedes y ver lo emocionante que puede llegar a ser la investigación, inclusive para quienes tienen sobre sus hombros una gran trayectoria.

Agradezco a todos los integrantes del Photonics Research Labs. grupo en el cual realicé gran parte de esta tesis. Todos, desde Daniel Pastor, quien me dio la oportunidad de ser parte de este prestigioso grupo, hasta los demás catedráticos que trabajan por dar continuidad al altísimo nivel de calidad del grupo. Sin olvidar por supuesto a todos los compañeros de estudio y de laboratorio, quienes me ofrecieron su ayuda y su amistad, Gloria, Luis, Rocío, Manuel, Dani, Jesús, Javi, Demetrio, Javi, Bernie, Joaquín y a todos los que me puedan faltar, ¡gracias!.

Agradezco igualmente al grupo de investigación CMUN en la Universidad Nacional de Colombia, que me dio la oportunidad de empezar en la investigación y me ha apoyado desde mi trabajo de maestría hasta ahora. A su directora, Margarita Varón, quien ha logrado consolidar un grupo de investigación en el

que prevalezca la calidad, apostando siempre por el desarrollo de la investigación en el país. Debo agradecer también a todos mis compañeros del grupo: Camilo, Monica, Santi, David, Sergio, Juan, Germán; gracias por su compañía y el buen ambiente que se tiene siempre en el grupo.

Agradezco también al programa de doctorado nacional de Colciencias (Conv. 567) por hacer posible este trabajo.

Por último quiero agradecer especialmente a mi grupo de amigos cercanos (Angie, Alejo, Jamer, Carlitos, V, Jorge, Anita, Sergio), que siempre han estado ahí para escucharme, a toda mi familia que me ha brindado su apoyo incondicional, a Sandra que también ha sabido acompañarme y brindarme su confianza durante estos años, y por supuesto a mis padres y hermanos que son la mejor motivación que he podido tener y el mejor apoyo en todo momento.

Abstract

This thesis investigates the application of encoding concepts to the design of optical sensors based on fiber Bragg grating (FBG) devices. Specifically, we present the design, characterization and experimental validation of custom encoded sensing devices that can be designed and manufactured as super-structured FBG (SSFBG) devices.

The aim of this thesis is to enhance the capacity and the overall performance of the optical sensing systems based on conventional FBG sensors. To do so, three encoding methodologies of SSFBG sensing devices have been proposed, aiming to endow each sensor with additional information useful to identify each sensor even under overlapping conditions. An encoded FBG-based sensor is a FBG structure whose shape has been tailored after an orthogonal codeword in such a way that their central wavelength can be distinguished unequivocally from other signals in the spectrum.

The design of encoded SSFBG sensors is performed by modifying the reflection spectrum of multi-band FBG devices, this is achieved by translating orthogonal codewords into the amplitude and phase terms of the FBG sensors.

Amplitude encoding of SSFBG sensors consists in translating the binary optical orthogonal codewords (OOCs), developed for optical-code division multiple-access (OCDMA) communications systems, into the reflection pattern of the devices.

Amplitude & phase encoding has been proposed in two different approaches: in the first one, custom amplitude and phase codewords (a_k, f_k) were specifically devised to exhibit orthogonal behavior by combining the two codewords. The dual-wavelength tunable interrogation technique was also specifically designed to retrieve the differential measurement of the sensors and effectively decode their information. The second approach uses the discrete prolate spheroidal sequences (DPSS), which are mutually orthogonal sequences developed for communications systems. We demonstrated the use of this structures as orthogonal sensing elements with definite phase and amplitude patterns.

The manufacturing and experimental validation of the proposed SSFBG devices were carried out to prove the overlap-proof performance of the devices. The central wavelength of the sensors is successfully retrieved in the three methodologies, additionally, the error of the sensing system was characterized in terms of the design parameters.

Resumen

Esta tesis investiga la aplicación de conceptos de codificación al diseño de sensores ópticos basados en redes de difracción de Bragg de Bragg (FBG). Específicamente, se presenta el diseño, la caracterización y la validación experimental de dispositivos de detección codificados personalizados que se pueden diseñar y fabricar como dispositivos FBG súper estructurados (SSFBG).

El objetivo de esta tesis es mejorar la capacidad y el rendimiento general de los sistemas de detección óptica basados en sensores FBG convencionales. Para ello, se han propuesto tres metodologías de codificación de dispositivos de detección SSFBG, con el objetivo de dotar a cada sensor con información adicional útil para la identificación de cada sensor incluso en condiciones de superposición. Un sensor codificado basado en FBGs es una estructura FBG cuya forma se ha adaptado a una palabra-código ortogonal, de tal manera que su longitud de onda central se puede distinguir inequívocamente de otras señales en el espectro.

El diseño de los sensores SSFBG codificados se realiza modificando el espectro de reflexión de dispositivos FBG multibanda, esto se logra traduciendo las palabras-código ortogonales en los términos de amplitud y fase de los sensores FBG.

La codificación en amplitud de los sensores SSFBG consiste en traducir las palabras-código *"Optical Orthogonal Codewords"* (OOC), desarrolladas para sistemas de comunicaciones de acceso múltiple por división de código óptico (OCDMA), en el patrón de reflexión de los dispositivos.

La codificación en amplitud y fase se ha propuesto mediante dos enfoques diferentes: en el primero, palabras-código de amplitud y fase personalizadas (a_k, f_k) fueron diseñadas específicamente para exhibir un comportamiento ortogonal obtenido por la combinación de dos palabras-código. La técnica de interrogación basada en una fuente dual sintonizable fue específicamente diseñada para recuperar la medición diferencial de los sensores y decodificar efectivamente su información. El segundo enfoque utiliza las secuencias *"Discrete Prolate Spheroidal Sequences"* (DPSS), que son secuencias mutuamente ortogonales desarrolladas para sistemas de comunicaciones. Se demostró el uso de estas estructuras como elementos de detección ortogonales con patrones específicos de fase y amplitud.

La fabricación y validación experimental de los dispositivos SSFBG propuestos se realizaron para demostrar el rendimiento de los sensores inclusive en condiciones de superposición espectral. La longitud de onda central de los sensores se recupera con éxito en las tres metodologías, además, el error del sistema de detección se caracterizó en términos de los parámetros de diseño.

Resum

Esta tesi investiga l'aplicació de conceptes de codificació al disseny de sensors òptics basats en xarxes de difracció de Bragg de Bragg (FBG) . Específicament, es presenta el disseny, la caracterització i la validació experimental de dispositius de detecció codificats personalitzats que es poden dissenyar i fabricar com a dispositius FBG súper estructurats (SSFBG) .

L'objectiu d'esta tesi és millorar la capacitat i el rendiment general dels sistemes de detecció òptica basats en sensors FBG convencionals. Per a això, s'han proposat tres metodologies de codificació de dispositius de detecció SSFBG, amb l'objectiu de dotar a cada sensor amb informació addicional útil per a la identificació de cada sensor inclús en condicions de superposició. Un sensor codificat basat en FBGs és una estructura FBG la forma de la qual s'ha adaptat a una paraula-codi ortogonal, de tal manera que la seua longitud d'ona central es pot distingir inequívocament d'altres senyals en l'espectre.

El disseny dels sensors SSFBG codificats es realitza modificant l'espectre de reflexió de dispositius FBG multibanda, açò s'aconseguix traduint les paraules-codi ortogonals en els termes d'amplitud i fase dels sensors FBG.

La codificació en amplitud dels sensors SSFBG consistix a traduir les paraules-codi extit *"Optical Orthogonal Codewords"* (OOC) , desenrotllades per a sistemes de comunicacions d'accés múltiple per divisió de codi òptic (OCDMA) , en el patró de reflexió dels dispositius.

La codificació en amplitud i phase s'ha proposat per mitjà de dos enfocaments diferents: en el primer, paraules-codi d'amplitud i fase personalitzades (a_k, f_k) van ser dissenyades específicament per a exhibir un comportament ortogonal obtingut per la combinació de dos paraules-codi. La tècnica d'interrogació basada en una font dual sintonizable va ser específicament dissenyada per a recuperar el mesurament diferencial dels sensors i descodificar efectivament la seua informació. El segon enfocament utilitza les seqüències *"Discrete Prolate Spheroidal Sequences"* (DPSS), que són seqüències mútuament ortogonals desenrotllades per a sistemes de comunicacions. Es va demostrar l'ús d'estes estructures com a elements de detecció ortogonals amb patrons específics de fase i amplitud.

La fabricació i la validació experimental dels dispositius SSFBG proposats es van realitzar per a demostrar el rendiment dels sensors inclusivament en condicions de superposició espectral. La longitud d'ona central dels sensors es recupera amb èxit en les tres metodologies, a més, l'error del sistema de detecció es va caracteritzar en termes dels paràmetres de disseny.

List of Figures

List of Tables

Contents

6 Conclusions and future work   115

Chapter 1

Thesis overview

1.1 Background

One of the biggest discoveries in the recent decades is without a doubt the optical fiber. Optical fibers, in principle seen as a low-loss waveguide, revolutionized the telecommunications field by increasing the quality and capacity of information transmission. Later, the invention of optical fiber active devices such as lasers and amplifiers potentiated the field, allowing the implementation of fiber based opto-electronic systems reducing the losses related to light coupling between bulk components and fiber waveguides. However, a major breakthrough in the opto-electronics field came after the discovery of photosensitivity in optical fibers with the invention of a new in-fiber device called the *Fiber Bragg Grating (FBG)*. An FBG is a very functional device, created inside the optical fiber thanks to its photo-sensitivity. FBGs allowed to perform filtering and reflection tasks with high efficiency and reducing the use of bulk components and therefore the losses in the system. For instance, FBGs are used as selective filters in communications setups, as de/multiplexers in wavelength division multiplexing (WDM), chirped FBGs are used to compensate the group delay in transmission links; among other functions we can name also optical processing, pulse shaping, or mode locking; functions that are very common and important in telecommunications.

FBGs have then revolutionalized the telecommunications field but since their invention they have been also considered to potentially work in sensing systems, which is where this thesis work is focused. FBG sensors have many advantages over their electronics peers: they are light weighted, small sized, immune to electromagnetic interferences EMI, able to work under high radiation environments and have linear response with low insertion losses, moreover they are naturally multiplexed in wavelength so that a number of sensors can be arranged in a single optical fiber. Therefore FBG sensors have been widely investigated and even implemented in high tech engineering projects to assess civil structures health for example, or to instrument the aerospace and oil & gas industries [1], [2].

The wavelength detection in optical sensing systems plays a key role in the design and usability of the FBG sensing systems. Consequently, many interrogation setups and multiplexing techniques have been studied [3]. Regarding interrogation setups, the most popular approaches are: *passive filters* [4], where the main idea is to map the wavelength variation of the FBG sensors to a power shift. This is achieved by placing the cut-off wavelength of the filter near to the sensor resonance. *Active filters* are also employed [5]–[10], in this system the filter is swept over the working range of the sensors in order to detect the position of the reflected wavelength. The analogue approach would be the use of *tunable sources* [11], [12], which are also swept over the operational spectrum of the sensors detecting the wavelength position of the sensors. Several additional interrogation setups have been also proposed, see for example [13]–[19], from which it is worth mentioning that a couple of proposals do include code division multiplexing (CDM) concepts in the interrogation of FBG sensors. The approach employed in [18], [19] employs codification in the sense that it modulates/encodes the LED source, using a PRBS (Pseudo-Random Binary Sequence) generator; then, it synchronizes the encoded source with the reflection spectrum from each sensing element in the array in order to perform the correlation between the sent and retrieved patterns. Once they have correlated the sent and retrieved signal from each sensor, they map the correlation amplitude to the given change in the FBG wavelength obtaining a measure of the environmental variable over the FBG device. The advantage of this method relies in that it discriminates signals from various FBG sensors while avoiding the utilization of a tunable source, reducing the cost of the system.

Equally important in sensing systems are the multiplexing techniques, which are basically the architecture of the sensing network. For 'conventional' FBG sensors these architectures are basically divided into wavelength division- and time division-multiplexing (WDM, TDM). WDM is the natural multiplexing

scheme of FBG sensors because it consists on allocating a given wavelength spectrum to each sensor in the spectrum in order to prevent overlapping between them. TDM, on the contrary, is based on detecting each sensor signal depending on their arrival time to the interrogation system. Therefore, WDM approaches use a broadband source to illuminate the sensing array, while TDM techniques require a pulsed signal. Also used is the combination of these multiplexing methodologies, for instance WDM+TDM have been used to increase the number of sensors interrogated, and with the same purpose it has been proposed the use of WDM and TDM combined with spatial multiplexing (SDM). These approaches are practically realizable even when they increase considerably the complexity of the interrogation system.

With time, the manufacturing process for the FBG devices have matured and therefore more versatile devices are realizable. A perfect example of this is the super structure Bragg grating (SSFBG), which is a grating structure fabricated as a modulation of the refractive index of the optical fiber [20]. With this kind of device, it is possible to construct different and complex reflection profiles (manipulating the reflection strength and the phase-shift over the device bandwidth). SSFBGs with intricate reflection spectra have been manufactured for instance to be used in optical code division multiple access (OCDMA) systems [21], [22]. In such approaches, SSFBG devices are used to en/decode the information transmitted through a communications link.

1.2   Motivation and Thesis Structure

In order to improve functionality of the optical sensing networks, it is expected to deploy the highest possible number of sensors, reducing the overall cost of the system from the point of view of price per sensing element. WDM and TDM multiplexing techniques have been historically exploited to overcome this. It is also desired to solve the problem of overlapping sensors (When two sensor wavelengths overlap, conventional detection systems are unable to track them down, leading to wrong measurements and referencing problems in the system). The proposed approaches regarding this, are decision algorithms that try to weigh the possible contributions of two sensors to the overlapped measurement. This is done through bio-inspired computational algorithms that often have to be trained and are computationally consuming.

Chapter 2 is an introduction to the main concepts regarding fiber Bragg grating sensors. Their theoretical description is provided along with their synthesis method. Also, the manufacturing and wavelength detection processes are de-

scribed. In the following paragraphs, the main contributions of this thesis are listed and framed inside the thesis structure.

In this thesis, generally, we propose the use of encoding concepts borrowed from communications systems to compose the shape of FBG sensors in order to endow each sensor with additional information. The encoding of the sensors makes it possible to identify each sensor in the network, even under overlapping conditions between them. In this way, a solution is offered to the above problems: as the sensors are mutually orthogonal between them, they can be detected even when they are totally overlapped. And, as a consequence, more sensors can be allocated in the sensing network, see illustration in Figure 1.1, since a combination between our Code Division Multiplexing (CDM) technique and conventional WDM, TDM approaches can be achieved. Figure 1.1 shows a general description of our CDM-WDM approach. The conventional scenario is depicted in the upper plot: a number N of conventional FBG sensors are allocated in the available spectrum. Each sensor has a working wavelength range $(\Delta\lambda_{Bn})$, and a guard-band $(\Delta\lambda_{GB})$ is necessary between the sensors to prevent overlapping. The lower part of the Figure represents the proposed CDM-WDM approach, where the working range and the guard-bands can be maintained, being the difference that each sensor is designed with an orthogonal shape regarding its neighboring sensors. Hence, overlapping is allowed between the orthogonal sensors and consequently it is possible to double or triple the number of sensors interrogated in a sensing network by using simple codewords families with two or three members as we will prove further in this work.

Particularly, we have first explored the amplitude encoding of FBG devices. In Chapter 3, a family of optical orthogonal codewords (OOCs) was proposed to shape the super structured FBG devices. In such an approach, the codeword length is directly related to the total bandwidth of the sensor so the smallest possible codewords were selected. Considerations regarding the manufacturing and practical feasibility of the sensors were analyzed through simulation. Also simulated was the detection process of the sensors, which is based on the correlation properties inherent to the codewords. Finally, a set of amplitude encoded SSFBG devices was manufactured and experimentally validated to allow detection of the sensors under the overlapping scenarios. The sensing system is also characterized to the point of isolating the error produced by the addition of overlapping sensors. The experimental results show very little error obtained at the expense of doubling the capacity of the system.
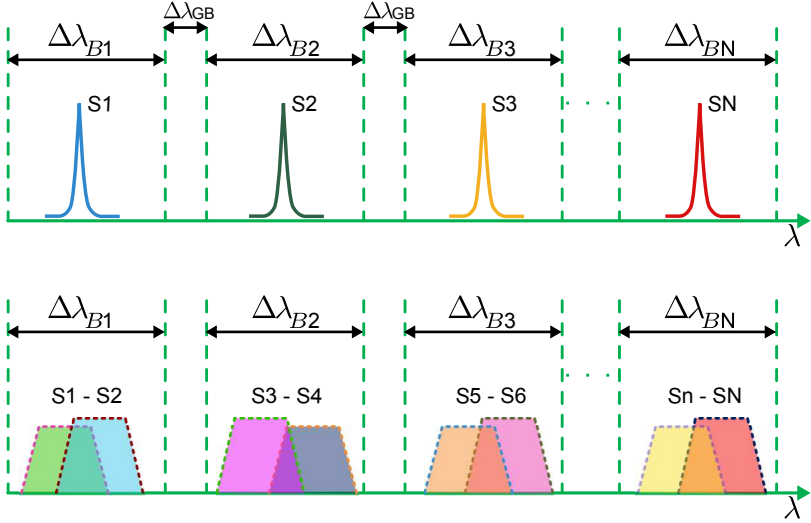
Figure 1.1: A representation of a CDM-WDM combined multiplexing scenario is presented. In this example, by assigning each pair of sensors with orthogonal shapes, the overlapping between each pair is allowed. Therefore the operational spectrum allocated for each sensor could be shared and the number of sensors in the array could be doubled.

Chapter 4, shows how, by including two variables in the design of the codewords, the correlation properties of the SSFBG sensors are enhanced, this helps to reduce the interference between multiple sensing elements in the system and therefore to minimize the error induced due to the overlapping between the sensors. We have proposed here the combination of amplitude and phase codewords to design a set of three sensors. The complex encoding of the sensors comes along with a specific interrogation setup, based on the use of a dual-wavelength tunable source, able to perform differential decoding of the manufactured devices. This approach was also experimentally validated, accomplishing the manufacturing and detection goals.

The differential interrogation setup proposed in this thesis is able to retrieve the magnitude and phase responses of intricate optical devices in a scanning-way (common to sensing systems). In Chapter 5 we have therefore demonstrated the approach versatility to successfully interrogate a set of sensors based on the discrete prolate spheroidal sequences. Which are complex structures with very definite phase and amplitude patterns.

In the final Chapter the summary of the thesis is provided as well as some remarks regarding the future work.

References

[1] X. Qiao, Z. Shao, W. Bao, and Q. Rong, "Fiber bragg grating sensors for the oil industry", *Sensors*, vol. 17, no. 3, 2017, ISSN: 1424-8220. DOI: `10.3390/s17030429` (cit. on p. 2).

[2] J. Johny, R. Prabhu, W. K. Fung, and J. Watson, "Investigation of positioning of fbg sensors for smart monitoring of oil and gas subsea structures", in *OCEANS 2016 - Shanghai*, Apr. 2016, pp. 1–4. DOI: `10.1109/O CEANSAP.2016.7485662` (cit. on p. 2).

[3] A. Othonos and K. Kalli, *Fiber Bragg Gratings: Fundamentals and Applications in Telecommunications and Sensing*, ser. Artech House optoelectronics library. Artech House, 1999, ISBN: 9780890063446 (cit. on p. 2).

[4] S. M. Melle, K. Liu, and R. M. Measures, "A passive wavelength demodulation system for guided wave bragg grating sensors", *IEEE Photonics Technology Letters*, vol. 4, no. 5, pp. 516–518, May 1992, ISSN: 1041-1135. DOI: `10.1109/68.136506` (cit. on p. 2).

[5] A. D. Kersey, T. A. Berkoff, and W. W. Morey, "Multiplexed fiber bragg grating strain sensor system with a fiber fabry perot wavelength filter", *Opt. Lett.*, vol. 18, no. 16, pp. 1370–1372, Aug. 1993. DOI: `10.1364/OL .18.001370` (cit. on p. 2).

[6] M. A. Davis, D. G. Bellemore, M. A. Putnam, and A. D. Kersey, "Interrogation of 60 fibre bragg grating sensors with microstrain resolution capability", *Electronics Letters*, vol. 32, no. 15, pp. 1393–1394, Jul. 1996, ISSN: 0013-5194. DOI: `10.1049/el:19960908` (cit. on p. 2).

[7] M. G. Xu, H. Geiger, J. L. Archambault, L. Reekie, and J. P. Dakin, "Novel interrogating system for fibre bragg grating sensors using an acousto optic tunable filter", *Electronics Letters*, vol. 29, no. 17, pp. 1510–1511, Aug. 1993, ISSN: 0013-5194. DOI: `10.1049/el:19931006` (cit. on p. 2).

[8] H. Geiger, M. G. Xu, N. C. Eaton, and J. P. Dakin, "Electronic tracking system for multiplexed fibre grating sensors", *Electronics Letters*, vol. 31, no. 12, pp. 1006–1007, Jun. 1995, ISSN: 0013-5194. DOI: `10.1049/el :19950641` (cit. on p. 2).

[9]   D. A. Jackson, A. B. L. Ribeiro, L. Reekie, and J. L. Archambault, "Simple multiplexing scheme for a fiber optic grating sensor network", *Opt. Lett.*, vol. 18, no. 14, pp. 1192–1194, Jul. 1993. DOI: 10.1364/OL.18.001192 (cit. on p. 2).

[10]   G. Brady, S. Hope, A. Ribeiro, D. Webb, L. Reekie, J. Archambault, and D. Jackson, "Demultiplexing of fibre bragg grating temperature and strain sensors", *Optics Communications*, vol. 111, no. 1, pp. 51–54, 1994, ISSN: 0030-4018 (cit. on p. 2).

[11]   B. Van Hoe, G. Lee, E. Bosman, J. Missinne, S. Kalathimekkad, O. Maskery, D. J. Webb, K. Sugden, P. Van Daele, and G. Van Steenberge, "Ultra small integrated optical fiber sensing system", *Sensors*, vol. 12, no. 9, pp. 12 052–12 069, Sep. 2012, ISSN: 1424-8220. DOI: 10.3390/s120912052 (cit. on p. 2).

[12]   T. Mizunami, S. Hirose, T. Yoshinaga, and K.-i. Yamamoto, "Power stabilized tunable narrow band source using a vcsel and an edfa for fbg sensor interrogation", *Measurement Science and Technology*, vol. 24, no. 9, p. 094 017, 2013 (cit. on p. 2).

[13]   Y. Sano and T. Yoshino, "Fast optical wavelength interrogator employing arrayed waveguide grating for distributed fiber bragg grating sensors", *Journal of Lightwave Technology*, vol. 21, no. 1, pp. 132–139, Jan. 2003, ISSN: 0733-8724. DOI: 10.1109/JLT.2003.808620 (cit. on p. 2).

[14]   K. P. Koo and A. D. Kersey, "Bragg grating based laser sensors systems with interferometric interrogation and wavelength division multiplexing", *Journal of Lightwave Technology*, vol. 13, no. 7, pp. 1243–1249, Jul. 1995, ISSN: 0733-8724. DOI: 10.1109/50.400692 (cit. on p. 2).

[15]   A. Arie, B. Lissak, and M. Tur, "Static fiber bragg grating strain sensing using frequency locked lasers", *J. Lightwave Technol.*, vol. 17, no. 10, p. 1849, Oct. 1999 (cit. on p. 2).

[16]   T. Guo, C. Chen, A. Laronche, and J. Albert, "Power referenced and temperature calibrated optical fiber refractometer", *IEEE Photonics Technology Letters*, vol. 20, no. 8, pp. 635–637, Apr. 2008, ISSN: 1041-1135. DOI: 10.1109/LPT.2008.919457 (cit. on p. 2).

[17]   M. A. Davis and A. D. Kersey, "Matched filter interrogation technique for fibre bragg grating arrays", *Electronics Letters*, vol. 31, no. 10, pp. 822–823, May 1995, ISSN: 0013-5194. DOI: 10.1049/el:19950547 (cit. on p. 2).

[18]   H. Lee, "Multiple fiber Bragg grating sensor system using code-division multiple access", *Appl. Opt.*, vol. 41, no. 25, pp. 5245–5248, Sep. 2002. DOI: 10.1364/AO.41.005245 (cit. on p. 2).

[19]   H. Ryu, H. Lee, and K.-S. Kim, "An economical and multiple fibre grating sensor system with a rapid response using code division multiple access", *Measurement Science and Technology*, vol. 12, no. 7, p. 906, 2001 (cit. on p. 2).

[20]   B. J. Eggleton, P. A. Krug, L. Poladian, and F. Ouellette, "Long periodic superstructure bragg gratings in optical fibres", *Electronics Letters*, vol. 30, no. 19, pp. 1620–1622, Sep. 1994, ISSN: 0013-5194. DOI: `10.1049/el:19941088` (cit. on p. 3).

[21]   P. C. Teh, P. Petropoulos, M. Ibsen, and D. J. Richardson, "A comparative study of the performance of seven- and 63-chip optical code-division multiple-access encoders and decoders based on superstructured fiber bragg gratings", *Journal of Lightwave Technology*, vol. 19, no. 9, pp. 1352–1365, Sep. 2001, ISSN: 0733-8724. DOI: `10.1109/50.948283` (cit. on p. 3).

[22]   D. Pastor, W. Amaya, and R. Garcia-Olcina, "Design of high reflectivity superstructured fbg for coherent ocdma employing synthesis approach", *Electronics Letters*, vol. 43, no. 15, pp. 824–825, Jul. 2007, ISSN: 0013-5194. DOI: `10.1049/el:20071171` (cit. on p. 3).

Chapter 2

Introduction to fiber Bragg grating devices and applications

Given the deep development in the telecommunications field during the last decades, optical fiber and optical fiber devices have been also widely investigated. One of the most developed and settled optical devices is the fiber Bragg grating (FBG) which carries out filtering and selection tasks in a pretty efficient way. This filtering capacity, combined with their manufacturing and packaging simplicity makes FBG devices a very useful, common component in optoelectronic communications and sensing systems[1], [2].

2.1 Fiber Bragg gratings

A fiber Bragg grating is a disturbance induced inside the optical fiber core of an optical fiber. This disturbance affects the optical fiber refractive index in a periodical fashion. This periodical disturbance, when meeting the Bragg condition, acts as a built-in filter around a fixed wavelength, also called the Bragg wavelength[3]. For an uniform fiber Bragg grating device, i.e. assuming that the optical fiber is entirely mono-mode and does not have any losses at
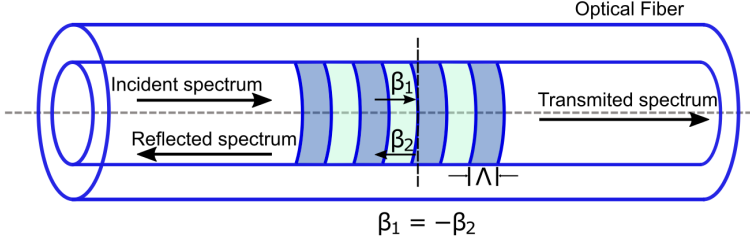
Figure 2.1: Sketch of the mono-mode Bragg grating reflection in a Bragg grating device, the grating condition of coupling between the forward- and counter-propagating modes is satisfied for $m = -1$.

the Bragg wavelength, the Bragg condition has an effect over the incident wavelength defined by the equation (2.1) [4] (see Fig. 2.1).

$$\beta_2 = \beta_1 + m\frac{2\pi}{\Lambda} \tag{2.1}$$

Where β_1, β_2 are the mode propagation constants for the forward- and counter-propagating waves, m is the diffraction order and Λ is the disturbance periodical spacing of the Bragg grating. The propagation constant is defined as: $\beta = \frac{2\pi}{\lambda}\eta_{eff}$ with η_{eff}, the effective refractive index of the optical fiber. Therefore, from equation (2.1), the resonant wavelength for reflection of a mode of index $\eta_{eff,1}$ into a mode of index $\eta_{eff,2}$ is presented in equation (2.2b):

$$\frac{-2\pi\eta_{eff,2}}{\lambda} - \frac{2\pi\eta_{eff,1}}{\lambda} = \frac{-2\pi}{\Lambda} \tag{2.2a}$$

$$\lambda = \Lambda\left(\eta_{eff,1} + \eta_{eff,2}\right) \tag{2.2b}$$

In equation (2.2b) the diffraction order was assumed to be $m = -1$ since we want to represent the coupling between the propagating and the counter-propagating modes, i.e. we consider a mono-mode optical fiber. Therefore we also consider that the two modes are identical ($\eta_{eff,1} = \eta_{eff,2} = \eta_{eff}$) obtaining the familiar Bragg equation ((2.3)):

$$\lambda_B = 2\eta_{eff}\Lambda \tag{2.3}$$
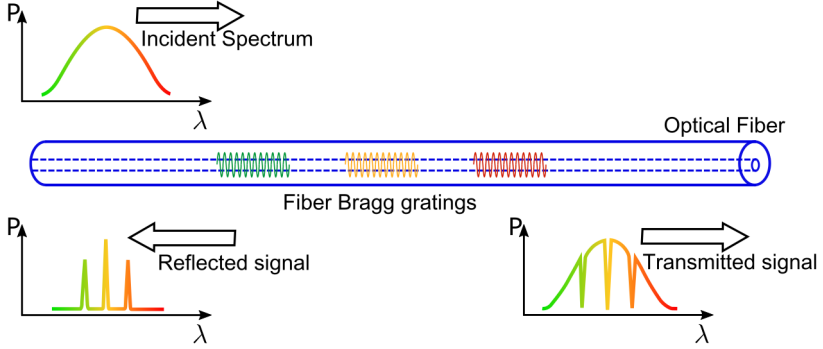
Figure 2.2: Schematic representation of the working principle of fiber Bragg grating devices. Incident light gets diffracted by each Bragg grating, which has a specific wavelength resonance. The reflected spectrum contains the wavelengths matching each Bragg grating while the transmitted spectrum contains all the remaining wavelengths.

Where λ_B is the Bragg wavelength, reflected by the the optical fiber built-in grating. Figure 2.2 shows the working principle of a fiber Bragg grating device, an incident broadband spectrum goes in an optical fiber with three uniform Bragg gratings written along its core, the reflected spectrum comprehends the three wavelengths matching the Bragg condition, while the complementary signal goes through the optical fiber. The analysis of a grating is performed by means of the coupled mode theory [4]–[6], which basically describes the coupling between the forward and backward propagating field envelopes, namely $u(z, \delta)$ and $v(z, \delta)$. In the uniform grating case, the coupled mode equations [7] can be analytically solved by considering constant index modulation and period, so that it can be assumed the boundary conditions $u(0, \delta) = 1$ and $v(L, \delta) = 0$, meaning that the reflected wave is 0 in $L = \delta$, then the reflectivity of an uniform FBG as a function of the grating length L and the wavelength λ is given by (2.4):

$$R(L, \lambda) = \frac{q^2 \sinh^2(\gamma L)}{\Delta\beta^2 \sinh^2(\gamma L) + \gamma^2 \cosh^2(\gamma L)} \tag{2.4}$$

where q is the coupling coefficient, $\beta = 2\pi\eta_0/\lambda$ the propagation constant, $\Delta\beta = \beta - \pi/\Lambda$ the wavelength vector detuning and $\gamma^2 = q^2 - \Delta\beta^2$. Note that at the Bragg wavelength, there is no wave vector detuning $\Delta\beta = 0$ so the reflectivity is $R_{max}(L, \lambda) = \tanh^2(qL)$. In summary, the optical fiber Bragg

grating is defined mainly by three parameters: the Bragg wavelength λ_B, the effective refractive index η_{eff} and the coupling coefficient $q(z)$ (2.5) [8].

$$q(z) = \frac{\pi \Delta \eta_{ac}(z)}{\lambda_B} \exp\left[i \left(\Theta(z) - \frac{4\pi}{\lambda_B} \int_0^z \Delta \eta_{dc}(z') dz' + \frac{\pi}{2} \right) \right] \qquad (2.5)$$

Shown in equation (2.5) is the relationship between the coupling coefficient and the refractive index modulation, the magnitude of the coupling coefficient is proportional to the amplitude of the index modulation (η_{ac}) and the phase is related to the average index change (η_{dc}).

2.1.1 Synthesis of fiber Bragg gratings

The coupling coefficient $q(z)$ describes the refractive index profile along the core of the optical fiber. It has a direct relationship with the reflected spectrum: generally, the modulus of the coupling coefficient $|q(z)|$ determines the amplitude of the grating or index modulation and its phase $\arg q(z)$ provides the grating phase envelope. Thus, regarding equation (2.5), amplitude of the grating is related mainly to the 'ac' component of the refractive index modulation (η_{ac}) and the phase is affected by the average refractive index profile (η_{dc}) and the geometrical phase Θ [9].

The synthesis of fiber Bragg grating devices consists in finding the grating profile, i.e. the complex coupling coefficient $q(z)$, from a given reflection spectrum. Synthesis methods are useful not only to design a Bragg grating from scratch, but also to characterize the manufacturing procedure or evaluate already manufactured devices. Some synthesis approaches are based in the Fourier transform from the weak grating approximation [10], nevertheless this is only an approximation valid for Bragg gratings with reflectivity values lower than $10 - 50\%$, producing large errors for strong gratings. A more convenient approach for performing the synthesis of fiber Bragg gratings is the so called layer peeling method [7], [11], which is an iteration-based method that treats the grating as a discretized stack of complex reflectors ρ_j with $j = 0, 1, \ldots, N$. It is based on causality: it calculates initially the coupling coefficient for the first grating layer, then, consecutively the fields are propagated to the next layer and the algorithm goes to the initial position since the effect of the first layer has been "peeled off", the process is iterated until the entire grating construction.

The layer peeling method is the most direct and simple method to obtain the complex coupling coefficient $q(z)$ of a FBG device, besides it is the only effective mechanism to design FBGs of high reflectivity or complex spectral

shapes. Therefore it is the method used in this thesis work to design the super-structured FBG devices which are composed by more than one reflection band and, they may or may not have discrete phase values distributed along the grating. The design methodology is first focused on the design and spectral definition of the sensors shape, and then the complex coupling profile $q(z)$ for each specific design is obtained and sampled to suite the manufacturing system characteristics.

2.1.2 Sensitivity of fiber Bragg gratings

The dependence of the back reflected wavelength on the effective refractive index and the periodicity of the perturbation makes it possible to use FBGs as sensing devices. The reason for this is that both, the effective refractive index and the periodicity of the Bragg grating, are affected by environmental changes in strain and temperature. The wavelength shift due to temperature and strain is written down in equation (2.6), where the first term describes the wavelength shift due to elongation of the optical fiber Δl, while the second term relates the wavelength shift caused by a temperature change ΔT.

$$\Delta\lambda_B = 2\left(\Lambda\frac{\delta\eta_{eff}}{\delta l} + \eta_{eff}\frac{\delta\Lambda}{\delta l}\right)\Delta l + 2\left(\Lambda\frac{\delta\eta_{eff}}{\delta T} + \eta_{eff}\frac{\delta\Lambda}{\delta T}\right)\Delta T \qquad (2.6)$$

Fiber Bragg gratings are the ideal sensors for strain and temperature, given that these variables affect directly the fundamental features of the grating device, besides, the output sensitivity is lineal regarding these variables. Different and innovative techniques have been developed for instance to enhance the sensing properties of the FBG sensors and to measure diverse physical variables [12], [13].

FBG temperature sensitivity

Temperature effect on the Bragg wavelength is represented by the second term in equation (2.6). This change is explained as given by equation (2.7), where α_Λ is the thermal expansion coefficient that for standard mono-mode optical fiber is $\alpha_\Lambda = 0.55e^{-6}$, α_η is the thermo-optic coefficient with an approximated value of $\alpha_\eta = 8.6e^{-6}$

$$\Delta\lambda_B = \lambda_B\left(\alpha_\Lambda + \alpha_\eta\right)\Delta T \qquad (2.7)$$

Hence, the sensitivity of a fiber Bragg grating manufactured in standard mono-mode silica optical fiber with central wavelength around 1544 nm is approximately 14.1 $pm/°C$

FBG strain sensitivity

On the other side, the first term of equation (2.6) describes the wavelength shift due to changes in the elongation of the optical fiber, this shift is given by the equation (2.8):

$$\Delta\lambda_B = \lambda_B \left(1 - p_e\right)\varepsilon z \qquad (2.8)$$

with:

$$p_e = \frac{\eta_{eff}^2}{2}\left[p_{12} - \nu\left(p_{11} + p_{12}\right)\right] \qquad (2.9)$$

Where p_e is the effective strain-optic constant, p_{11} and p_{12} are components of the strain-optic tensor, that relate the grating spacing and the change in the refractive index with the applied axial strain. They exhibit typical values of $p_{11} = 0.113$ and $p_{12} = 0.252$; ν is the Poisson's ratio with typical value $\nu = 0.16$ and the effective refractive index is $\eta_{eff} = 1.482$, εz is the axial strain applied to the optical fiber. So, from equation (2.9) the sensitivity of a fiber Bragg grating manufactured at a center wavelength around 1544 nm is about 1.2 $pm/\mu\varepsilon$.

2.1.3 Types of fiber Bragg gratings

Fiber Bragg gratings are defined by different features regarding the type of fiber, its material or even their manufacturing process, this variations yield to different types of FBGs that have a very definite application. In this section, we describe some of the most useful kind of gratings on the subject of sensing systems.

Uniform Bragg gratings

Uniform Bragg gratings are the most common device and are described by constant Bragg period (Λ) and constant index modulation amplitude ($\Delta\eta$) as well as the perpendicularity of the grating regarding the z-axis of the optical fiber. Thus, it is the ideal device to be used as a pass-band filter [14], [15], sensing device [16]–[18] or as a high reflecting mirror [19], [20].

Apodized Bragg gratings

One of the main requirements when designing a FBG device is to select a narrow set of wavelengths around the theoretical Bragg wavelength. Nevertheless, this is not always the case and reflection side-lobes appear often in the design of a simple Bragg grating. An apodized Bragg grating is a special grating intended to minimize the amplitude of the reflected side-lobes.

There are different apodization techniques, which basically consist in concentrate the interference at the center of the FBG and gradually minimize the effect to the sides of the FBG. e.g. a Gaussian or a cosine profile. Using these profiles it can be achieved a reduction of the side-lobes amplitude above 20 dB. Which is especially useful in dense wavelength division de/multiplexing (DWDM). Some manufacturing techniques of apodized gratings are: the symmetric stretching method [21], which varies the intensity of the grating by stretching the fiber around the center of the gratingn, the use of a specially designed phase mask was also demonstrated [22], the mask is designed to have variable diffraction efficiency when illuminated with a uniform UV beam.

Commonly, the apodization of the spectral profile of FBG sensors is a desired characteristic. The main reason for this is that the identification method for FBG-based sensing systems relies on the peak detection of the reflected wavelength, therefore the ideal FBG sensor would reflect power only at the Bragg wavelength and nothing or very little power at other wavelengths (sidelobes). High power sidelobes are not only harmful to the detection of FBG peaks themselves, setting a tight detection threshold to perceive which is the actual Bragg reflection. Also, the presence of a sidelobe with considerable power could affect the readout of neighbor sensors if the sidelobe reaches the operation wavelength range of another sensor in the array under a WDM scheme for example. In such cases the power of the sidelobe can be added to the power of a Bragg reflection band, causing an error in wavelength.

Chirped Bragg gratings

A fiber Bragg grating with chirp is, basically a longer Bragg grating structure in which the spacing period of the grating Λ varies continuously [23], [24]. The effect can be approximated to have a chain of uniform gratings at different Bragg wavelengths so their reflected spectrum will be broader. The applications of this kind of FBG are related to filtering out a big part of the incoming spectrum or compensating the amplitude of a broad portion of the spectrum, also compensating the group delay as a function of wavelength [25].

Tilted Bragg gratings

As mentioned before, the custom way to inscribe a Bragg grating is perpendicular to the z-axis of the optical fiber because the reflected mode will be traveling in the counter-propagation direction so the losses are minimized. Another possibility is exactly the opposite, where the Bragg grating is written into the optical fiber at a certain angle [26]. This can be done with the objective of rejecting the back-propagation or enhancing the coupling of modes traveling in the cladding of the optical fiber.

Superimposed and Super-structured Bragg gratings

Superimposed and super-structured fiber Bragg gratings are terms used often indistinctly, although very similar reflected spectra can be obtained using each one of these techniques, there is a fundamental difference between them.

Superimposed Bragg gratings (Moiré gratings)

Superimposed Bragg gratings are obtained through multiple inscriptions of Bragg gratings at the same spatial location in the optical fiber. The manufacturing process consists simply in writing each Bragg grating consecutively. Manufacturing different gratings in the same region of the optical fiber has two main consequences, first, the reflectivity of the gratings became lower each time a new one is written, due to the strongly non-linear growth of the refraction index caused by the UV flux, and second, the wavelength of the previous gratings is shifted to longer wavelengths due to the change induced in the effective index with the creation of the new grating. See for example [27], [28]

Super-structured Bragg gratings

Super-structured Bragg gratings can achieve reflection spectra very similar to the ones obtained through multiple Bragg grating inscription but they are radically different in their manufacturing process. A super-structured Bragg grating is manufactured by exposition of the optical fiber to a strong UV radiation, to obtain a modulated index pattern $\sim |q(z)|$ along the length of the grating. In general, a super-structured Bragg grating features a complex reflection pattern both in amplitude and phase, which is written by translating the UV writing beam along the Bragg grating length, see [29]. The manufacturing of super-structured FBGs is very useful nowadays because with the rapid growth in optoelectronics there are more specific applications that can not be optimally solved with the simple uniform Bragg grating, however it is desired that a single device addresses different tasks at the same time, [30] is an example of the versatility and complexity that can be achieved with super-structured FBGs, they have manufactured highly complex devices with phase and amplitude patterns to perform filtering and encoding tasks in an actual communications system [31], [32]. It is notable that the manufacturing feasibility does not get compromised, the same phase mask technique used to write the majority of Bragg gratings nowadays can be used to manufacture these complex structures, only adding a controlled translation platform to move the UV incident beam over the optical axis.

2.1.4 Manufacturing of FBGs

The first requirement in the manufacturing process of fiber Bragg gratings is related to the photosensitivity of the optical fiber, i.e. the ability of the optical fiber to change its refractive index when exposed to light radiation. A more thoroughly explanation on the photosensitivity is given in [33]. In the general case, a Silica fiber (SiO_2) doped with germanium (Ge) exhibits more photosensitivity than the common silica fiber. Higher photosensitivity is achieved by soaking the doped fiber in hydrogen [34]–[36] in order to diffuse the hydrogen molecules into the core of the optical fiber. Besides, in the fiber sections non-exposed to UV radiation, the hydrogen diffuses out, which means no absorption losses at the telecommunications windows.

The manufacturing process has evolved considerably since the writing of the first grating [33], [37], This approach carried out the internal writing of the grating by using a high power beam at the wavelength where the optical fiber is photosensitive. In this process, the incident beam becomes diffracted with
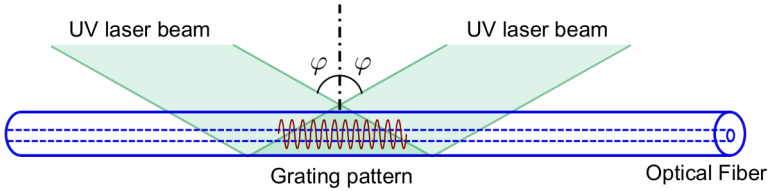
Figure 2.3: Schematic representation of the interferometric technique used to write a grating externally, in general, two beams are split and then intersected at the optical fiber region to create a pattern that depends on the incidental angle and the wavelength.

its Fresnel reflection, and creates an interference pattern (a stationary wave) inside the optical fiber affecting permanently its refractive index.

On the other hand, external writing has been widely researched, different approaches have been proposed, whose principle is to put the optical fiber under the interference of two light beams. When the two beams interfere at a certain angle (see Figure (2.3)), they generate a periodic pattern that is translated to the refractive index in the core of the fiber according to $\Lambda = \lambda_{UV}/2\sin\varphi$ [38]–[40]. The main inconvenient with this technique is its high susceptibility to mechanic vibration.

Other approaches have been carried out to successfully write Bragg gratings into the optical fibers core, for instance, point by point manufacturing is intended to write the grating one step at a time [41], [42], this is of course a highly precision-dependent technique that requires very stable focusing systems and translation platforms. Since the grating period is $sim 0.5\mu$m the error in the platforms should be in the order of nanometers.

Phase Mask technique

A highly efficient technique that is largely used nowadays due to its versatility and easiness of implementation, is the Phase-Mask technique [43]–[45] which consists on the use of a one-side corrugated silica plate with a controlled grating etched in their corrugated surface at a periodic spacing Δ_{PM}. This etching is designed to favor the ± 1 diffraction orders generating a diffraction pattern in the proximity of the phase mask. The phase mask spacing is designed so that $\Lambda = \frac{\Delta_{PM}}{2}$. Figure 2.4 depicts the writing process using the phase mask technique, this technique allows to minimize the inaccuracies due to mechanical
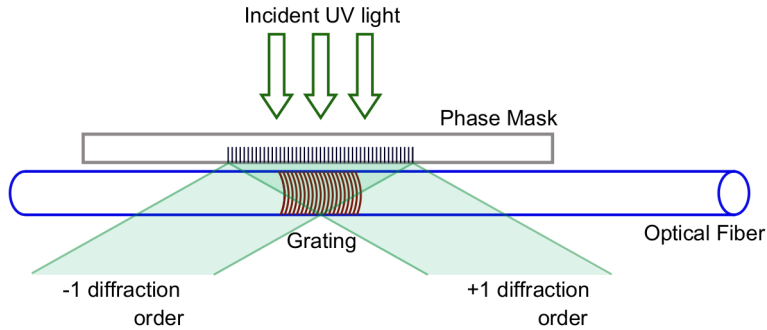
Figure 2.4: Schematic representation of the Phase-mask technique used to write fiber Bragg gratings.

vibration and, since the fiber can be swept in the writing process, it allows to manufacture larger devices easily. On the contrary, its main disadvantage relies in its lack of flexibility given that a different phase mask is required to manufacture gratings at different wavelengths.

Automatic Phase mask technique

The system used to manufacture all the fiber Bragg grating devices presented in this thesis is located at the Photonics Research Labs. (PRL), Universitat Politècnica de València. While this system is mainly based on the phase mask technique, it also has a series of flexible parameters to improve the versatility of the method allowing to manufacture many complex devices with a wide range of reflectivities and index profiles. This system is thoroughly described in [46]. This system is based on the scanning of the fibre/mask relative position (see [47]). So it uses a single uniform phase-mask mounted in a translation platform, as depicted in Figure 2.5, to write almost any realizable complex index profile required in the Bragg grating. A key feature of this manufacturing system is the use of a continuous UV laser beam, driven through a shutter device to obtain a pulsed beam, to create the Bragg pattern in the fiber, this allows to control the growing of the grating by controlling the relative phase alignment between consecutive UV pulsations to the fiber [46] (i.e. any two in-phase pulses will contribute to the growth of the grating while two pulses out of phase create a fading effect in the grating). Another important feature of the manufacturing system is the incorporation of a focusing system allowing the control of the effective width of the beam impacting the optical fiber in
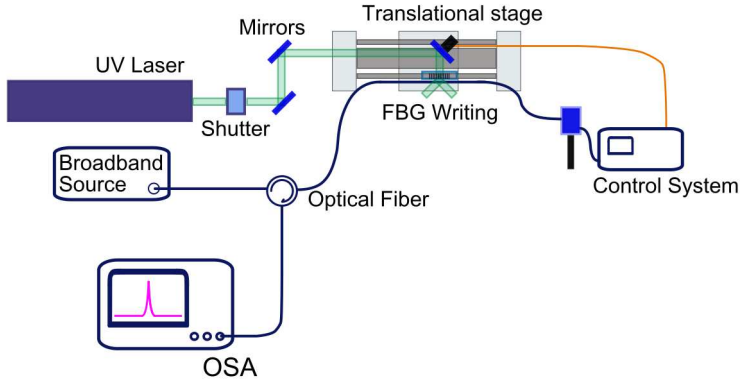
Figure 2.5: Representation of the manufacturing system at the Photonics Research Labs. The laser pulsation is controlled by an optical shutter, the UV beam is directed through a set of mirrors and lenses to the phase mask in order to write the grating device.

both x- and y-axis. This is useful to set the maximum distance permitted between the phase mask and the optical fiber during the writing process and also it allows to gain precision in the manufacturing of complex Bragg grating devices.

2.1.5 Measurement of fiber Bragg grating sensors

A large part of the success of FBG devices is the simplicity of their measurement. When used as sensors, the characterization of optical fiber Bragg gratings is straightforward because it is only necessary to obtain the information related to the wavelength peak of the sensors. Neglecting the power of each sensor in the reflected spectrum saves a lot of work since less importance is given to power fluctuations in the network due to new connections in a given sensing network or losses between stretches of optical fiber. For this purpose, the best measurement instrument is the optical spectrum analyzer (OSA). In communication setups, on the other hand, it is often required to measure the phase and temporal response of the Bragg grating devices (although in most of the cases their spectral response is enough). There are different techniques useful to measure completely the profile of fiber Bragg grating devices. In this section we treat briefly the optical frequency domain reflectometry (OFDR), the modulation phase shift and the optical low coherence reflectometry (OLCR).
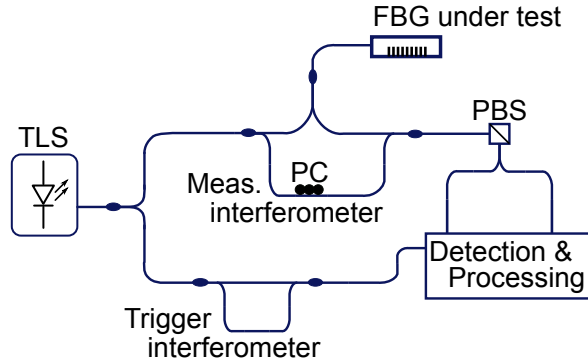
Figure 2.6: Optical Frequency-domain Reflectometry setup to characterize optical devices. TLS: Tunable laser source, PBS: Polarization beam splitter, PC: Polarization controller.

Optical Frequency Domain Reflectometry

OFDR is a well known technique used not only to characterize optical devices but also to be used in large sensing systems given its notable spatial resolution. As a characterization technique, it features a spatial resolution of ∼mm over distances of 1 km approximately [48]–[50], and a relatively fast measurement with high sensitivity and spectral resolution. This is, to a large extent, due to the use of a high power, fast sweep rate tunable laser over a wide wavelength range. OFDR is a very complete technique for it is able to measure the grating reflectivity, phase response and dispersion [51].

The working principle of this technique is based, as already mentioned, on the sweeping of an optical frequency over the total spectrum. In coherent detection, the reflected signal from the device under test (DUT) is mixed with the source reference at the detector. The reflected wave features a frequency component proportional to its transit time that marks the spatial position in the optical fiber [48]. Attenuation can also be seen as a function of the fiber distance.

Figure 2.6 shows a standard schematic of an OFDR characterization setup, the TLS is swept over a wide spectrum and is launched via a 3 dB standard coupler to two Mach-Zender interferometers (MZI); the upper branch is the measurement interferometer which is connected to the device under test (DUT). The signal reflected from the DUT is coupled back to interfere with the reference signal at the measurement MZI, then the produced fringes are detected by a photo-detector and stored in a computer to be processed. The trigger interfer-
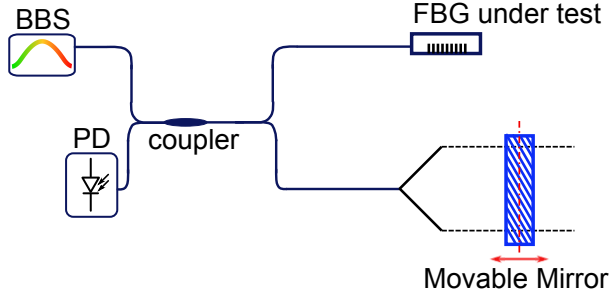
Figure 2.7: Schematic of the Optical Low Coherence Reflectometry technique (OLCR) used to characterize optical devices.

ometer is used frequently to reference the start and end of the sweeping process in the acquisition stage.

Optical low coherence reflectometry

Optical low coherence reflectometry is a technique based in the fast scanning Michelson-Interferometer used to measure the impulse response of an optical device [52]. Figure 2.7 exemplifies the typical schematic of the OLCR technique, the DUT is placed in one arm of the interferometer while a movable mirror is placed in the second arm. Thus, a spatial reflectogram is obtained as the optical path is changed by the position of the mirror in the second arm. The key feature of this approach is that the source has a wide spectral bandwidth, so that the intensity detected at the photo-detector, which is initially given by equation (2.10) where $S(\omega)$ is the spectrum of the low coherence source, $r(\omega)$ is the complex reflectivity of the DUT, can be rewritten as in equation (2.11) due to the fact that for a broadband source, $S(\omega)$ can be considered a constant.

$$i(t) = \frac{1}{2\pi}\Re\left[\int S(\omega)r(\omega)\exp(i\omega t)d\omega\right] \tag{2.10}$$

$$i(t) = C \cdot \frac{1}{2\pi}\Re\left[\int r(\omega)\exp(i\omega t)d\omega\right] \propto h_r(t) \tag{2.11}$$

By using a broadband source, the detected signal from the interferometer is consistent with the DUT impulse response, from where the reflection and impulse response can be retrieved [53], [54].
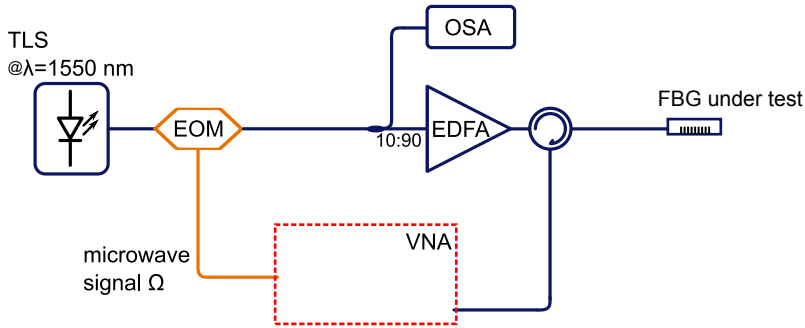
Figure 2.8: Schematic of the Phase shift method used to characterize optical devices.

Modulation phase shift method

Figure 2.8 shows the schematic of the modulation phase shift method to characterize optical devices. The light from a tunable laser source (TLS) is modulated at a microwave frequency ω, to generate a dual wavelength tunable source that is going to be the swept over a wide wavelength range that covers the wavelength of the DUT. The reflected signal from the DUT is detected at a photo-detector and processed in the vectorial network analyzer (VNA) which compares the phase difference between the reflected signal and the microwave signal ω obtaining the phase difference as a function of the swept wavelength $\Delta\varphi(\lambda)$.

References

[1] R. Kashyap, "Fiber bragg gratings (second edition)", in *Fiber Bragg Gratings (Second Edition)*, R. Kashyap, Ed., Second Edition, Boston: Academic Press, 2010, pp. 119–187, ISBN: 978-0-12-372579-0. DOI: https://doi.org/10.1016/B978-0-12-372579-0.00004-1 (cit. on p. 9).

[2] C. R. Giles, "Lightwave applications of fiber bragg gratings", *Journal of Lightwave Technology*, vol. 15, no. 8, pp. 1391–1404, Aug. 1997, ISSN: 0733-8724. DOI: 10.1109/50.618357 (cit. on p. 9).

[3] A. Othonos and K. Kalli, *Fiber Bragg Gratings: Fundamentals and Applications in Telecommunications and Sensing*, ser. Artech House optoelectronics library. Artech House, 1999, ISBN: 9780890063446 (cit. on p. 9).

[4] T. Erdogan, "Fiber grating spectra", *Lightwave Technology, Journal of*, vol. 15, no. 8, pp. 1277–1294, Aug. 1997, ISSN: 0733-8724 (cit. on pp. 10, 11).

[5] H. Kogelnik, "Guided-wave optoelectronics", in *Guided-Wave Optoelectronics*, T. Tamir, Ed. Berlin, Heidelberg: Springer Berlin Heidelberg, 1988, ch. Theory of Optical Waveguides, pp. 7–88, ISBN: 978-3-642-97074-0. DOI: `10.1007/978-3-642-97074-0_2` (cit. on p. 11).

[6] D. Marcuse, "Chapter 3 - {coupled} {mode} {theory}", in *Theory of Dielectric Optical Waveguides (Second Edition)*, D. Marcuse, Ed., Second Edition, Academic Press, 1991, pp. 97–133, ISBN: 978-0-12-470951-5. DOI: `https://doi.org/10.1016/B978-0-12-470951-5.50009-3` (cit. on p. 11).

[7] S. Johannes, "Synthesis and characterization of fiber bragg gratings", PhD thesis, Department of Physical Electronics, Norwegian University of Science and Technology (NTNU), 2000 (cit. on pp. 11, 12).

[8] Z. Zhang, "Passive and active bragg gratings for optical networks", PhD thesis, UNIVERSITY OF SOUTHAMPTON Optoelectronics research centre, 2007 (cit. on p. 12).

[9] D. Pastor, "Redes de difraccion sobre fibra optica para procesado de senales fotonicas.", PhD thesis, Universitat Politecnica de Valencia, 1996 (cit. on p. 12).

[10] K. A. Winick and J. E. Roman, "Design of corrugated waveguide filters by fourier-transform techniques", *IEEE Journal of Quantum Electronics*, vol. 26, no. 11, pp. 1918–1929, Nov. 1990, ISSN: 0018-9197. DOI: `10.1109/3.62111` (cit. on p. 12).

[11] J. Skaar, L. Wang, and T. Erdogan, "On the synthesis of fiber bragg gratings by layer peeling", *IEEE Journal of Quantum Electronics*, vol. 37, no. 2, pp. 165–173, Feb. 2001, ISSN: 0018-9197. DOI: `10.1109/3.903065` (cit. on p. 12).

[12] D. Barrera Vilar, "Diseno, fabricacion y caracterizacion de fbgs e interferometros en fibra optica para la monitorizacion en ambientes adversos", PhD thesis, Universitat Politecnica de Valencia, 2013. DOI: `doi:10.4995/Thesis/10251/33399.` (cit. on p. 13).

[13] A. L. Ricchiuti, "Design and fabrication of customized fiber gratings to improve the interrogation of optical fiber sensors", PhD thesis, Universitat Politecnica de Valencia, 2016 (cit. on p. 13).

[14]   R. Slavik and S. LaRochelle, "Large-band periodic filters for dwdm using multiple-superimposed fiber bragg gratings", *IEEE Photonics Technology Letters*, vol. 14, no. 12, pp. 1704–1706, Dec. 2002, ISSN: 1041-1135. DOI: `10.1109/LPT.2002.804639` (cit. on p. 15).

[15]   K. Kitayama, T. Kuri, K. Onohara, T. Kamisaka, and K. Murashima, "Dispersion effects of fbg filter and optical ssb filtering in dwdm millimeter-wave fiber-radio systems", *Journal of Lightwave Technology*, vol. 20, no. 8, pp. 1397–1407, Aug. 2002, ISSN: 0733-8724 (cit. on p. 15).

[16]   A. Kersey, M. Davis, H. Patrick, M. Leblanc, K. Koo, C. Askins, M. Putnam, and E. Friebele, "Fiber grating sensors", *Lightwave Technology, Journal of*, vol. 15, no. 8, pp. 1442–1463, Aug. 1997, ISSN: 0733-8724. DOI: `10.1109/50.618377` (cit. on p. 15).

[17]   G. A. Ball, W. W. Morey, and P. K. Cheo, "Fiber laser source/analyzer for bragg grating sensor array interrogation", *Journal of Lightwave Technology*, vol. 12, no. 4, pp. 700–703, Apr. 1994, ISSN: 0733-8724. DOI: `10.1109/50.285367` (cit. on p. 15).

[18]   A. T. Alavie, S. E. Karr, A. Othonos, and R. M. Measures, "A multiplexed bragg grating fiber laser sensor system", *IEEE Photonics Technology Letters*, vol. 5, no. 9, pp. 1112–1114, Sep. 1993, ISSN: 1041-1135. DOI: `10.1109/68.257209` (cit. on p. 15).

[19]   G. A. Ball and W. W. Morey, "Continuously tunable single-mode erbium fiber laser", *Opt. Lett.*, vol. 17, no. 6, pp. 420–422, Mar. 1992. DOI: `10.1364/OL.17.000420` (cit. on p. 15).

[20]   G. A. Ball, W. W. Morey, and W. H. Glenn, "Standing-wave monomode erbium fiber laser", *IEEE Photonics Technology Letters*, vol. 3, no. 7, pp. 613–615, Jul. 1991, ISSN: 1041-1135. DOI: `10.1109/68.87930` (cit. on p. 15).

[21]   R. Kashyap, A. Swanton, and D. J. Armes, "Simple technique for apodising chirped and unchirped fibre bragg gratings", *Electronics Letters*, vol. 32, no. 13, pp. 1226–1228, Jun. 1996, ISSN: 0013-5194. DOI: `10.1049/el:19960837` (cit. on p. 15).

[22]   J. Albert, K. O. Hill, D. C. Johnson, F. Bilodeau, and M. J. Rooks, "Moire phase masks for automatic pure apodisation of fibre bragg gratings", *Electronics Letters*, vol. 32, no. 24, pp. 2260–2261, Nov. 1996, ISSN: 0013-5194. DOI: `10.1049/el:19961469` (cit. on p. 15).

[23]   F. Ouellette, "Dispersion cancellation using linearly chirped bragg grating filters in optical waveguides", *Opt. Lett.*, vol. 12, no. 10, pp. 847–849, Oct. 1987. DOI: `10.1364/OL.12.000847` (cit. on p. 16).

[24] G. Brady, K. Kalli, D. Webb, D. Jackson, L. Zhang, and I. Bennion, "Extended-range, low coherence dual wavelength interferometry using a superfluorescent fibre source and chirped fibre bragg gratings", *Optics Communications*, vol. 134, no. 1, pp. 341–348, 1997, ISSN: 0030-4018. DOI: `https://doi.org/10.1016/S0030-4018(96)00558-5` (cit. on p. 16).

[25] R. Kashyap, H. G. Froehlich, A. Swanton, and D. J. Armes, "1.3 m long super-step-chirped fibre bragg grating with a continuous delay of 13.5 ns and bandwidth 10 nm for broadband dispersion compensation", *Electronics Letters*, vol. 32, no. 19, pp. 1807–1809, Sep. 1996, ISSN: 0013-5194. DOI: `10.1049/el:19961207` (cit. on p. 16).

[26] R. Kashyap, R. Wyatt, and P. F. McKee, "Wavelength flattened saturated erbium amplifier using multiple side-tap bragg gratings", *Electronics Letters*, vol. 29, no. 11, pp. 1025–1026, May 1993, ISSN: 0013-5194. DOI: `10.1049/el:19930685` (cit. on p. 16).

[27] A. Othonos, X. Lee, and R. M. Measures, "Superimposed multiple bragg gratings", *Electronics Letters*, vol. 30, no. 23, pp. 1972–1974, Nov. 1994, ISSN: 0013-5194. DOI: `10.1049/el:19941359` (cit. on p. 16).

[28] P. Peterka, P. Koska, and J. Ctyroky, "Reflectivity of superimposed bragg gratings induced by longitudinal mode instabilities in fiber lasers", *IEEE Journal of Selected Topics in Quantum Electronics*, vol. PP, no. 99, pp. 1–1, 2018, ISSN: 1077-260X. DOI: `10.1109/JSTQE.2018.2806084` (cit. on p. 16).

[29] B. J. Eggleton, P. A. Krug, L. Poladian, and F. Ouellette, "Long periodic superstructure bragg gratings in optical fibres", *Electronics Letters*, vol. 30, no. 19, pp. 1620–1622, Sep. 1994, ISSN: 0013-5194. DOI: `10.1049/el:19941088` (cit. on p. 17).

[30] W. Amaya, D. Pastor, R. Baños, and V. Garcia-Munoz, "Wdm-coherent ocdma over one single device based on short chip super structured fiber bragg gratings", *Opt. Express*, vol. 19, no. 24, pp. 24 627–24 637, Nov. 2011. DOI: `10.1364/OE.19.024627` (cit. on p. 17).

[31] W. Amaya Ocampo, "Sistemas opticos con multiplexacion por division en codigo (ocdma) empleando redes de difraccion de bragg sobre fibra optica", PhD thesis, Universitat Politecnica de Valencia., 2008. DOI: `doi:10.4995/Thesis/10251/3788.` (cit. on p. 17).

[32] R. Banos Lopez, "Diseno y caracterizacion de dispositivos codificadores y decodificadores para sistemas ocdma coherentes", PhD thesis, Universitat Politecnica de Valencia, 2015. DOI: `doi:10.4995/Thesis/10251/52022.` (cit. on p. 17).

[33] K. O. Hill, Y. Fujii, D. C. Johnson, and B. S. Kawasaki, "Photosensitivity in optical fiber waveguides: Application to reflection filter fabrication", *Applied Physics Letters*, vol. 32, no. 10, pp. 647–649, 1978. DOI: `10.1063/1.89881`. eprint: `https://doi.org/10.1063/1.89881` (cit. on p. 17).

[34] P. J. Lemaire, R. M. Atkins, V. Mizrahi, and W. A. Reed, "High pressure h2 loading as a technique for achieving ultrahigh uv photosensitivity and thermal sensitivity in geo2 doped optical fibres", *Electronics Letters*, vol. 29, no. 13, pp. 1191–1193, Jun. 1993, ISSN: 0013-5194. DOI: `10.1049/el:19930796` (cit. on p. 17).

[35] R. M. Atkins, P. J. Lemaire, T. Erdogan, and V. Mizrahi, "Mechanisms of enhanced uv photosensitivity via hydrogen loading in germanosilicate glasses", *Electronics Letters*, vol. 29, no. 14, pp. 1234–1235, Jul. 1993, ISSN: 0013-5194. DOI: `10.1049/el:19930825` (cit. on p. 17).

[36] T. A. Strasser, T. Erdogan, A. E. White, V. Mizrahi, and P. J. Lemaire, "Ultraviolet laser fabrication of strong, nearly polarization independent bragg reflectors in germanium doped silica waveguides on silica substrates", *Applied Physics Letters*, vol. 65, no. 26, pp. 3308–3310, 1994. DOI: `10.1063/1.112443`. eprint: `https://doi.org/10.1063/1.112443` (cit. on p. 17).

[37] B. S. Kawasaki, K. O. Hill, D. C. Johnson, and Y. Fujii, "Narrow-band bragg reflectors in optical fibers", *Opt. Lett.*, vol. 3, no. 2, pp. 66–68, Aug. 1978. DOI: `10.1364/OL.3.000066` (cit. on p. 17).

[38] G. Meltz, W. W. Morey, and W. H. Glenn, "Formation of bragg gratings in optical fibers by a transverse holographic method", *Opt. Lett.*, vol. 14, no. 15, pp. 823–825, Aug. 1989. DOI: `10.1364/OL.14.000823` (cit. on p. 18).

[39] I. Bennion, J. A. R. Williams, L. Zhang, K. Sugden, and N. J. Doran, "Uv-written in-fibre bragg gratings", *Optical and Quantum Electronics*, vol. 28, no. 2, pp. 93–135, Feb. 1996, ISSN: 1572-817X. DOI: `10.1007/BF00278281` (cit. on p. 18).

[40] R. Kashyap, J. R. Armitage, R. Wyatt, S. T. Davey, and D. L. Williams, "All-fibre narrowband reflection gratings at 1500 nm", *Electronics Letters*, vol. 26, no. 11, pp. 730–732, May 1990, ISSN: 0013-5194. DOI: `10.1049/el:19900476` (cit. on p. 18).

[41] B. Malo, K. O. Hill, F. Bilodeau, D. C. Johnson, and J. Albert, "Point-by-point fabrication of micro-bragg gratings in photosensitive fibre using single excimer pulse refractive index modification techniques", *Electronics Letters*, vol. 29, no. 18, pp. 1668–1669, Sep. 1993, ISSN: 0013-5194. DOI: `10.1049/el:19931110` (cit. on p. 18).

[42] K. O. Hill, B. Malo, K. A. Vineberg, F. Bilodeau, D. C. Johnson, and I. Skinner, "Efficient mode conversion in telecommunication fibre using externally written gratings", *Electronics Letters*, vol. 26, no. 16, pp. 1270–1272, Aug. 1990, ISSN: 0013-5194. DOI: `10.1049/el:19900818` (cit. on p. 18).

[43] K. O. Hill, B. Malo, F. Bilodeau, D. C. Johnson, and J. Albert, "Bragg gratings fabricated in monomode photosensitive optical fiber by uv exposure through a phase mask", *Applied Physics Letters*, vol. 62, no. 10, pp. 1035–1037, 1993. DOI: `10.1063/1.108786`. eprint: `https://doi.org/10.1063/1.108786` (cit. on p. 18).

[44] D. Z. Anderson, V. Mizrahi, T. Erdogan, and A. E. White, "Production of in-fibre gratings using a diffractive optical element", *Electronics Letters*, vol. 29, no. 6, pp. 566–568, Mar. 1993, ISSN: 0013-5194. DOI: `10.1049/el:19930379` (cit. on p. 18).

[45] P. Dyer, R. Farley, and R. Giedl, "Analysis of grating formation with excimer laser irradiated phase masks", *Optics Communications*, vol. 115, no. 3, pp. 327–334, 1995, ISSN: 0030-4018. DOI: `https://doi.org/10.1016/0030-4018(94)00694-P` (cit. on p. 18).

[46] R. Garcia-Olcina, "Sistema de fabricación de altas prestaciones de redes de difracción en fibra y aplicaciones al campo de los sensores ópticos y a los sistemas de comunicaciones ópticas", PhD thesis, Universitat Politècnica de València, 2008 (cit. on p. 19).

[47] M. J. Cole, W. H. Loh, R. I. Laming, M. N. Zervas, and S. Barcelos, "Moving fibre/phase mask-scanning beam technique for enhanced flexibility in producing fibre gratings with uniform phase mask", *Electronics Letters*, vol. 31, no. 17, pp. 1488–1490, Aug. 1995, ISSN: 0013-5194. DOI: `10.1049/el:19950986` (cit. on p. 19).

[48] W. Eickhoff and R. Ulrich, "Optical frequency domain reflectometry in single mode fiber", *Applied Physics Letters*, vol. 39, no. 9, pp. 693–695, 1981. DOI: `10.1063/1.92872`. eprint: `https://doi.org/10.1063/1.92872` (cit. on p. 21).

[49] U. Glombitza and E. Brinkmeyer, "Coherent frequency-domain reflectometry for characterization of single-mode integrated-optical waveguides", *Journal of Lightwave Technology*, vol. 11, pp. 1377–1384, Aug. 1993. DOI: `10.1109/50.254098` (cit. on p. 21).

[50] P. Oberson, B. Huttner, O. Guinnard, L. Guinnard, G. Ribordy, and N. Gisin, "Optical frequency domain reflectometry with a narrow linewidth fiber laser", *IEEE Photonics Technology Letters*, vol. 12, no. 7, pp. 867–869, 2000 (cit. on p. 21).

[51] S. Kieckbusch, C. Knothe, and E. Brinkmeyer, "Fast and accurate characterization of fiber bragg gratings with high spatial and spectral resolution", in *Optical Fiber Communication Conference*, Optical Society of America, 2003, WL2 (cit. on p. 21).

[52] R. Kashyap, "Chapter 9 - measurement and characterization of gratings", in *Fiber Bragg Gratings (Second Edition)*, R. Kashyap, Ed., Second Edition, Boston: Academic Press, 2010, pp. 405–440, ISBN: 978-0-12-372579-0. DOI: `https://doi.org/10.1016/B978-0-12-372579-0.00009-0` (cit. on p. 22).

[53] S. D. Dyer, K. B. Rochford, and A. H. Rose, "Fast and accurate low-coherence interferometric measurements of fiber bragg grating dispersion and reflectance", *Opt. Express*, vol. 5, no. 11, pp. 262–266, Nov. 1999. DOI: `10.1364/OE.5.000262` (cit. on p. 22).

[54] B. Malo, S. Theriault, D. C. Johnson, F. Bilodeau, J. Albert, and K. O. Hill, "Apodised in-fibre bragg grating reflectors photoimprinted using a phase mask", *Electronics Letters*, vol. 31, no. 3, pp. 223–225, Feb. 1995, ISSN: 0013-5194. DOI: `10.1049/el:19950150` (cit. on p. 22).

Chapter 3

Amplitude encoded Super-structured FBG sensors

3.1 Introduction

Optical Code Division Multiple Access (OCDMA) is a multiplexing technique used in optical access networks [1], [2]. It allows an increase in the user capacity of the system by providing asynchronous access to each user without waiting time (in contrast with other asynchronous techniques [3]). OCDMA assigns a unique orthogonal code to each user of the network so that they can share the wavelength bandwidth at the same time. OCDMA techniques can be broadly classified (according to their sources and detection schemes) into two categories, coherent and incoherent encoding [4]. Incoherent encoding techniques handle uniquely the optical power while coherent encoding makes use also of the optical phase to perform tasks of encoding and decoding. This is the reason why, in general, coherent encoding is better in terms of spectral efficiency, signal to noise ratio and cardinality [5].

Aside from classifying the OCDMA techniques into coherent and incoherent approaches, one can also classify them by the way they treat the information and/or the domain they use. i.e. information encoding is achieved by ma-

nipulating its parameters (amplitude, phase or both) and can be performed indistinctly in the time or wavelength domain.

One of the simplest coding schemes is the so called: pulse-amplitude-coding [3], [6], which is a time domain coding technique that basically decompose the signal into a number of replicas spaced a certain amount in time. In this scheme, incoherent detection is performed to retrieve the summation of the optical intensities (amplitude) of the many signals spread in time. The codes used to spread the signals in time are unipolar pseudo orthogonal codes (e.g. optical orthogonal codes (OOCs) and prime codes).

Another time domain coding scheme is for instance the pulse-phase-coding [7], which introduce 0° or 180° phase shifts to the signals according to a given codeword. These schemes require coherent detection and can use bipolar orthogonal codes (e.g. Walsh codes, maximal length sequences or Gold codes) that exhibit better correlation performance than unipolar codes [8].

Similar approaches to the above mentioned schemes have been developed in wavelength domain coding [9], [10], this is the case of the spectral-amplitude-coding and spectral-phase-coding. In these cases the temporal essence of the information is translated to the wavelength domain after defining a common wavelength reference. To this purpose, Bipolar orthogonal codes are also preferred.

2D coding schemes should also be mentioned; for instance, the wavelength-hopping - time-spreading coding technique [11] performs information encoding in the time and wavelength domains, taking advantage of each method to achieve more robust and secure transmissions.

In any OCDMA transmission system, the transmitted signals from many users merge in the transmission link, all the information is broadcast to each receiver node in the network. At each receiver node, the information is decoded by performing the correlation product between the decoder and all the gathered information. The correlation product has two possible outcomes: the auto-correlation signal, featuring a peak that indicates correspondence between the decoder codeword and the original message; and the cross-correlation signal which does not exhibit any peak at all, meaning that the information has not been decoded properly. When the decoder output in a transmission system is an auto-correlation signal, the original message is reconstructed from the merged information. On the contrary, if no peak is achieved (cross-correlation) the specific node is not able to receive the message.

To replicate the OCDMA concepts in a sensing system one should part from the simplest and most effective encoding schemes, therefore, one-dimensional unipolar codes (i.e. OOCs and prime codes) should be considered. These sets of codewords feature good correlation properties (i.e. a high auto-correlation peak and a constrained cross-correlation function). Besides, they are suitable to implement a system based in optical power measurement, which is the easiest and most common approach to implement an optical sensing system.

In this work, we focused on the optical orthogonal codes (OOCs) to design the encoded sensors given that, as opposite from communication systems, fewer codewords are necessary in a sensing system, besides, they should be simple (positive) codewords with a limited length. A set of orthogonal codewords in OCDMA must satisfy the following two conditions: each codeword must be distinguishable from shifted versions of itself and they should be distinguishable from any other codeword in the set. OOCs can be defined as follows: an OOC family represented as $(n, \omega_c, \lambda_a, \lambda_c)$ is a set of binary (0,1) codewords, where n represents the codewords length, ω_c is the weight of the codeword (number of bits set to '1') and λ_a, λ_c are the auto- and cross-correlation constraints. Therefore a $(n, \omega_c, \lambda_a, \lambda_c)$ family S is an OOC (satisfies mutual orthogonality) when it meets the following auto- and cross-correlation properties [12]:

DEFINITION 3.1.1 *Auto-correlation property: for any codeword* $x = [x_0, x_1, \ldots, x_{n-1}] \in S$ *and any integer* $\tau \in (0, n) \Rightarrow \sum_{t=0}^{n-1} x_t x_{t \oplus \tau} \leq \lambda_a$. *Being* $\oplus$ *the modulo-n addition.*

DEFINITION 3.1.2 *Cross-correlation property: for any codeword* $x = [x_0, x_1, \ldots, x_{n-1}] \in S$ *and any* $y = [y_0, y_1, \ldots, y_{n-1}] \in S$ *such that* $x \neq y$ *and any integer* $\tau \in (0, n) \Rightarrow \sum_{t=0}^{n-1} x_t y_{t \oplus \tau} \leq \lambda_c$.

Different techniques such as greedy algorithms, block designs [13]–[15], among others [16], [17], have been employed to construct OOCs' families [18], always seeking for code families with λ_a, λ_c as small as possible and with the largest possible cardinality $|C|$ i.e. the number of codewords in the family.

Taking into account the above mentioned considerations, we selected sets of 2 and 3 OOCs through the combinatorial method described in [18]. The selected set, with 2 orthogonal codewords is exemplified in Figure 3.1, the two codewords: $S1 = 11001000$ and $S2 = 10100001$ of an $(n, \omega_c, \lambda_a, \lambda_c) = (n, \omega_c, \lambda) = (7, 3, 1)$ OOC family have a weight of 3, with auto- and cross-correlation constants constrained to a value of 1.
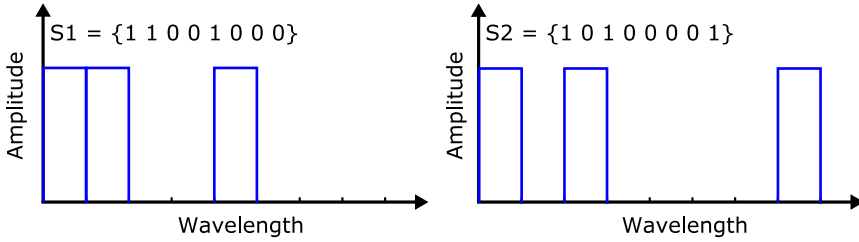
Figure 3.1: Waveform of the two orthogonal codewords $S1 = 11001000$ and $S2 = 10100001$ corresponding to a $(7, 3, 1)$ OOC family.

We have proposed the use of orthogonal codewords to encode the FBG sensors, adding useful information to each sensor in the network. Other approaches have been carried out by relating CDMA coding and FBG sensors, nevertheless, these techniques focused primarily on the encoding of the light source [19]–[22]. In this work, the coding methodology is applied to shape the encoded sensors, which have a reflection profile distributed over different wavelengths. In this sense, the encoded sensors can be manufactured as super-structured FBG (SSFBG) devices in order to maintain important properties such as: small size, tunability and manufacturing simplicity. The main contribution of this sensors is to allow wavelength detection under overlapping conditions; thus enhancing the number of sensors that can be multiplexed in a sensing network. It is important to mention that the identification problem of two sensors under overlapping conditions have been previously addressed. The main idea of these approaches is to discriminate the weight of each sensor over the compounded measured spectrum [23]–[26]. This is performed through the use of non-deterministic optimization techniques (bio-inspired algorithms) that find the best possible contribution of each sensor to a given total reflection spectrum.

In this chapter, a detailed description of the SSFBG sensing devices design is addressed in Section 3.2, in this section is also derived the detection process that yields to the central wavelength detection of each sensor in the spectrum.

In Section 3.3, the SSFBG encoded sensors are simulated. First of all, the influence of certain design parameters (e.g. reflectivity, sub-bands width, sub-bands detuning) is studied as a function of the detection error. Some design conclusions are drawn from the simulation of the sensing devices. Second, wavelength detection under overlapping scenarios is proved and the detection error of the sensing system is theoretically assessed. Finally, the synthesis and manufacturing parameters of the SSFBG are developed and explained.

In Section 3.4, the results from the characterization of the manufactured de-
vices are discussed, and the experimental demonstration of the amplitude-
encoded SSFBG sensors is carried out, achieving total detection of two or
more sensors under (partial or total) overlapping conditions. Also, it is ver-
ified the experimental error obtained as a result of the spectral overlapping
between adjacent sensors. Finally, Section 3.5 presents the overall conclusions
of the chapter.

3.2   Amplitude encoded sensors: Design

As mentioned before, the proposed amplitude encoded FBG sensors are de-
signed after the elementary set of codewords known as Optical Orthogonal
Codewords (OOC). These families of codewords can be obtained through the
combinatorial method proposed by Salehi in [18]. In order to preserve the
spectral efficiency of the devices and having into account that the number of
orthogonal codewords in sensing applications should not be high (as opposite
to communications systems were a great number of users are required), we
used, in this work, sets of two and three orthogonal codewords.

The first selected set, with cardinality $C = 2$, is composed of the codewords:
$S1 = [11001000]$ and $S2 = [10100001]$. Each one of these codewords is com-
posed of 8 bits with a weight of 3 (the number of bits set to $'1'$). The correlation
product between these two codewords is depicted in Fig. 3.2, this product is
performed between the original codeword and all the codewords in the set and
the shifted versions of each one. It is obtained a peak at the point of coincidence
with the same codeword when no shift applied, this is the auto-correlation peak
(ACP), the result obtained from the remaining codes and shifted versions is
the cross-correlation signal. Which is constrained to a fixed value, one third of
the ACP in this case, given by the codewords weight. The correlation product
proved that this set of codes satisfy the two rules of orthogonality and there-
fore they can be used to design a set of two encoded sensors able to be totally
distinguishable between them by obtaining their ACP, this is possible because
the cross-correlation value can never reach the ACP value.

In order to design a sensing device based on the orthogonal codes presented
above we used the concept of super-structured fiber Bragg gratings (SSFBG),
which are multi-band FBG devices manufactured at once in the same spatial
region of the optical fiber. SSFBG devices have been used to prove OCDMA
communications systems [27]–[29] due to their wavelength tunability and man-
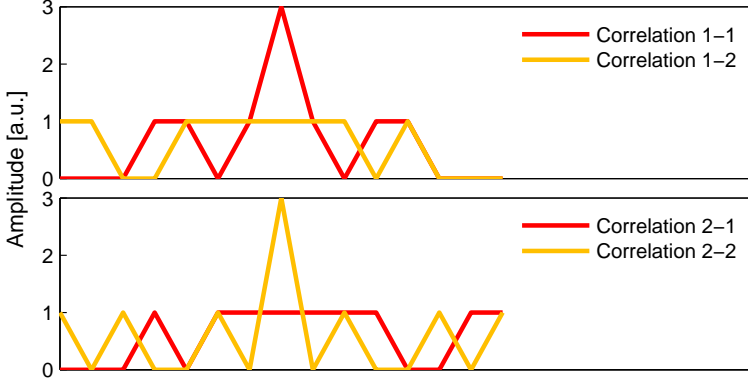ufacturing advantages. The orthogonal codewords can be translated to the

Figure 3.2: Auto- and Cross-correlation function for a set of two orthogonal codewords $S1 = [11001000]$ and $S2 = [10100001]$.
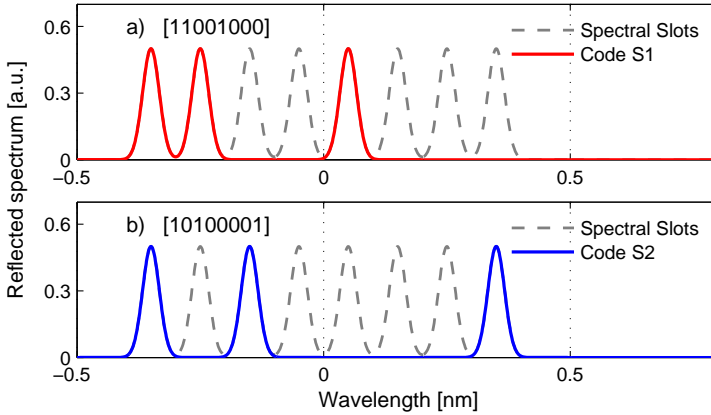

Figure 3.3: Representation of a set of two encoded FBG sensors. Sensors $S1$ and $S2$ are designed according to the codewords $S1 = [11001000]$ (a) and $S2 = [10100001]$ (b).

shape of a SSFBG device as depicted in Fig. 3.3: an orthogonal binary code is converted into a multi-band device by defining 8 equally spaced spectral slots and assigning a reflection sub-band to each bit set to one in the codeword, e.g. the codeword $S1 = [11001000]$ would be translated to a spectral shape featuring reflection sub-bands at the bit positions (1,2,5). See Fig. 3.3, the same holds for the sensor based on the codeword $S2 = [10100001]$. Of course this 'binary to reflection' conversion is not the unique practical consideration when designing a set of mutually orthogonal sensing devices. There are a series of parameters used to define the SSFBG devices that need to be accounted because they will have a big influence on the performance of the sensing system. Perhaps the most trivial design parameter affecting the SSFBG devices would be the reflectivity of the device, in general, it will be desired that the whole device presents a constant reflectivity over its total spectrum. Other key parameter is precisely the spacing between the sub-bands because it will determine to a large extent the device total bandwidth. Also, the width of each sub-band itself is a parameter that will influence mainly the physical length of the devices. Considering these main parameters we modeled the total reflected spectrum of the SSFBG devices ($R(\lambda)$) as follows (3.1):

$$R(\lambda) = \sum_{j=1}^{K} \sum_{i=-N/2+1}^{N/2} c_j(i) \cdot R' \cdot g(\lambda - \lambda_{Bj} - \Delta\lambda_{Bj} - (\delta\lambda \cdot i - \delta\lambda/2)) \quad (3.1)$$

Where, for a number of sensors K, with N sub-bands. The bit-code $c_j(i)$ activates each reflection sub-band composing the sensing device, $g(\lambda)$ is the spectral shape of the sub-bands, with reflectivity R' and Bragg wavelength λ_{Bj}, $\delta\lambda$ is the spectral separation between sub-bands. Increment on the N sub-bands goes from $-N/2 + 1$ to $N/2$ allowing the length of the codewords to be even or odd. Using equation (3.1) to model the SSFBG devices, the sensors spectra is obtained as depicted in Figure 3.3 basically obtaining a conversion from the discrete binary values to an amplitude encoded sensing device (Gaussian shape has been selected to perform the conversion from the binary codeword to the actual FBG device).

The number of orthogonal codewords in a family is directly proportional to the length of the codewords, i.e. a higher number of mutually orthogonal sensing devices can be obtained at the expense of a longer codeword, equivalent to a higher bandwidth in the SSFBG devices. A family of three orthogonal codewords features a minimum length of 12 bits and is composed by the codewords: $S1 = [110000100000]$, $S2 = [101000000100]$ and $S3 = [100100000001]$, their mutual correlation products are depicted in Fig. 3.4 and their conversion in sensing SSFBG devices is represented in Fig. 3.5. It is observed that
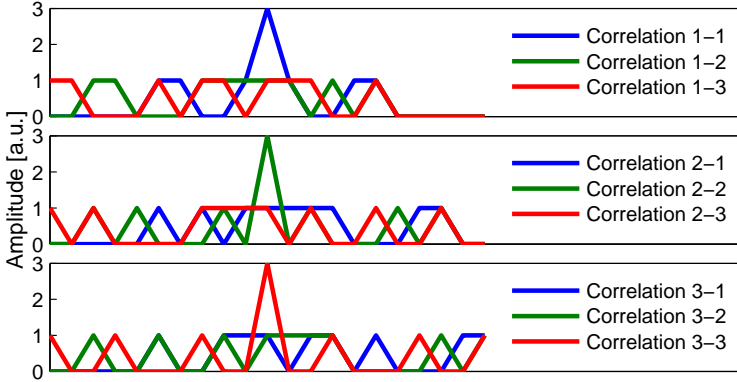
Figure 3.4: Auto- and Cross-correlation function for a set of three orthogonal codewords $S1 = [110000100000]$, $S2 = [101000000100]$ and $S3 = [100100000001]$

an increment in the cardinality of the codewords family means a considerable increasing of the device bandwidth.

3.2.1 Detection process

The algorithm used to demodulate the central wavelength of the encoded FBG sensors is based fundamentally on the correlation product. As mentioned before, the correlation product is the tool used to assess whether a set of codewords satisfy mutual orthogonality or not. In the detection process, the auto-correlation algorithm have been used to interrogate conventional FBG sensors [30], [31]. In our proposal, the correlation algorithm is used to retrieve each sensor wavelength and it is of special interest because it allows to identify the central wavelength of any sensor in spite of partial or full overlapping conditions. Thus, the correlation product can be used to determine the central spectral position of any given sensor in the network. Since each sensor is designed after an orthogonal code, the correlation between the measurement and its original spectral code will generate an auto-correlation peak (ACP). On the contrary, at all the remaining positions, the correlation product will be constrained to a low value because of the mismatching between the sensor and the designed spectrum. From this concept, the wavelength detection process can be performed after recording the total reflection spectrum from the sensing network with an OSA. Then, the correlation product between the theoretical spectral shape of each encoded sensor and the instant recorded spectrum can be performed. The ACP obtained will indicate the central wave-
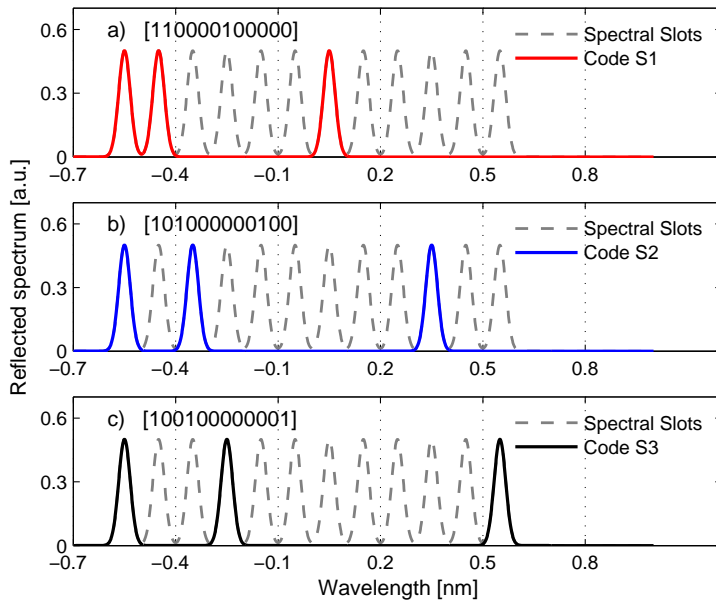
Figure 3.5: Representation of a set of three encoded FBG sensors. Sensors $S1$, $S2$ and $S3$ are designed according to the codewords $S1 = [110000100000]$ (a), $S2 = [101000000100]$ (b) and $S3 = [100100000001]$ (c)
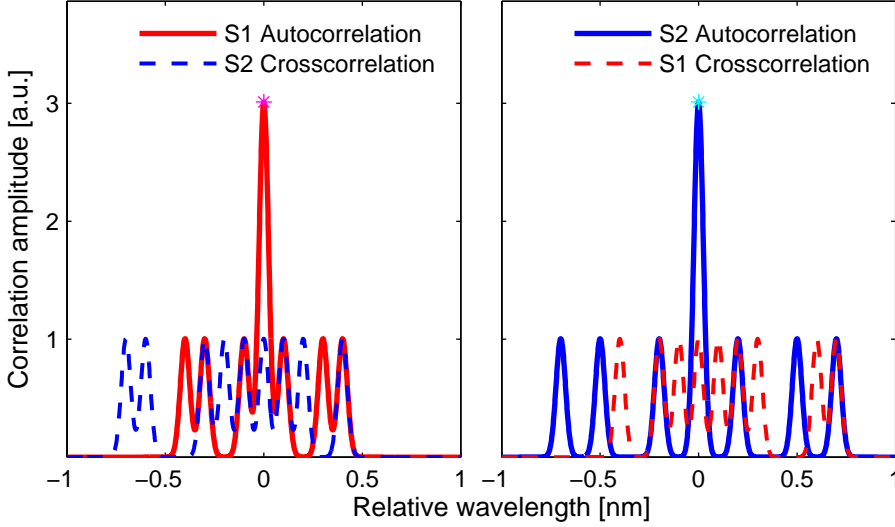
Figure 3.6: Auto- and cross-correlation signals obtained by applying the identification function. The peak of the auto-correlation signal points at the central wavelength of the corresponding sensor.

length position $\lambda_{B_j} + \Delta\lambda_{B_j}$ of the matching sensor in the spectrum, while all the non-coincident spectral positions will produce a XC value constrained according to the theory. The *Identification Function* $IF(\lambda')$ in equation (3.2) describes the comprehensive process in which each theoretical encoded sensor shape is swept over the whole recorded spectrum. Computationally, the whole detection procedure does not add any complexity to the system because it is a simple moving scalar product.

$$IF_j(\lambda') = \int \left(\sum_{i=-N/2+1}^{N/2} c_j(i) \cdot g(\lambda - \lambda' - \delta\lambda \cdot (i - 1/2)) \right) \cdot R(\lambda)d\lambda \quad (3.2)$$

The auto-correlation: $S1 : S1$, $S2 : S2$, and the cross-correlation: $S1 : S2$, $S2 : S1$ products are depicted in Figure 3.6 for the designed sensors. They are obtained by applying the procedure described in equation (3.2), the ACP is obtained at the matching wavelength position along with some low value sidelobes corresponding to the shifted version of the same sensor. On the other hand, the XC signal is constrained to low values at all the wavelength positions.
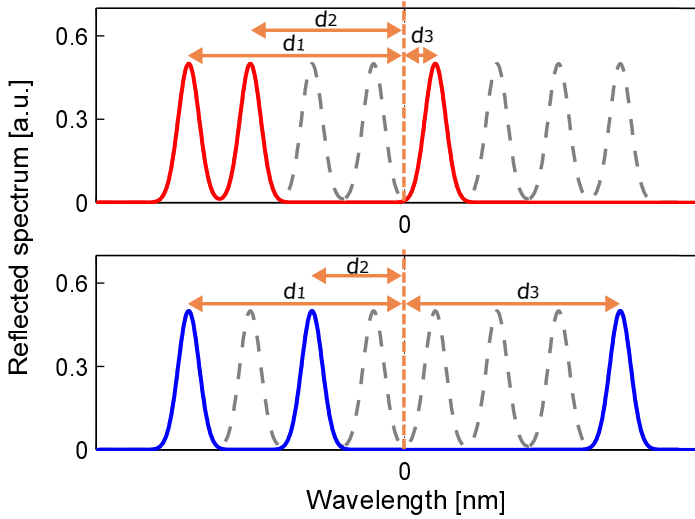
Figure 3.7: Representation of a set of two amplitude-encoded SSFBG sensors, where the relative distance of each sub-band to the center can be used to confirm the spectral location of any given sensor in the network.

The sensors encoding represents not only the possibility of measure correctly their central wavelength under overlapping conditions, it also provides the sensors with more information that can be exploited. For instance, it is possible to perform an additional step in the detection algorithm that is useful to eliminate the error caused by the summation or interference between the cross- and the auto-correlation signals. The additional part of the algorithm is exemplified in Figure 3.8 where the simple and the *two-steps* algorithms are depicted. The additional task in the *two-steps* process consists in calibrating the distance of the obtained ACP to each sub-band of the sensor, given that each sensor can be defined also as a function of the relative distances between sub-bands as exemplified in Figure 3.7, i.e. the sensor $S1 = [11001000]$ can be represented as a function of the high positions in the codeword: $S1(0,1,4)$, or as a function of the sub-bands distances to the center: $S1(d_1, d_2, d_3)$. In this way, and given that *only one of the sub-bands get overlapped at the same time*, the overlapped sub-band can be detected because of the mismatch regarding the theoretical distance to the center of the sensor. The overlapped sub-band is then discarded and the new ACP, without overlapping error can be detected. It is noticeable, from Figure 3.8 that the *two-steps* process does not add further complexity to the initial detection process.

Correlation Algorithm

2-steps Correlation Algorithm
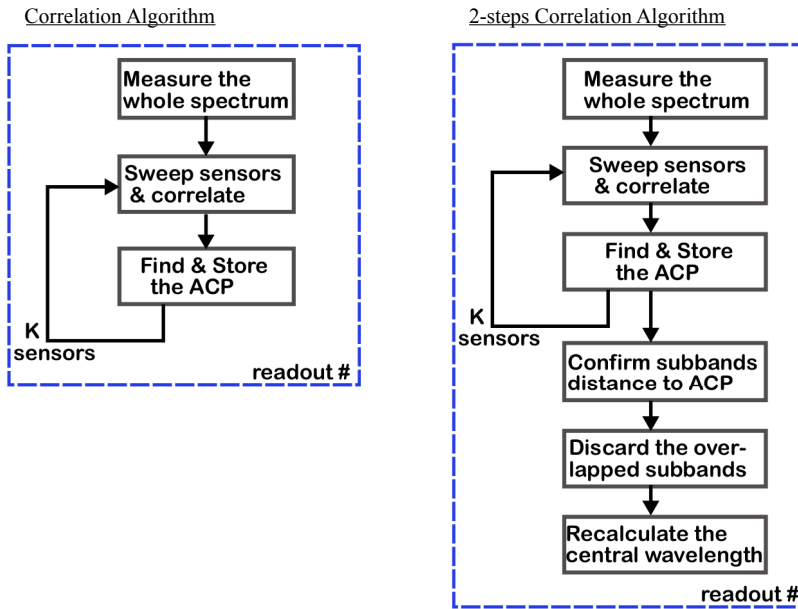
Figure 3.8: Schematic representation of the two detection algorithms. The simple, corre-
lation process is described in the left side, and the *two-steps* process in the right side

Table 3.1: Simulation Parameters

Parameters	Symbols	Range	Final value
Spatial Resolution	Res	[1 - 5]	1 pm
Reflectivity	R	[0.1 - 1]	0.5
Sub-bands' width	FWHM	[0.04 - 0.1]	0.04 nm
Slot spacing	$\delta\lambda$	[0.08 - 0.16]	0.1 nm
Number of Sensors	NoS	[1 - 3]	3
Connection type	Config.	Parallel / Serial	**Serial**

3.3 Modeling the encoded FBG sensors

The purpose of this work is to propose, manufacture and validate a new kind of optical sensors, using encoding techniques in order to improve the performance of the sensing networks in terms of capacity and intelligence. In this chapter we focused on the development of a multi-band fiber Bragg grating device featuring amplitude encoding based on a simple set of codes, namely the optical orthogonal codes (OOC). This set of binary sequences with a definite length and weight satisfy the orthogonality conditions, but this is not the only design parameter to be accounted especially when considering the manufacturing feasibility of the devices. In order to evaluate the effect of the design parameters and the performance of the encoded FBG sensors under overlapping conditions a simulated scenario was developed. It allowed to evaluate, before running into fabrication of the devices, the relevance of the practical parameters such as: sub-bands width, reflectivity, spectral distance between sub-bands, among others. The modeling of the sensors before manufacturing is essential not only to evaluate each parameter significance to the whole sensor design, but also to validate the viability of the detection process of each sensor under different multiplexing scenarios that may or may not include overlapping.

3.3.1 Parameters influence

Sensors modeling will be mainly focused on evaluating the effect of the parameters listed on table 3.1 over the detection algorithm that allows to track the central spectral position of each sensor even if two or more sensors are overlapping due to physical changes in the measured variables. The main objective in a sensing system is to identify clearly the signal from each sensor, which

means, in our detection case, that a high dynamic range should be preserved between the auto- and the cross-correlation signals obtained from the whole sensing network. This condition, besides being good to identify each sensor in the spectrum, is unavoidable in the case of overlapping sensors where multiple sensors share the same spectral position, and their wavelength identification must be guaranteed.

SSFBGs Reflectivity

The reflectivity of the SSFBG devices is a key parameter not only because it can affect directly the correct identification of each sensor in the spectrum, but also because it is a key manufacturing parameter for the devices.

To develop the simulations, the set of two amplitude encoded SSFBG sensors is evaluated in terms of their detection capability and performance while changing their reflectivity. The set of sensors will be modeled according to the codewords $S1 = [11001000]$ and $S2 = [10100001]$, they are 8-chip (sub-bands) devices with a full width at half maximum (FWHM) of 0.04 nm at each sub-band and separation between sub-bands of 0.12 nm.

The first consideration we can make is the effect of the SSFBG devices reflectivity over the system measurement error. This error is the absolute difference between the theoretical sensor position and the measured one, obtained after overlapping. Another possible investigation is to consider the effect of changing one of the devices reflectivity while the overlapped sensor remains with a fixed reflectivity value. To evaluate the former postulation, the reflectivity of the sensors is modified from 10% to 100%, it is worth to note that in this case the configuration of the sensing network is of crucial importance: in a serial network the first sensor receives the full power from the illuminating source, and reflects a portion of it, while the subsequent sensors will get the remaining light at the matching wavelengths, this is known as the shadowing effect and it is of great importance in our overlapping scenarios. In the parallel configuration case, on the contrary, the illuminating light is divided equally between the sensors and so, they do not get 'blinded' by a previous sensor. Figure 3.9 shows the maximum detection error obtained for each sensor in a serial configuration as a function of their reflectivity (the two detection algorithms are plotted). With the simple detection method, an error of ~ 5 pm is obtained almost as a constant for the two sensors at all the reflectivity values, although the second sensor exhibits more error. This detection error is eliminated at low reflectivity values by employing the 2-steps improved detection algorithm, nevertheless
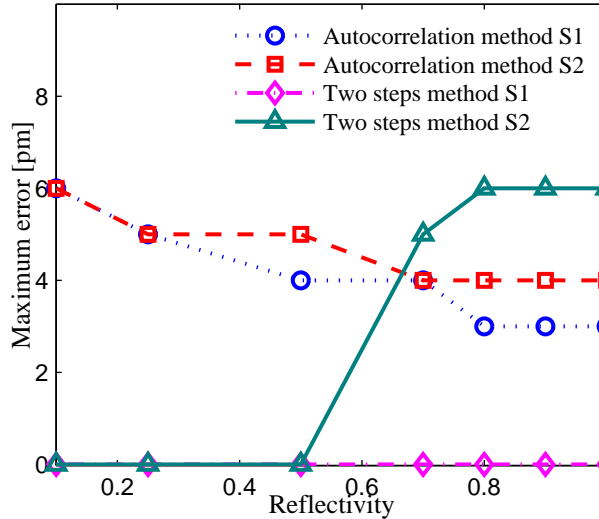
Figure 3.9: Maximum detection error of each sensor in a serial array of two SSFBG sensors as a function of their reflectivity. The two detection algorithms are shown: the simple, correlation-based, detection algorithm and its improved version.

this method is not able to eliminate the detection error for the second sensor at reflectivities above 70%.

As mentioned above, this effect does not occur when deploying the overlapping sensors in parallel configuration, therefore, both serial and parallel configuration are suitable to be implemented, just minding that the shadowing effect is intrinsic to the serial configuration (low reflectivity sensors should be used). In parallel configuration, although the reflectivity of the sensors is not constrained to low values, passive splitter devices should be used inducing losses to the sensing system.

Now, to evaluate the detection performance in a sensing system composed of two overlapping sensors a simulation was performed: In the simulated scenario, the first sensor remains at the initial position with a fixed reflectivity value, while the second sensor is swept over the sensor S1. Sensor S2 reflectivity is increased progressively (several overlapping scenarios are simulated) to evaluate its effect over the wavelength detection of each sensor. Figure 3.10 shows the effect of varying one of the sensors reflectivity over the detection error of each sensor. While the reflectivity of the sensor $S2$ augments, its detection error diminishes because it is proportional to the magnitude of the sensor $S1$
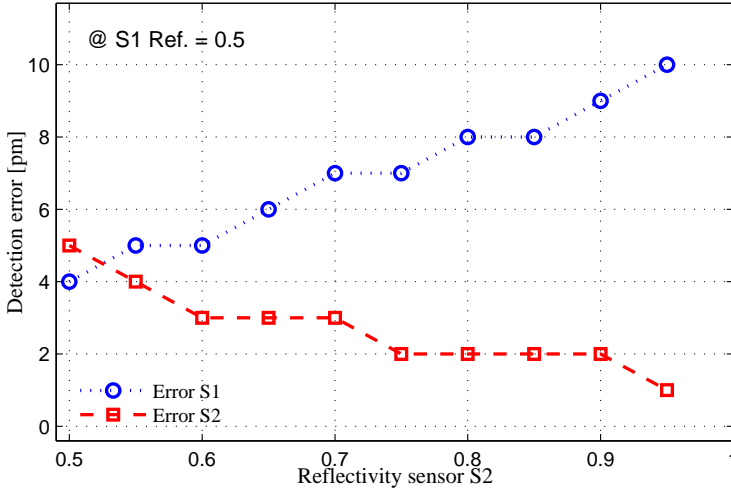
Figure 3.10: Maximum detection error of each sensor in a serial array of two SSFBG sensors while the reflectivity of the sensor $S2$ is varied from 50% to a 100%. The detection error of sensor $S2$ decreases because the magnitude of the correlation product becomes bigger; on the other hand, the detection error of sensor $S1$ increases as it gets affected by a bigger cross-correlation product of the second sensor.

cross-correlation. On the other hand, the sensor with less reflectivity becomes affected and its detection error increases according to the reflectivities difference.

In Figure 3.11 it is depicted the influence of varying one of the sensors reflectivity over the ratio XC/ACP in the detection of the sensors. As the detection process consists on the direct product between the designed shape of the sensors and the total reflected spectrum, it is expected that with larger reflectivity values the whole correlation product will increase. Nevertheless, the ratio between the cross- and the auto-correlation products is affected by the reflectivity values of the overlapping neighboring sensors. In this way, the influence of a sensor ($S1$) with less reflectivity that the sensor $S2$ will be smaller than the influence of two sensors with equal reflectivity values.
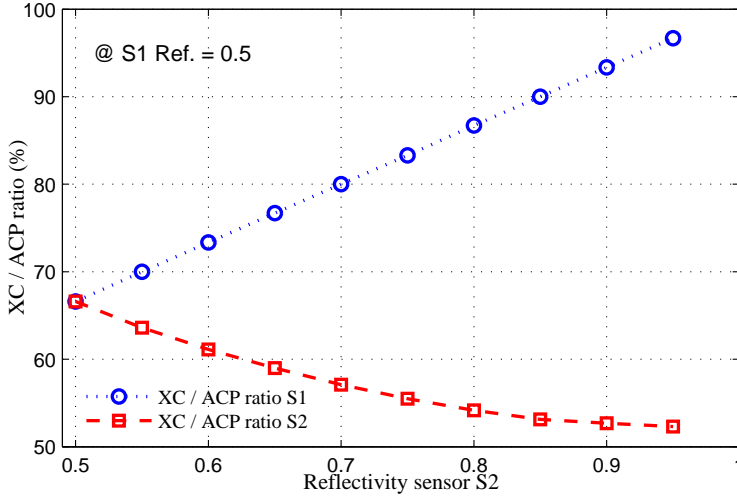
Figure 3.11: Ratio between the cross-correlation and the auto-correlation (XC/ACP) obtained in the detection of two sensors in a serial configuration while the reflectivity of the sensor $S2$ is varied from 50% to a 100%. A sensor with bigger reflectivity leads to a better XC/ACP ratio and consequently to less error in the detection. On the contrary, the XC/ACP ratio of the sensor with less reflectivity is affected and therefore its detection error worsens.

Sub-bands spectral width

The spectral width of each sub-band composing the SSFBG encoded sensor is an important parameter not only because it is directly linked to the device spectral extent, but also because it can affect the detection error. The reason for this is that the detected central wavelength is obtained from the decoded spectrum which is the summation of the auto- and the cross-correlation signals; wider sub-bands imply a widening of the cross-correlation signal and therefore they have more influence in the detected signal, besides, widening of the decoded spectrum makes more difficult to establish the central peak of the auto-correlation peak.

On the other hand, a narrow design of the sub-bands results in a longer device given the inverse relationship between the length of the FBG devices and their FWHM [32].

To quantify the influence of sub-bands spectral width ($FWHM$) over the detection error, we took as a reference the slots distance defined for the SSFBG $\delta\lambda$. Figure 3.12 shows the maximum detection error obtained for each sensor as
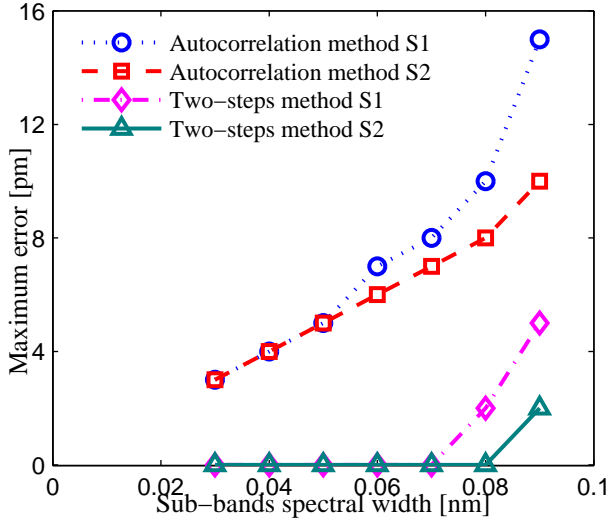
Figure 3.12: Effect of the sub-bands width over the detection error obtained through simulation. The slot spacing is maintained constant at $\delta\lambda = 0.12$ nm. The two detection methods are analyzed.

a function of the sub-bands spectral width ($FWHM$) for a fixed spacing of the slots $\delta\lambda = 0.12$ nm. At the end we obtain a design limitation in terms of the relation $\delta\lambda/FWHM$ given that the two parameters are proportional (a bigger slot spacing would allow a bigger width of the sub-bands). As a result from the Figure 3.12 a 2:1 ($\delta\lambda/FWHM$) relation should be preserved, always intending to design a spectrally compact SSFBG device, under the manufacturing feasibility restrictions.

Wavelength offset between sub-bands

The analysis about the effect of each design parameter in the performance of the sensing network have been done under the assumption that the central wavelength of each sub-band is tuned according to the design. Nevertheless, due to the manufacturing feasibility this will not be always the case. Through simulation, we can assess the effect caused by the wavelength detuning of one of the sub-bands over the detection process. Figure 3.13 shows the relationship between the detection error and an artificial wavelength-offset applied to one of the device sub-bands.
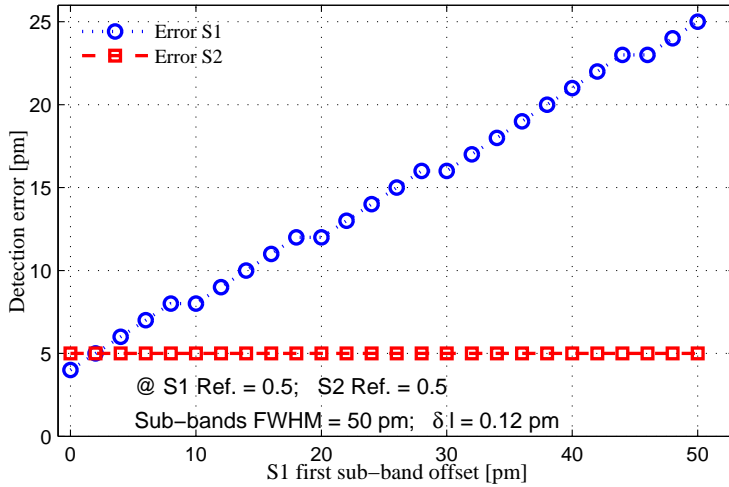
Figure 3.13: Effect of detuning one of the sensor sub-bands over the detection error after the auto-correlation process.
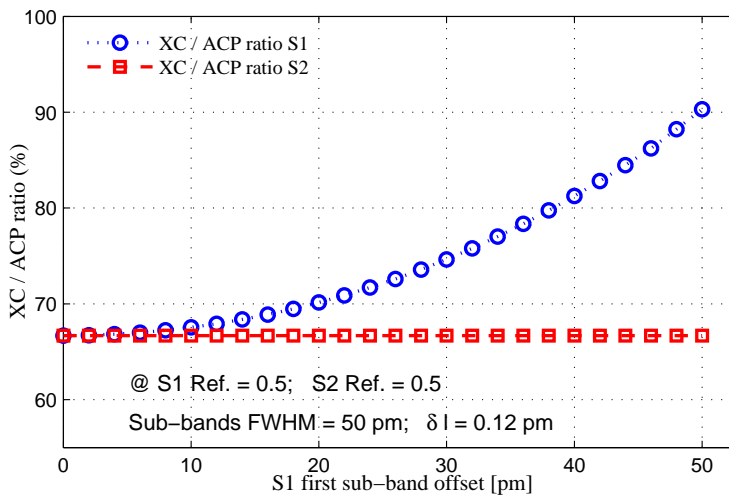
Figure 3.14: Effect of detuning one of the sensor sub-bands over the ratio between the cross- and the auto-correlation of the overlapping sensors.

In Figure 3.14, it is shown the effect of detuning one of the sensors sub-bands over the cross- and the auto-correlation signals obtained in the detection of the sensors. As expected, a misadjustment in one of the sensors sub-bands will worsen the detection error of the corresponding sensor, still, it is important to analyze its effect over the other sensors: in both, Figures 3.13 and 3.14 it is shown that for the unaffected sensor neither the detection error nor the XC/ACP ratio are affected by the detuning of other sensor in the spectrum.

In general, the error induced by this central wavelength offset could be eliminated in the detection process by using the exact shape of the manufactured devices to perform the detection of the sensors, this, although a little bit intricate (it requires the previous calibration of the sensors arranged in the sensing system), would eliminate the mismatch between the designed and the manufactured sensing devices.

Codewords length - number of sub-bands

Although the ratio ACP/XC gets better for codewords with a greater chip number (sub-bands of the sensor in our case), in our sensing application we are interested in spectrally compact sensors, i.e. SSFBG devices that maintain orthogonality but are designed after short codewords. In this way our system of two SSFBG sensors, each one designed after codewords with length $= 8$ bits, with slot spacing $\delta\lambda = 0.1$ nm and sub-bands width $W = 40$ pm, will have a total spectral length of 0.74 nm.

For the next family of orthogonal codewords, with three orthogonal sensing devices the spectral length of each device would need 12 bits, increasing the total spectral width of each sensor to 1.14 nm. Which is also achievable but contributes to a limitation in the number of sensors since the operational spectrum range for three sensors, each one with a 1.14 nm width, would be considerably larger and therefore, less sensors could be located in the total spectrum.

3.3.2 Overlapping scenarios

After designing the SSFBG encoded sensing devices and selecting the proper manufacturing parameters, some detection scenarios can be tested in order to verify the correct wavelength identification of the sensors with and without overlapping conditions, to do so, the detection algorithm including an additional routine to eliminate the cross-correlation error is used. Also, both connection schemes (parallel or serial) are simulated and assessed in terms
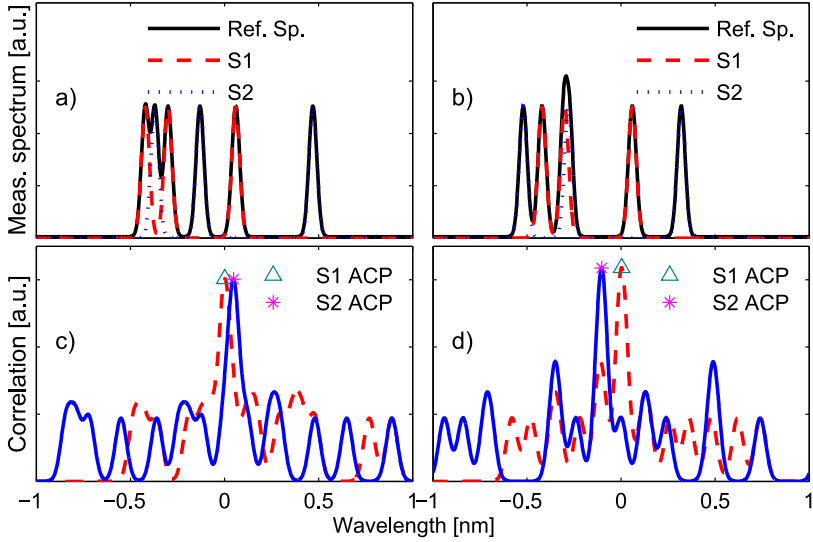
Figure 3.15: Simulated reflected spectrum for two orthogonal sensors encoded in amplitude a), b). In c), d) their correlation products are obtained, pointing at the central wavelength of each sensor.

of the total error obtained. For instance, Figure 3.15 a), b) depicts the instantaneous reflection spectrum measured for an array of two encoded SSFBG sensors connected in serial configuration and figure 3.15 c), d) shows the result of computing the improved identification function $IF(\lambda)$ based on the correlation between the theoretical and measured spectra. The obtained ACP for each sensor corresponds to their central wavelength.

A feasible scenario is simulated by assigning each sensing SSFBG device with a trajectory that can result in partial or total overlapping. The most direct approach is to sweep one of the sensing devices through the second one, which remains at a steady position. This is exemplified in Figure 3.16 a) and b), where the detected wavelength of two sensors in an overlapping scenario ($S2$ swept over $S1$) is depicted as a function of the experiment step. We hereby demonstrate the detection feasibility of any two neighboring sensors overlapping completely.

By working in simulation, it is possible to prove that a set of encoded SSFBG sensors is suitable to be manufactured and tested. Also, it allows to extend the concept and to test the behavior of more intricate sensing structures, Fig-
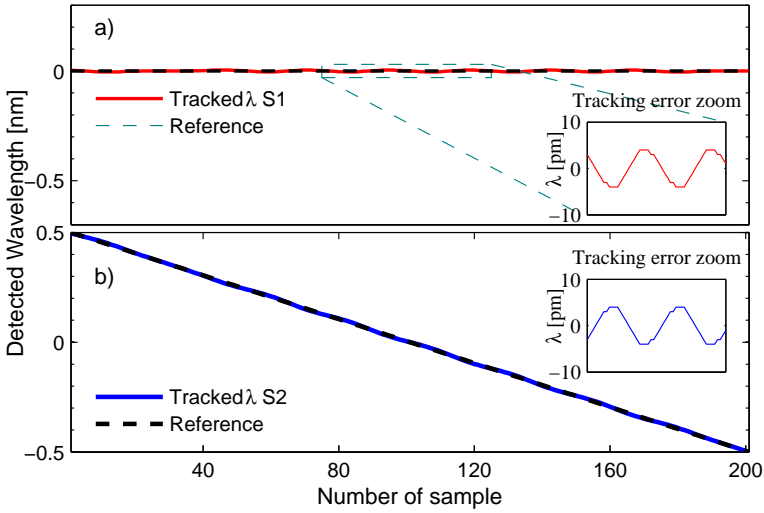
Figure 3.16: The central wavelength of the two SSFBG encoded sensors is simulated in an overlapping scenario. In a), it is shown the retrieved wavelength of the sensor $S1$ that remains still. b) shows the detected wavelength of the sensor $S2$, it follows a linear trajectory that goes through the spectral position of sensor $S1$. Total identification of the two sensors is achieved under overlapping conditions.

ure 3.17 shows the complete simulation scenario for a set of three orthogonal sensors, in a) it is shown the compounded spectrum of the three overlapping sensors while b) shows their corresponding ACP signals (the central wavelength is obtained for the three overlapping sensors). Last, Figure 3.17 c), d) and e) show the trajectory followed by the sensors $S1$, $S2$ and $S3$ respectively and their associated error in the insets. The simulation of the overlapping scenarios was performed with the parameters listed on table 3.1, having into account the considerations regarding the choice of the design parameters made in the last section (3.3.1), seeking low reflectivity devices, with a narrow sub-bands spectral width and the minimum realizable spacing between sub-bands.
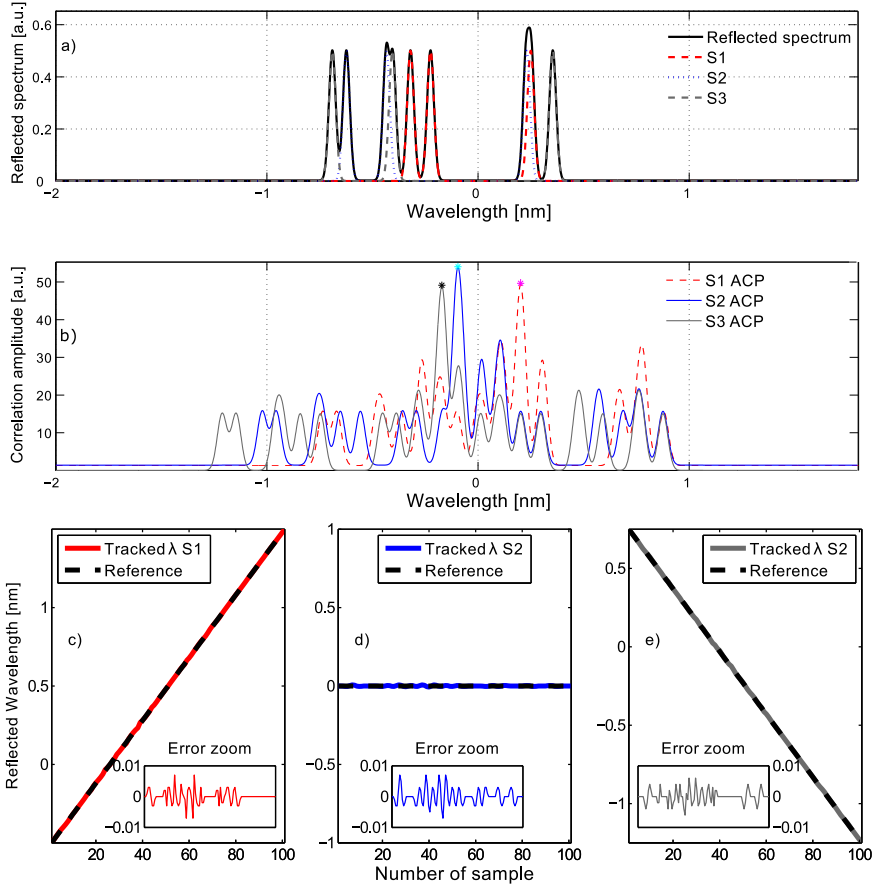
Figure 3.17: The trajectories followed by three orthogonal sensors are obtained through simulation. It is shown the compounded reflected spectrum in a), the auto-correlation product for each sensor is obtained in b). The trajectories followed by the sensors are also plotted: $S1$ in c), $S2$ in d) and $S3$ in e). Each inset shows the obtained error during the overlapping.

3.3.3 Synthesis and manufacturing of the SSFBG devices

Our design methodology is based on the fact that the binary orthogonal codes can be translated to a multi-band SSFBG device simply by assigning reflection sub-bands to the high values in the codeword, once the spectral shape of the sensors, including all the design paramenters, has been defined. A synthesis method can be used to obtain the complex grating index profile $q(z)$. This is performed by an algorithm based on the discrete layer peeling method (DLP) [33] as described in Section 2.1.1 of the previous chapter. Then, the obtained index modulation is discretized and manufactured by the point by point - phase mask writing method outlined in Section 2.1.4. Figure 3.18 shows the index modulation profile obtained for the sensors $S1$ and $S2$. The complexity of each sensor is determined by the spectral width of the device and the FWHM of its sub-bands, although the devices have complex shapes, the manufacturing method is perfectly able to construct the index modulation profiles. Manufactured devices follow the design based on two orthogonal codes. They are written at central wavelengths $S1 = 1546.5$ nm and $S2 = 1547.3$ nm, with reflectivity set to 30%, $FWHM = 40$ pm for each sub-band, and the distance between sub-bands is $\delta\lambda = 0.1$ nm.
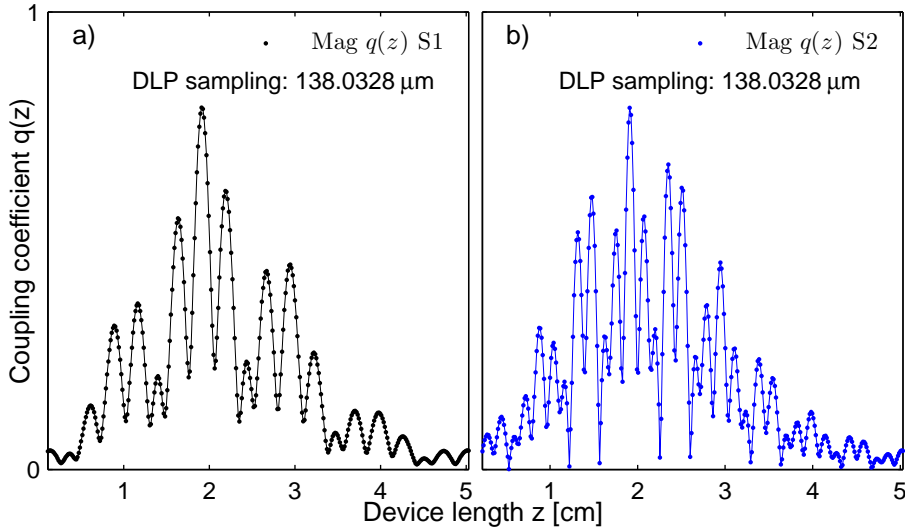
Figure 3.18: Index modulation profile $q(z)$ obtained through the synthesis of the sensors. The index profile (magnitude) of the sensor $S1$ is depicted in a), while b) shows the one obtained for sensor $S2$.

3.4 Experimental results

The two experimental setups used to validate the behavior of the designed sensors are depicted in Figure 3.19 a), b), they are the straightforward representation of the serial and parallel arrangement of the sensors. Generally, a broadband source illuminates the sensors and the reflected signal from the set of sensors is recorded by an Optical Spectrum Analyzer (OSA) and then analyzed in the computer by the correlation algorithm obtaining the central position for each sensor in the network.

When using both, serial and parallel configuration (Figure 3.19 a), b)), the reflectivity of the sensors must be maintained approximately equal in order to avoid the reduction on the ratio ACP/XC, which would affect the detection process. Besides, under the serial approach, the shadowing effect should be prevented by using low-reflectivity devices that do not significantly reduce the power when two or more devices overlap spectraly.
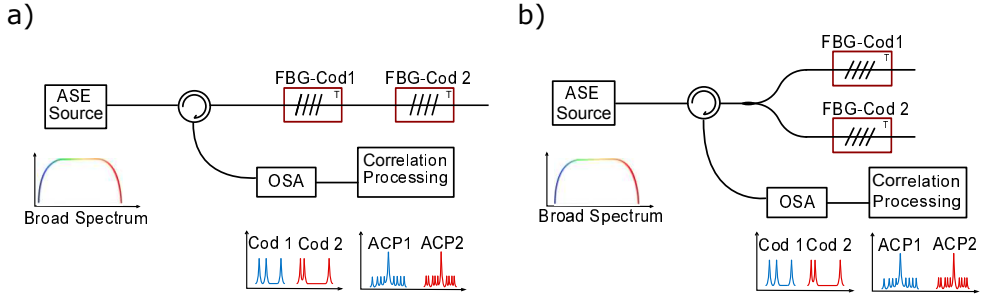
Figure 3.19: Serial and parallel schematic setups used to measure the reflection spectrum of the encoded SSFBG sensors.

3.4.1 Characterization of the devices

The characterization of the devices was performed to assess the spectral shape of the manufactured devices. It was measured directly by using an amplified spontaneous emission (ASE) source and an optical spectrum analyzer (OSA) with 10 pm resolution. Figure 3.20 compares the spectra measured from the manufactured device $S1$ against the designed spectrum.

A very good agreement is shown in Figure 3.20 between the designed and the measured reflection spectra for the manufactured SSFBG devices, which proves that the $q(z)$ profiles have been manufactured with good quality under the DLP sampling definition of 138.0328 μm. Figure 3.21 depicts the same comparison results for the manufacturing of the sensor $S2$. as a result of the comparison between the design and the practical devices, it is reasonable to extend the idea of proving the sensors behavior under overlapping conditions.
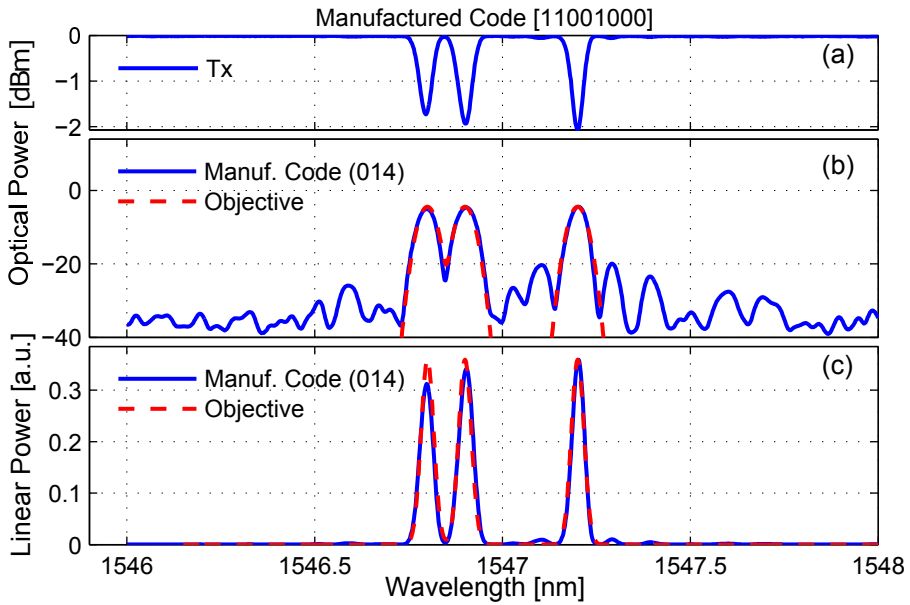
Figure 3.20: Measured spectral response of the manufactured SSFBG sensor $S1$. In a), it is shown the spectral response in transmission; b) compares both, the manufactured response in reflection (blue, continuous line) and the theoretical expected spectrum (red, dashed line); c) shows the reflection response in linear scale. A very good agreement is obtained between the designed and the manufactured devices.
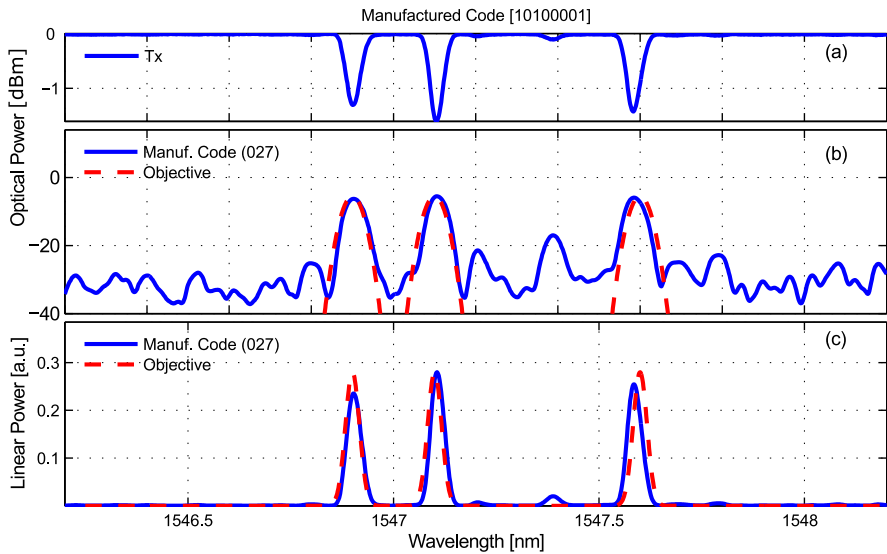
Figure 3.21: Measured spectral response of the manufactured SSFBG sensor $S2$. In a), it is shown the spectral response in transmission; b) compares both, the manufactured response in reflection (blue, continuous line) and the theoretical expected spectrum (red, dashed line); c) shows the reflection response in linear scale. A very good agreement is obtained between the designed and the manufactured devices.

3.4.2   Overlapping detection

We tested the sensing system with the manufactured devices using the experimental setups shown in Figure 3.19, the sensors are stabilized in temperature in order to avoid changes in their wavelength caused by ambient temperature drifts. Wavelength changes are then induced by stretching the optical fiber in a strain platform. The readout measured at the OSA is transferred to a computer where the correlation identification algorithm is run, finally, the sensors are logged in terms of their central wavelength.

The simplest and most effective way to prove the sensors orthogonality is to fix one of the sensors (at a steady wavelength) while the second one is swept over the spectrum. Figure 3.22 depicts the results for the experiment performed in serial configuration. Here, any unbalance between the SSFBG devices power would affect the ratio ACP/XC and therefore the detection error. The opposite occurs when using the parallel configuration (Figure 3.23). At the expense of using a passive splitter, the auto- and cross-correlation signals maintain the same ratio because the reflectivity of each sensor is not affected by the shadowing effect.

By performing these experiments the distinction capacity of the system is verified and most importantly its capacity to find the central wavelength of two sensors when they are overlapping. From this, the number of sensors in an optical sensing network is increased because every pair of neighboring sensors can share the same operational wavelength range. In fact, going to the limit of the orthogonality definition: *o*rthogonal codewords in a set are distinguishable between them and from shifted versions of themselves, it is possible to have two versions of the same SSFBG device in the same operational wavelength, and they are totally identifiable from each other except when totally overlapped (on top of each other). Figure 3.24 depicts the detected reflection spectrum from 3 encoded sensors in the same operational range (two sensors are designed after the $S1$ codeword and one sensor with the shape of sensor $S2$), also in Figure 3.24 it is shown the obtained ACP signal from each sensor, pointing at the central wavelength of each sensor while their reflection spectra are merged. The trajectory followed by each one of the sensors during the experiment is depicted in Figure 3.25, the operational range of the sensor $S2$ overlaps at both sides with one of the $S1$ sensors. This is possible because sensors with the same code can overlap partially without causing the detection system to loose their location. Therefore, the orthogonal features of the sensors have been proved to be useful to detect the central wavelength of encoded sensors under overlapping conditions.
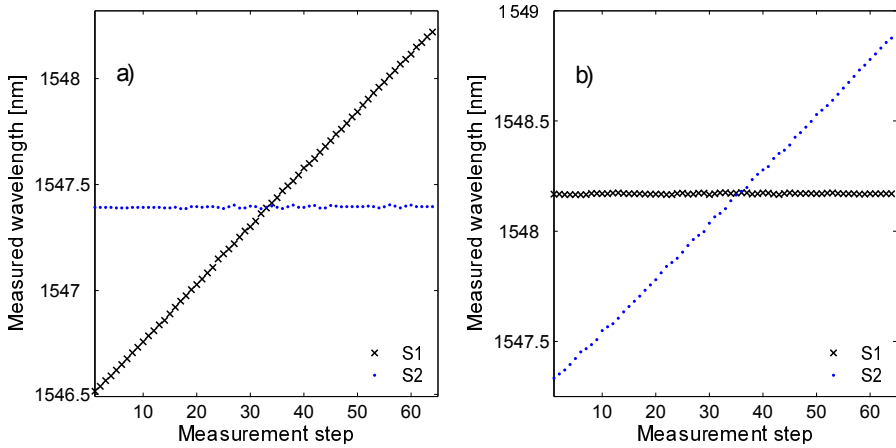
Figure 3.22: Detected wavelength for two sensors under overlapping conditions. Sensors are connected in serial configuration. In a) it is shown the swept of the sensor $S1$ over the sensor $S2$. The analog scenario is shown in b). Total identification of the sensors wavelength is achieved even under overlapping conditions.
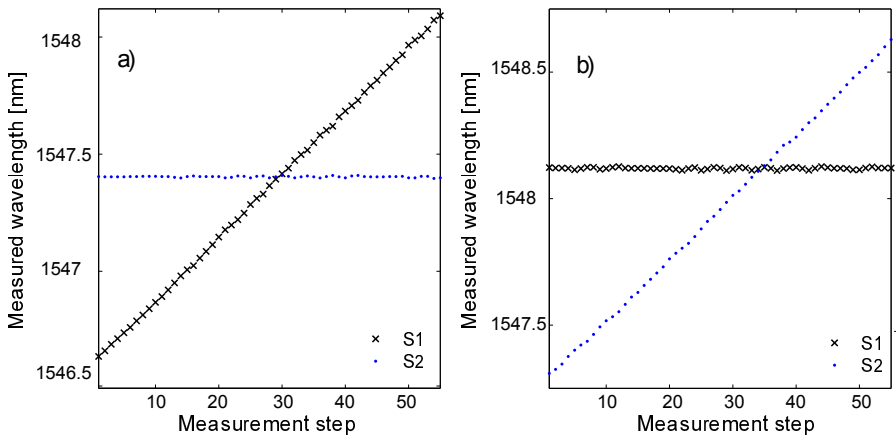
Figure 3.23: Detected wavelength for two sensors under overlapping conditions. Sensors are connected in the parallel configuration. In a) it is shown the swept of the sensor $S1$ over the sensor $S2$. The analog scenario is shown in b). Total identification of the sensors wavelength is achieved even under overlapping conditions.
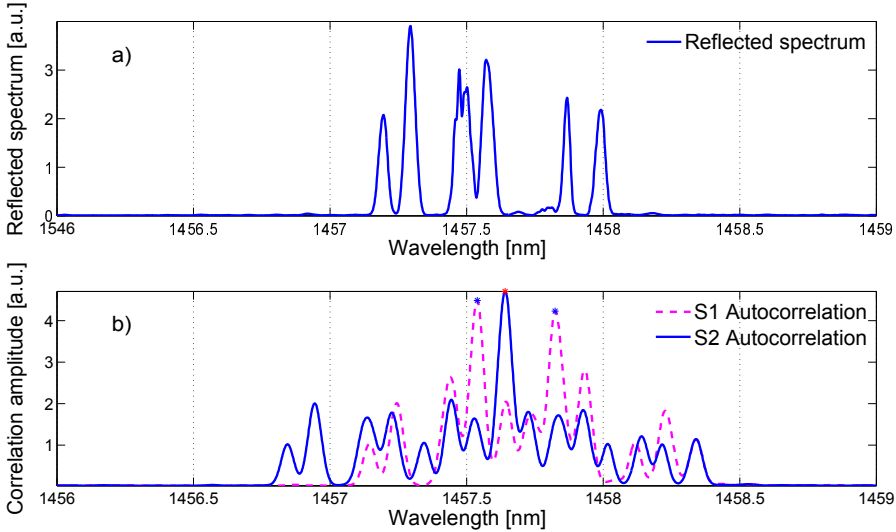
Figure 3.24: Experimental readout of the reflection spectrum from three encoded FBG sensors. In a), it is shown the reflection spectrum of three SSFBG sensors under overlapping conditions. In b), the corresponding correlation product is computed in order to identify the central wavelength through the ACP.

Another experiment was performed to validate the detection of a sensing system with 4 sensors that share the spectrum by pairs. This is the proof of the concept of a sensing system with a CDM-WDM multiplexing scheme. Figure 3.26 illustrates the reflection spectrum recorded for 4 sensors working in the same operational range, which were arranged in two branches, combining the serial and parallel configuration. Figure 3.26 also depicts the ACP obtained for the recorded spectrum, where the 4 wavelengths are located. The magnitude of the ACP for each sensor depends on each sensors reflectivity. Figure 3.27 shows the trajectories followed by the sensors during the experiment.

3.4.3 Error assessment

In the previous sections, the effective use of SSFBG sensors was proved to allow the identification of two or more sensors under overlapping conditions. Still, the overlapping between the sensors causes a determined detection error. This error is due to additional signals in the spectrum affecting the correlation detection function. Any additional signal in the spectrum has an impact
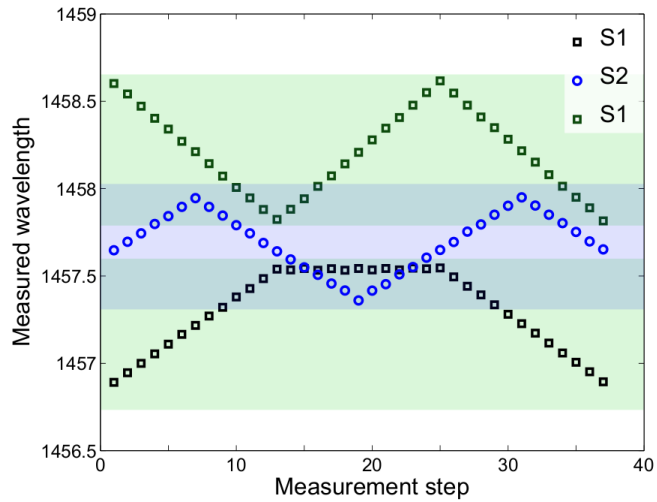
Figure 3.25: Measured wavelength of a sensing system composed of three sensors of two kinds. Sensors $S1$ are designed after the codeword $S1 = [10100001]$ and sensor $S2$ after $S2 = [11001000]$. Orthogonality of the sensors is demonstrated: full overlapping is possible between different sensors while partial overlapping is allowed for sensors designed after the same codeword.
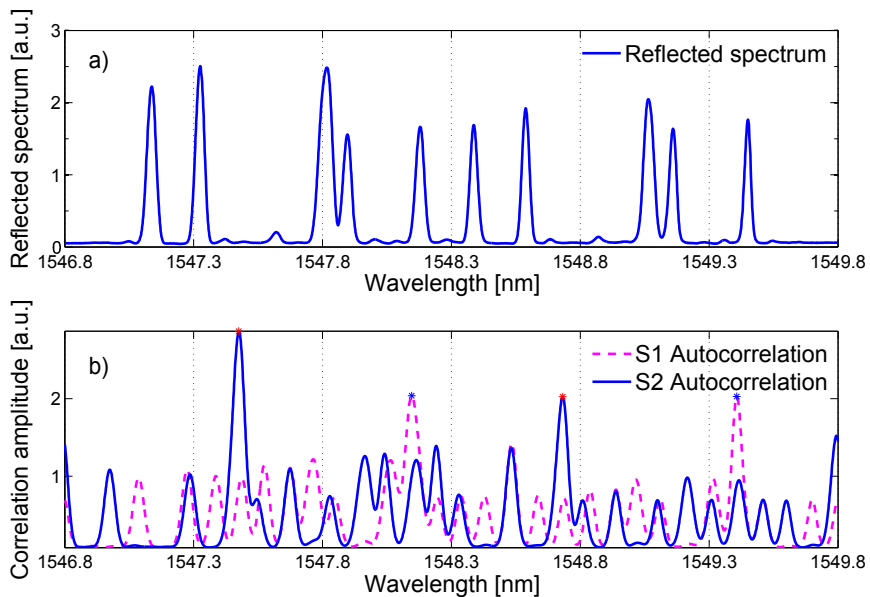
Figure 3.26: Experimental readout of the reflection spectrum from four encoded FBG sensors. In a), it is shown the reflection spectrum of 4 sensors under overlapping conditions. In b), the corresponding correlation product is computed in order to obtain the ACP for each sensor.
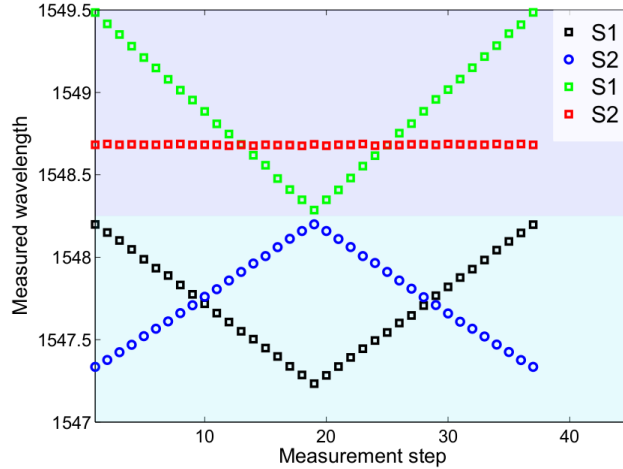
Figure 3.27: Measured wavelength of a sensing system composed of 4 sensors of two kinds. Full overlapping between encoded FBG sensors and CDM-WDM compatibility are demonstrated.

over the cross-correlation signal obtained from a sensor, when this XC values interfere with the auto-correlation signal, the obtained ACP result is shifted.

This error can be easily tracked because it should not be present when the central wavelength of a single sensor is interrogated. i.e. without overlapping. Therefore, an experiment with the two SSFBG sensors was arranged, the idea was to discriminate the error due to the cross-correlation (XC-error) so the obtained sensor wavelengths were measured with and without the interference from a second sensor in the spectrum. It is important to isolate also the human error from the measurements, i.e. the individual and overlapped measurements must be performed with the sensors located at the exact same positions.

The overlapping scenario between two SSFBG encoded sensors was assembled in parallel configuration (using a 50:50 splitter) so that the sensors can be individually switched-off, removing its influence over the other sensor. In this way the readout of the system captures the reflection spectrum of sensor $S1$, sensor $S2$, and sensors $S1 + S2$ during the same experiment.

In the experiment, sensor $S1$ was swept over the spectrum of the sensor $S2$ and viceversa. It is important to have into account that we can not get rid of the systematic error, which is the amount of error caused by all the components
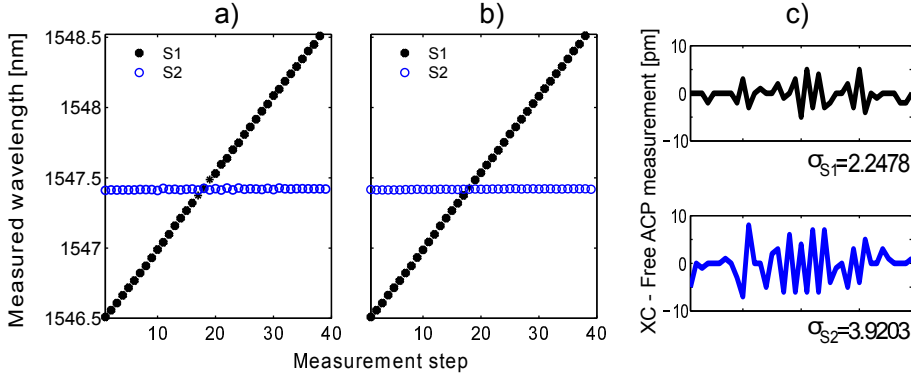
Figure 3.28: Comparison between the wavelength measurement obtained from the overlapping scenario and the one obtained individually during the same experiment is presented in a) and b) respectively. In c), it is plotted the difference between the two set of measurements.

in the system i.e. noise, power looses, etc. Therefore, the total error in the detection system can be written as in (3.3):

$$\sigma E_T = \sqrt{\sigma E_{XC}^2 + \sigma E_{syst}^2} \qquad (3.3)$$

Where σE_{XC}^2 and σE_{syst}^2 are the standard deviation corresponding to the cross-correlation, and the systematic error in the system. Figure 3.28 depicts the detected wavelength for sensors $S1$ and $S2$ when sensor $S1$ is swept through the spectral position of sensor $S2$. Fig. 3.28 a) shows the measurement performed with the two sensors connected simultaneously to the sensing system. Fig. 3.28 b) shows the wavelength of each sensor measured individually during the same experiment, and Fig. 3.28 c) shows the point by point difference between the two cases. The maximum instantaneous error obtained through this comparison is of ± 7 pm.

The maximum error obtained through the comparison between the simultaneous and the individual measurements contains both, the systematic and the XC-error. However, our goal is to isolate the XC-error. To do so, we compared the detected wavelength of the stationary sensor $S2$ with and without the presence of the sensor $S1$ in the spectrum. This is shown in Figure 3.29, indeed, Figure 3.29 a) delimits clearly the overlapping region between the two sensors, the central wavelength shows a bigger error value than the external regions were no overlapping occurs. In this case the standard deviation due to the cross-correlation plus the systematic error is $\sigma E_T = 3.8046$. On the
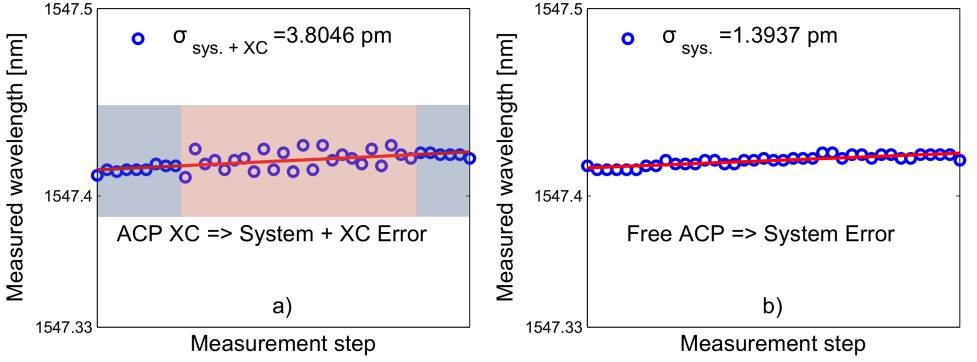
Figure 3.29: Zoomed wavelength measurement for the fixed sensor in the comparison between an overlapped system (a), and the individual measurement (b). In a), it is possible to discriminate the systematic from the XC-error when the two sensors start to merge into each other. b) shows only the systematic error for an individual measurement.

other hand, in Fig. 3.29 b) it is depicted the individually measured wavelength during the same experiment, from this, the standard deviation due to the systematic error is obtained as $\sigma E_{syst} = 1.3937$. Hence, the XC-error is calculated as (3.4):

$$\sigma E_{XC} = \sqrt{\sigma E_T^2 - \sigma E_{syst}^2} \tag{3.4}$$

$$= \sqrt{3.804^2 - 1.393^2} = 3.54 \ pm \tag{3.5}$$

3.5 Conclusion

In this chapter, the amplitude encoded SSFBG sensors have been proposed and subsequently investigated in terms of manufacturing feasibility, detection under overlapping conditions and obtained error. This study provides the framework for designing and validating encoded sensors based on super-structured FBG sensors. The impact of this work is to enhance the capacity of the system regarding the number of sensors than can be deployed in a given spectrum.

The sensors are intended to be manufactured as super-structured FBGs which provide important features such as small spatial size under a single manufacturing process and control over the average refractive index change in the device. The encoded SSFBG sensors are designed after the optical orthogonal

codes (OOCs) that are orthogonal codewords used in this case to shape the amplitude of FBG structures in order to achieve spectral amplitude encoding.

For these devices, numerical simulations were performed in order to obtain insights into how the correlation functions were satisfied regarding orthogonality between the set of sensors. Also, the overlapping scenarios were simulated to guarantee the correct demodulation of each sensor even when the central wavelengths of two or more sensors are overlapping.

A simple, correlation-based demodulation method was proved to retrieve the central wavelength of each sensor in the spectrum. Besides, we have devised a '2-steps' procedure to reduce the error caused by other sensors in the spectrum. By employing this additional step in the detection process, the detection error is eliminated.

The effects of practical SSFBG parameters are simulated and analyzed. Practical manufacturing parameters such as reflectivity, width and detuning of the sub-bands and the device length were analyzed. The simulation work, led us to conclude that the detection method performs better with SSFBG devices with reflectivity values of less than the 70%, mainly due to (and under) the serial configuration approach that produces a shadowing effect between two sensors operating at the same wavelength. Also, the relationship between each sub-band width and the spacing between sub-bands was found to be of 1 : 2 for minimizing the error influence from the cross-correlation signal into the auto-correlation signal that points out the central wavelength of each sensor. Another important parameter is the codewords length, the longer the codeword, the wider the sensors in terms of spectral width. It is worthwhile noting that with the minimum number of orthogonal sensors (therefore the minimum codewords length is = 8 bits), the capacity of the sensing system will be doubled since two encoded SSFBG sensors can be allocated in the same spectral region. Finally, the effect of detuning one of the sensors sub-bands was also investigated: as expected, a clear inverse correlation was found between the detuning of the sensors sub-bands and the detection error. Still, manufacturing procedures are good enough to minimize the detuning of the sub-bands and, when needed, the exact detuning can be loaded in the detection algorithm to totally overcome the effect over the detection error.

With the certainty that all the practical parameters were thoughtfully studied, the manufacturing process was started. The refractive index profile was obtained through a synthesis algorithm and the SSFBG devices were manufactured under a point by point - double exposure methodology. A set of 2 encoded

SSFBG was manufactured; constructed devices were characterized and the experimental overlapping scenarios were carried out. Significantly, results from this stage agreed thoroughly with the simulated scenarios. Total wavelength discrimination was achieved in both, serial and parallel configuration.

The experimental stage not only validated the detection method proposed to retrieve the central wavelength of each sensor in an overlapping scenario, it also allowed us to assess the detection error present in the system due to the interference between the XC and the ACP signals. The central wavelength of each sensor obtained from the compounded measurement (when two sensors overlap) was compared against the individual measurement for each sensor during the same experiment. A total error in the system, i.e. due to the cross-correlation between the sensors plus the systematic error, was found to be: $\sigma_{sys} + \sigma_{XC} = 3.804$ *pm*. While the isolated error due to the XC signals in the system is of $\sigma_{XC} = 3.54$ *pm*. This is a significant result proving that two encoded SSFBG sensors can share the operational range, doubling the capacity of the system, with a penalty of less than $\pm 3\mu\varepsilon$ or $\pm 3°C$ for strain or temperature measurement.

References

[1] J. A. Salehi, "Code division multiple-access techniques in optical fiber networks. i. fundamental principles", *IEEE Transactions on Communications*, vol. 37, no. 8, pp. 824–833, Aug. 1989, ISSN: 0090-6778. DOI: `10.1109/26.31181` (cit. on p. 31).

[2] J. Shah, "Optical code division multiple access", *Opt. Photon. News*, vol. 14, no. 4, pp. 42–47, Apr. 2003. DOI: `10.1364/OPN.14.4.000042` (cit. on p. 31).

[3] P. Prucnal, M. Santoro, and T. Fan, "Spread spectrum fiber-optic local area network using optical processing", *Journal of Lightwave Technology*, vol. 4, no. 5, pp. 547–554, May 1986, ISSN: 0733-8724. DOI: `10.1109/JLT.1986.1074754` (cit. on pp. 31, 32).

[4] W. C. Kwong, P. A. Perrier, and P. R. Prucnal, "Performance comparison of asynchronous and synchronous code-division multiple-access techniques for fiber-optic local area networks", *IEEE Transactions on Communications*, vol. 39, no. 11, pp. 1625–1634, Nov. 1991, ISSN: 0090-6778. DOI: `10.1109/26.111444` (cit. on p. 31).

[5] M. E. Marhic, "Coherent optical cdma networks", *Journal of Lightwave Technology*, vol. 11, no. 5, pp. 854–864, May 1993, ISSN: 0733-8724. DOI: `10.1109/50.233249` (cit. on p. 31).

[6] G. C. Yang, "Some new families of optical orthogonal codes for code-division multiple-access fibre-optic networks", *IEE Proceedings - Communications*, vol. 142, no. 6, pp. 363–368, Dec. 1995, ISSN: 1350-2425. DOI: `10.1049/ip-com:19952304` (cit. on p. 32).

[7] W. Huang and I. Andonovic, "Optimal performance of coherent optical pulse cdma systems based on code and phase synchronisation and interference cancellation", *IEE Proceedings - Optoelectronics*, vol. 145, no. 6, pp. 353–359, Dec. 1998, ISSN: 1350-2433. DOI: `10.1049/ip-opt :19982481` (cit. on p. 32).

[8] E. H. Dinan and B. Jabbari, "Spreading codes for direct sequence cdma and wideband cdma cellular networks", *IEEE Communications Magazine*, vol. 36, no. 9, pp. 48–54, Sep. 1998, ISSN: 0163-6804 (cit. on p. 32).

[9] D. Zaccarin and M. Kavehrad, "An optical cdma system based on spectral encoding of led", *IEEE Photonics Technology Letters*, vol. 5, no. 4, pp. 479–482, Apr. 1993, ISSN: 1041-1135. DOI: `10.1109/68.212705` (cit. on p. 32).

[10] G.-C. Yang and W. C. Kwong, "Performance comparison of multiwavelength cdma and wdma+cdma for fiber-optic networks", *IEEE Transactions on Communications*, vol. 45, no. 11, pp. 1426–1434, Nov. 1997, ISSN: 0090-6778. DOI: `10.1109/26.649764` (cit. on p. 32).

[11] L. Tancevski and I. Andonovic, "Wavelength hopping/time spreading code division multiple access systems", *Electronics Letters*, vol. 30, no. 17, pp. 1388–1390, Aug. 1994, ISSN: 0013-5194. DOI: `10.1049/el:19940942` (cit. on p. 32).

[12] H. Yin and D. Richardson, *Optical Code Division Multiple Access Communication Networks: Theory and Applications*. Springer Berlin Heidelberg, 2009, ISBN: 9783540684688 (cit. on p. 33).

[13] R. C. BOSE, "On the construction of balanced incomplete block designs", *Annals of Eugenics*, vol. 9, no. 4, pp. 353–399, 1939. DOI: `10.1111/j .1469-1809.1939.tb02219.x`. eprint: `https://onlinelibrary.wiley .com/doi/pdf/10.1111/j.1469-1809.1939.tb02219.x` (cit. on p. 33).

[14] R. M. Wilson, "Cyclotomy and difference families in elementary abelian groups", *Journal of Number Theory*, vol. 4, no. 1, pp. 17–47, 1972, ISSN: 0022-314X. DOI: `https://doi.org/10.1016/0022-314X(72)90009-1` (cit. on p. 33).

[15] H. Hanani, "Balanced incomplete block designs and related designs", *Discrete Mathematics*, vol. 11, no. 3, pp. 255–369, 1975, ISSN: 0012-365X. DOI: https://doi.org/10.1016/0012-365X(75)90040-0 (cit. on p. 33).

[16] H. Chung and P. V. Kumar, "Optical orthogonal codes-new bounds and an optimal construction", *IEEE Transactions on Information Theory*, vol. 36, no. 4, pp. 866–873, Jul. 1990, ISSN: 0018-9448 (cit. on p. 33).

[17] G.-C. Yang, "Variable weight optical orthogonal codes for cdma networks with multiple performance requirements", *IEEE Transactions on Communications*, vol. 44, no. 1, pp. 47–55, Jan. 1996, ISSN: 0090-6778. DOI: 10.1109/26.476096 (cit. on p. 33).

[18] F. Chung, J. Salehi, and V. Wei, "Optical orthogonal codes: Design, analysis and applications", *Information Theory, IEEE Transactions on*, vol. 35, no. 3, pp. 595–604, May 1989, ISSN: 0018-9448 (cit. on pp. 33, 35).

[19] J. Ko, Y. Kim, and C.-S. Park, "Fiber Bragg grating sensor network based on code division multiple access using a reflective semiconductor optical amplifier", *Microwave and Optical Technology Letters*, vol. 52, no. 2, pp. 378–381, 2010, ISSN: 1098-2760. DOI: 10.1002/mop.24913 (cit. on p. 34).

[20] K. Koo, A. Tveten, and S. Vohra, "Dense wavelength division multiplexing of fibre Bragg grating sensors using CDMA", *Electronics Letters*, vol. 35, no. 2, pp. 165–167, Jan. 1999, ISSN: 0013-5194. DOI: 10.1049/el:19990135 (cit. on p. 34).

[21] A. D. Kersey, A. Dandridge, and M. A. Davis, "Low-crosstalk code-division multiplexed interferometric array", *Electronics Letters*, vol. 28, no. 4, pp. 351–352, Feb. 1992, ISSN: 0013-5194. DOI: 10.1049/el:19920219 (cit. on p. 34).

[22] H. Lee, "Multiple fiber Bragg grating sensor system using code-division multiple access", *Appl. Opt.*, vol. 41, no. 25, pp. 5245–5248, Sep. 2002. DOI: 10.1364/AO.41.005245 (cit. on p. 34).

[23] J. Chen, H. Jiang, T. Liu, and X. Fu, "Wavelength detection in FBG sensor networks using least squares support vector regression", *Journal of Optics*, vol. 16, no. 4, 2014 (cit. on p. 34).

[24] H. Jiang, J. Chen, and T. Liu, "Wavelength Detection in Spectrally Overlapped FBG Sensor Network Using Extreme Learning Machine", *Photonics Technology Letters, IEEE*, vol. 26, no. 20, pp. 2031–2034, Oct. 2014, ISSN: 1041-1135. DOI: 10.1109/LPT.2014.2345062 (cit. on p. 34).

[25]   H. Jiang, J. Chen, T. Liu, and W. Huang, "A novel wavelength detection technique of overlapping spectra in the serial wdm fbg sensor network", *Sensors and Actuators A: Physical*, vol. 198, no. 1, pp. 31–34, 2013, ISSN: 0924-4247. DOI: `http://dx.doi.org/10.1016/j.sna.2013.04.023` (cit. on p. 34).

[26]   D. Liu, K. Tang, Z. Yang, and D. Liu, "A Fiber Bragg Grating Sensor Network Using an Improved Differential Evolution Algorithm", *Photonics Technology Letters, IEEE*, vol. 23, no. 19, pp. 1385–1387, Oct. 2011, ISSN: 1041-1135. DOI: `10.1109/LPT.2011.2160992` (cit. on p. 34).

[27]   L. Chen, "Optical code-division multiple-access enabled by fiber bragg grating technology", in *Optical Code Division Multiple Access Fundamentals and Applications*, CRC Press, Dec. 2005, pp. 111-164–. DOI: `10.1201/9781420026610.ch4` (cit. on p. 35).

[28]   S. Ayotte, M. Rochette, J. Magne, L. Rusch, and S. LaRochelle, "Experimental verification and capacity prediction of FE-OCDMA using superimposed FBG", *Lightwave Technology, Journal of*, vol. 23, no. 2, pp. 724–731, Feb. 2005, ISSN: 0733-8724. DOI: `10.1109/JLT.2004.839984` (cit. on p. 35).

[29]   C. Tian, Z. Zhang, M. Ibsen, P. Petropoulos, and D. J. Richardson, "A 16-channel reconfigurable ocdma/dwdm system using continuous phase-shift ssfbgs", *IEEE Journal of Selected Topics in Quantum Electronics*, vol. 13, no. 5, pp. 1480–1486, Sep. 2007, ISSN: 1077-260X. DOI: `10.1109/JSTQE.2007.897668` (cit. on p. 35).

[30]   C. Huang, W. Jing, K. Liu, Y. Zhang, and G.-D. Peng, "Demodulation of Fiber Bragg Grating Sensor Using Cross-Correlation Algorithm", *Photonics Technology Letters, IEEE*, vol. 19, no. 9, pp. 707–709, May 2007, ISSN: 1041-1135. DOI: `10.1109/LPT.2007.895422` (cit. on p. 38).

[31]   C. Caucheteur, K. Chah, F. Lhomme, M. Blondel, and P. Megret, "Autocorrelation demodulation technique for fiber bragg grating sensor", *Photonics Technology Letters, IEEE*, vol. 16, no. 10, pp. 2320–2322, Oct. 2004, ISSN: 1041-1135. DOI: `10.1109/LPT.2004.833106` (cit. on p. 38).

[32]   V. Jayaraman, Z. M. Chuang, and L. A. Coldren, "Theory, design, and performance of extended tuning range semiconductor lasers with sampled gratings", *IEEE Journal of Quantum Electronics*, vol. 29, no. 6, pp. 1824–1834, Jun. 1993, ISSN: 0018-9197. DOI: `10.1109/3.234440` (cit. on p. 47).

[33]   J. Skaar, L. Wang, and T. Erdogan, "On the synthesis of fiber bragg gratings by layer peeling", *IEEE Journal of Quantum Electronics*, vol. 37, no. 2, pp. 165–173, Feb. 2001, ISSN: 0018-9197. DOI: `10.1109/3.903065` (cit. on p. 55).

Chapter 4

Phase and amplitude encoded sensors

4.1 Introduction

In chapter 3, SSFBG sensing devices were proposed to address the problem of the spectrally overlapping adjacent sensors. The amplitude encoding of the devices was designed after the well known Optical Orthogonal Codes (OOCs), obtaining as a result sets of 2 and 3 adjacent sensors that can be identified by means of the correlation product between the total measured spectrum and each sensor single expected spectral response.

The encoding in amplitude showed to be useful to provide each sensor with additional information that can be helpful in solving the overlapping detection problem between adjacent sensors. It also proved itself able to be used in sync with more common multiplexing approaches like wavelength division multiplexing for example, consequently enhancing the number of sensors that can be deployed in any sensing network.

The validation of the sensing system based on amplitude encoding allowed us to propose a more complex approach that relies basically on the use of both, phase

Table 4.1: A Walsh codes family with length = 4.

Walsh codes
$[+1+1+1+1[$
$[+1-1+1-1[$
$[+1+1-1-1[$
$[+1-1-1+1[$

and amplitude patterns to design the spectral response of an encoded sensor. Thus, the codewords used to shape the sensor could be bipolar code families instead of unipolar codewords, this would potentially reduce the multiple access interference (MAI) due to the fact that bipolar codes feature close to zero correlation functions (i.e. to diminish the cross-correlation signal influence over the detection of other sensors in the spectrum).

There are different families of bipolar codes that are widely used due to their good correlation properties, for instance, 'Gold sequences' [1], [2] have been used to prove OCDMA communication systems [3]. The Gold codes are an important set of codes specially suitable for asynchronous systems. Another important set of codes is the family known as 'Walsh codes' [4], which features zero cross-correlation between the codes of a family when they are fully synchronized in time.

Nevertheless, the bipolar codes used in the literature are suited and designed to work as en/decoders in communication systems [5]. There is a big difference between sets of codewords created for communication systems and the ones that can be used in a sensing system. This has to do with the cyclical behavior of the codes, i.e. bipolar codes are designed to be orthogonal between them but not between shifted versions of themselves. To illustrate this, we can take as an example the family of Walsh codes with length = 4 represented in table 4.1:

The correlation product of the Walsh codes listed in Table 4.1 is zero because of the bits sign, nevertheless, from Table 4.1 it is straightforward that the correlation properties does not hold for shifted versions of the codewords.

The main feature of bipolar codes is that the elements in the codeword have a sign (± 1). This contributes to the good correlation behavior, but, from the FBG technology point of view, this is not practical. A FBG device can be tailored to have 'positive' reflection wavelengths spaced according to a given

codeword but it is not practical to think about positive and negative terms represented by means of a FBG device. Still, some approaches have implemented the unipolar version of bipolar codes, i.e. M-sequences, Walsh-Hadamard codes or modified quadratic congruence codes (MQC) [6].

OCDMA can be implemented with systems based on FBG devices. Both, coherent and incoherent approaches are suitable to be implemented. Basically, the FBG will perform the same task, it will have some reflection wavelengths spaced in wavelength and/or time, see Figure 4.1. In Figure 4.1 a) it is represented the incoherent approach, where a broadband spectral source is used to illuminate the grating device, which filters out the broad spectrum reflecting a spectral shape according to the specific codeword. In the coherent approach, Figure 4.1 b), a pulsed signal is input to the system, as the pulse goes through the whole FBG device, it gets reflected with a certain phase value due to each reflection wavelength in the encoder (additional phase delay would be added if the gratings are physically separated).
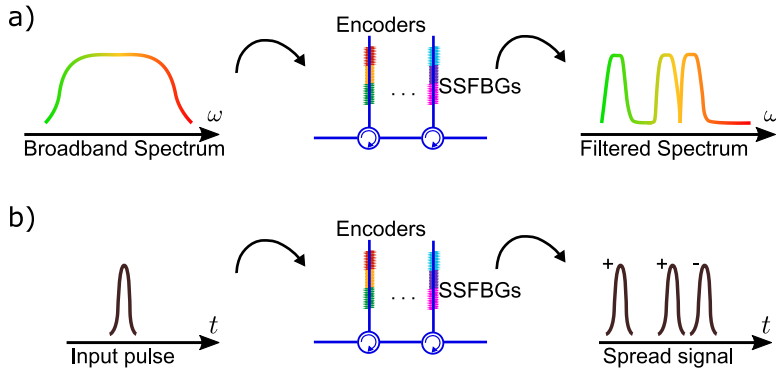
Figure 4.1: Working pinciple of super-structured FBG en/decoders, SSFBG devices can be employed to achieve incoherent or coherent encoding. In a), the SSFBG filters out (encodes) the optical spectrum from a broad-band source (incoherent encoding). In b), a pulse is coherently encoded in time by spreading the input pulse according to a given phase pattern.

As mentioned before, the FBG devices designed after bipolar codewords are developed to spread a pulse with a given phase pattern in time [7]. Therefore, they are not suitable to be distinguished through the correlation between them. i.e. they are not suited to work as sensors in a sensing system.

As the goal of this research is to propose methodologies and optical devices to encode the sensors in a network, we wanted to introduce a set of codes, that includes amplitude and phase terms just like bipolar codes, aiming to achieve

better correlation behavior and potentially increase the number of multiplexed sensors. To do this, we needed to come up not only with the SSFBG encoders but also with their interrogation method.

The design of the codewords is based on a dual-band mapping from bipolar to unipolar spectral shapes. This means that the translation between the manufactured spectral shape and the full codeword with amplitude and phase terms is performed at the interrogation stage. To understand this, we fully describe the encoding mechanism:

The first component in this encoding approach is the amplitude of the sensors. As explained in Chapter 3, amplitude encoding is achieved, using FBG-based devices, by translating a binary codeword ('0', '1') into the activation or deactivation of a defined sub-band in a SSFBG device composed of the necessary number of sub-bands to represent the binary codeword. The second encoding parameter is the phase of each sub-band, this means that the reflected waveform from each sub-band can be phase-shifted by a fixed value depending on the codeword. Thus, two consecutive sub-bands can be designed to have a relative phase difference ('0', 'π') between them.

So, we need an interrogation methodology in order to obtain a bipolar encoding (with $\pm$ sign) from SSFBG devices featuring binary amplitude values and relative phase shifts between consecutive sub-bands. It is noteworthy that this translating procedure should be performed without affecting the measurement process (ideally it will not include pre- or post-processing stages). Therefore we have proposed an interrogation technique based on the use of a dual-wavelength source that scans the entire working spectrum of the sensors. Through the scanning procedure, the phase value between two adjacent sub-bands can be retrieved. It is therefore important that the distance between sub-bands in the sensor matches the separation of the dual-wavelength scanning source. A simple and cost-effective way to obtain a dual-wavelength source is through the single side band (SSB) modulation of a laser.

The working principle of the interrogation method that translates the unipolar nature of a SSFBG device into a bipolar codeword is exemplified in Figure 4.2. An SSFBG device is described by two codewords, the amplitude and the phase codewords. For this case, let us consider (Figure 4.2 a)) a device with five active reflection sub-bands, corresponding to the amplitude codeword: $a = [1\ 1\ 1\ 1\ 1]$, and the phase shifts between these sub-bands according to the phase codeword: $f = [0\ \pi\ \pi\ 0\ 0]$. The sub-bands of the sensor are distanced in frequency (wavelength) a given value: $\delta\omega$. This value matches the radio-frequency distance,
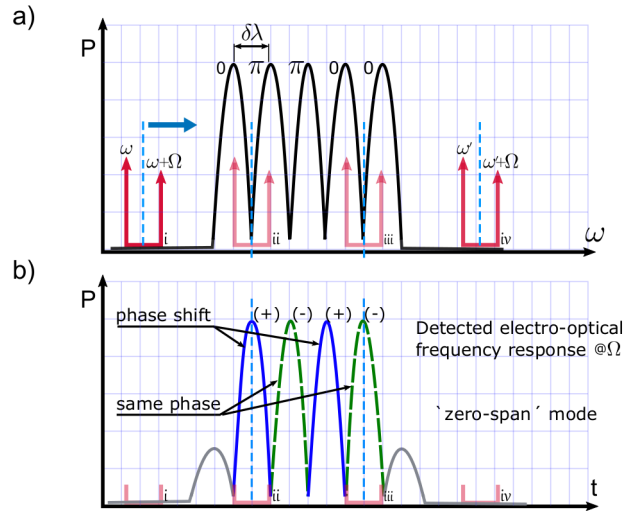
Figure 4.2: Illustration of the interrogation method used to retrieve the frequency response of the sensing network in phase and amplitude. In a), the dual-wavelength source scanning process is depicted. b) depicts the electro-optical frequency response for the sensing device, amplitude and phase response from the sensing array are obtained.

Ω, between the two interrogating tones of the tunable dual-wavelength source. In addition, Figure 4.2 b) shows the expected interrogated signal, assuming photo-detection at the radio-frequency Ω during the dual-wavelength scanning procedure. The interrogation method produces a single detected sub-band for each pair of sub-bands in the SSFBG device, and the detected sub-bands feature a relative phase value depending on the phase relationship between the actual SSFBG device. Figure 4.2 highlights four phases of the interrogation process (i, ii, iii, iv), stages ii and iii represent the two possibilities of phase detection, i.e. the presence or not of a differential phase-shift.

This chapter presents the design, manufacturing and validation of FBG-based sensors encoded in both, phase and amplitude. The encoded sensors are manufactured as specialized SSFBG devices according to the dual-wavelength interrogation methodology devised specifically for this sensing system. Despite the fact that other dual-wavelength interrogation approaches have been proposed before [8], our interrogation technique differs in that we use the dual-wavelength source to characterize the network not only in amplitude, we also obtain its phase pattern. Therefore we can apply the correlation algorithm as a post-processing tool to decode and identify the central wavelength of each

sensor in the working spectrum even under overlapping conditions. The actual advantage of encoding the sensors relies on the addition of a multiplexing dimension (i.e. code multiplexing), which allows the arrangement of more sensors in the spectrum since they are mutually orthogonal between them so they can share their operational range. Our approach shows a clear advantage over post-processing bio-inspired techniques [9]–[12] employed to asses the wavelength of overlapping FBG sensors because our sensors are essentially orthogonal by definition, so their identification follows a straightforward procedure without using sophisticated computational techniques.

The rest of the chapter is organized as follows: Section 4.2 reports on the design of the codewords and how they are used to shape the proposed SSFBG encoded sensors, also a look into the interrogating methodology is offered since it is related to the selection of the codewords. In Section 4.3, the practical aspects of the sensors are discussed: the manufacturing process is reported, the method to retrieve the central wavelength of each sensor is disclosed, manufactured devices are characterized, not only by contrasting their amplitude spectra against the design but also the relative phase shift between the interrogated sub-bands is measured. This section ends with the experimental validation of the three manufactured devices, their central wavelength is measured in an overlapping scenario and the induced error is assessed. Finally some conclusions are presented in Section 4.4.

4.2 Principle

In this section we discuss the design process followed to obtain a set of mutually orthogonal SSFBG sensors. This set of sensors has the particularity of being encoded in amplitude and phase. We address the technical formulation of the proposed devices from the point of view of the whole sensing system, i.e. considering also the interrogation and post-processing schemes.

4.2.1 Design

The first consideration to get into the design of the SSFBG sensors has to do with the practical parameters needed to manufacture the devices. Each SSFBG sensor shape in the network is established by a number of parameters that can be optimized either to facilitate their detection or to adapt the sensors behavior to the network characteristics (e.g. network topology could require higher/lower reflectivity values). The main descriptor parameters in our SSFBG sensors are

of course the amplitude and phase codewords (a_k, f_k) that define the sub-bands distribution. Still, other important design parameters are the spacing between slots $\delta\lambda$ (this wavelength spacing matches the microwave modulation frequency which is set at $10\ GHz$. With $\delta\nu = \frac{c}{\lambda^2}\delta\lambda$ the wavelength spacing is $\sim 0.08\ nm$), the sub-bands linewidth $\Delta\lambda_{FWHM}$ and the reflectivity of the sensors R. The whole frequency response of the system is described in equation (4.1) for a set of K sensors, each one with N sub-bands, and a reflectivity pattern $(R(\lambda))$.

$$H(\lambda) = \sqrt{R(\lambda)} \cdot \exp(j\pi \cdot f_k) \tag{4.1a}$$

$$R(\lambda) = \sum_{k=1}^{K} \sum_{p=-N/2+1}^{N/2} a_k(p) \cdot \bar{R} \cdot \\ \exp\left(-\left(\frac{\lambda - \lambda_{B_k} - \Delta\lambda_{B_k} - (\delta\lambda \cdot p - \delta\lambda/2 - N/2)}{\Delta\lambda_{FWHM}} \right)^2 \right) \tag{4.1b}$$

The frequency response of the encoded sensors in equation (4.1) is composed of a phase component for each sub-band (determined by the phase codeword f_k) and a magnitude component determined by the reflection spectrum of each sensor $(R(\lambda))$.

In the reflecion spectrum described in equation (4.1b), the kth sensor with N sub-bands, amplitude and phase codewords (a_k, f_k) is represented in terms of the design parameters: $\bar{R}$ is the reflectivity of each sensor, $\delta\lambda$ is the spectral spacing between the slots, each sub-band linewidth $\Delta\lambda_{FWHM}$ is determined by the Full Width Half Maximum $(FWHM)$ value and, $\Delta\lambda_{B_k}$ represents the induced wavelength shift. The sub-bands shape was chosen as Gaussian, nevertheless any other realizable shape is compatible with the encoding proposal.

In order to obtain a set of sensors mutually orthogonal with each other we take some concepts from optical orthogonal codes (OOC), which are binary codewords used in Optical Code Division Multiple Access (OCDMA) communication systems; in Chapter 3, OOCs were used to shape the amplitude pattern of a SSFBG device. Here we use the same concept with the addition of phase encoding to the reflecting sub-bands. This is represented in equation (4.1), by the inclusion (or not) of the phase term $\exp(j\pi)$ to the active sub-bands. An important practical requirement is that at least two consecutive active sub-bands are necessary in order to establish the phase difference between them in the interrogation stage. The effect achieved by adding phase encoding to the sensors can be seen as a new dimension in the amplitude encoding, going from binary $(0, 1)$ to ternary encoding since a sign is added $(0, +1, -1)$.
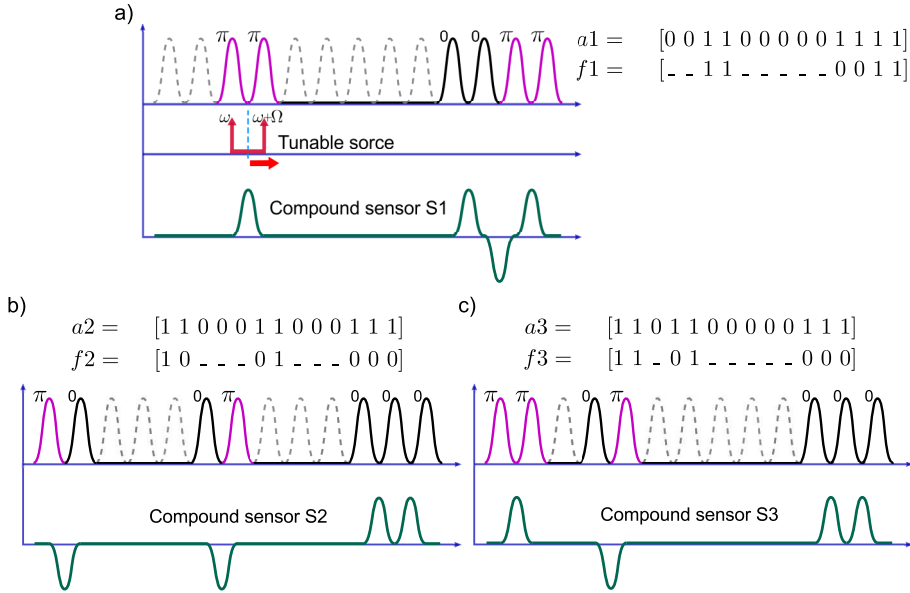
Figure 4.3: Set of three independent sensors designed according to the amplitude and phase codewords reported in table 4.2. a), b) and c) depict the wavelength sub-band distribution for each SSFBG device as well as their compound signals after interrogation through the dual-wavelength scanning.

A set of three, amplitude and phase, codewords is selected as exemplified in table 4.2, these codewords are interpreted in increasing wavelength as described in equation (4.1) and have a bit length of thirteen positions, meaning that each SSFBG device features thirteen slots to allocate the respective reflection sub-bands according to the codewords a_k and f_k. However, due to the dual-wavelength interrogation principle, the retrieved information from each sensor consists of twelve sub-bands. For example the first sensor (S1) is constructed by the codewords $a_1 = [0\ 0\ 1\ 1\ 0\ 0\ 0\ 0\ 0\ 1\ 1\ 1\ 1]$ in amplitude, and $f_1 = [0\ 0\ 1\ 1\ 0\ 0\ 0\ 0\ 0\ 0\ 0\ 1\ 1]$ in phase. Hence, it is composed of 6 sub-bands corresponding to the 1's in the amplitude codeword a_1. In turn, the phase value for each sub-band is determined by the codeword f_1, that enables the factor $\exp(j\pi)$ at the nonzero bit positions. Figure 4.3 a), b) and c) depicts the equivalent sub-band distribution for the set of sensors in table 4.2, as well as their compound interrogated signal. A change of phase between consecutive sub-bands is translated to a negative sign in the detected shape, likewise, two adjacent sub-bands without phase change produce a detected signal with positive sign.

Table 4.2: Set of three sensors represented by their amplitude and phase codewords

Sensor		Codeword
S1	a_1	[0 0 1 1 0 0 0 0 0 1 1 1 1]
	f_1	[0 0 1 1 0 0 0 0 0 0 0 1 1]
S2	a_2	[1 1 0 0 0 1 1 0 0 0 1 1 1]
	f_2	[1 0 0 0 0 0 1 0 0 0 0 0 0]
S3	a_3	[1 1 0 1 1 0 0 0 0 0 1 1 1]
	f_3	[1 1 0 0 1 0 0 0 0 0 0 0 0]

4.2.2 Interrogation

The interrogation method has been described briefly in the past sections, now we will detail this process from the theoretical perspective. To do so, it is necessary to define the source used to illuminate the sensors, and formulate its interaction with the sensing array. The dual-wavelength source (input to the sensing array) is described by equation ((4.2)).

$$
\begin{aligned}
E_{in}(t) &= A_a \exp\left(i\left[\omega_a t + \varphi(t)\right]\right) + A_b \exp\left(i\left[\omega_b t + \varphi(t)\right]\right) \\
&= E_a(t) + E_b(t)
\end{aligned}
\tag{4.2}
$$

where ω_a and ω_b are the general expressions for the two optical angular frequencies, and A_a, A_b represent each tone amplitude. Equation (4.2) represents a general dual-wavelength source, using single side band modulation (SSB) at a microwave frequency Ω the terms are: $\omega_a = \omega_0$, $\omega_b = \omega_0 + \Omega$, besides, with right-$SSB$ modulation we get $A_a > A_b$. The term $\varphi(t)$ in equation (4.2) describes the random variations in the optical phase of the CW source; this parameter is considered the same in the two tones because they are obtained through SSB modulation of the original source.

As a result, the interrogating signal E_{in} is composed of two tones (E_a, E_b in equation (4.2)) separated in frequency by $\Delta\omega = \omega_a - \omega_b$. E_{in} is swept over the sensors operational range and reflected by the sensing elements in the network. Here we consider the full overlapping scenario between two neighboring sensors, this scheme is adequate to analyze the behavior of the network and can be extended to larger sensing networks. Therefore, the reflected signal from the sensing network (E_{out}) would be the product between the dual-wavelength source and the frequency response of the sensors, written as in equation ((4.3)):

$$E_{out} \propto [H_{a1} \exp(i\phi_{a1}) \cdot E_a(t) + H_{b1} \exp(i\phi_{b1}) \cdot E_b(t)]$$
$$+ [H_{a2} \exp(i\phi_{a2}) \cdot E_a(t - \Delta t) + H_{b2} \exp(i\phi_{b2}) \cdot E_b(t - \Delta t)] \qquad (4.3)$$

Where $H_{ak} \exp(i\phi_{ak})$ are the amplitude and phase response of the kth sensor in the lower sub-band ω_a. In the same way the term $H_{bk} \exp(i\phi_{bk})$ corresponds to the upper sub-band ω_b. Notice that the 2nd sensor in the network gets delayed by Δt regarding sensor 1, due to the difference between their fiber paths.

In a 'square-law' detector, the detected photocurrent is proportional to:

$$i(t) \propto E_{out} \cdot E_{out}^* \qquad (4.4)$$

So, from equations ((4.3)) and ((4.4)) the expected beating terms in the photodetector are listed in equations (4.5) to (4.7).

First, we have the beating terms falling in the baseband region, these are represented in equations (4.5)

$$\left(H_{a1}^2 + H_{a2}^2\right)|E_a|^2 + \left(H_{b1}^2 + H_{b2}^2\right)|E_b|^2 \qquad (4.5a)$$

$$H_{a1}H_{a2}\left[\exp(i(\phi_{a1} - \phi_{a2}))\,E_a(t)E_a^*(t - \Delta t)\ +\right.$$
$$\left.\exp(-i(\phi_{a1} - \phi_{a2}))E_a^*(t)E_a(t - \Delta t)\right] \qquad (4.5b)$$

$$H_{b1}H_{b2}\left[\exp(i(\phi_{b1} - \phi_{b2}))\,E_b(t)E_b^*(t - \Delta t)\ +\right.$$
$$\left.\exp(-i(\phi_{b1} - \phi_{b2}))E_b^*(t)E_b(t - \Delta t)\right] \qquad (4.5c)$$

Then, we will call *direct terms* to those terms created by the two interrogating bands being reflected from a unique sensor, they are expressed in equations (4.6).

$$H_{a1}H_{b1}\left[\exp(i(\phi_{a1} - \phi_{b1}))\,E_a(t)E_b^*(t)\ +\right.$$
$$\left.\exp(-i(\phi_{a1} - \phi_{b1}))E_a^*(t)E_b(t)\right] \qquad (4.6a)$$

$$H_{a2}H_{b2}\left[\exp(i(\phi_{a2} - \phi_{b2}))\,E_a(t - \Delta t)E_b^*(t - \Delta t)\ +\right.$$
$$\left.\exp(-i(\phi_{a2} - \phi_{b2}))E_a^*(t - \Delta t)E_b(t - \Delta t)\right] \qquad (4.6b)$$

On the other hand, the terms proceeding from two different sensors beating the two wavelengths are called the *cross terms*, they are represented in equations (4.7).

$$H_{a1}H_{b2}\left[\exp(i(\phi_{a1} - \phi_{b2}))\,E_a(t)E_b^*(t - \Delta t)\ +\right.$$
$$\left.\exp(-i(\phi_{a1} - \phi_{b2}))E_a^*(t)E_b(t - \Delta t)\right] \tag{4.7a}$$

$$H_{b1}H_{a2}\left[\exp(i(\phi_{a2} - \phi_{b1}))\,E_b(t)E_a^*(t - \Delta t)\ +\right.$$
$$\left.\exp(-i(\phi_{a2} - \phi_{b1}))E_b^*(t)E_a(t - \Delta t)\right] \tag{4.7b}$$

In order to develop the *direct* and *cross* terms, we need to compute the different products $(E_a(t) \cdot E_b(t))$ from equations (4.6) and (4.7). It is important to note that the *direct* and *cross* terms oscillate at the fixed microwave frequency value $\Delta\omega = \Omega$. The frequency response of the sensing network is then measured as the electro-optical frequency response at the modulation frequency (Ω). Hence, the detected photocurrent related to *direct* and *cross* terms is obtained as expressed in the equations set (4.8).

$$i_{d1} = 2A_aA_bH_{a1}H_{b1}\cos(\Delta\omega t + (\phi_{a1} - \phi_{b1})) \tag{4.8a}$$

$$i_{d2} = 2A_aA_bH_{a2}H_{b2}\cos(\Delta\omega(t - \Delta t) + (\phi_{a2} - \phi_{b2})) \tag{4.8b}$$

$$i_{x1} = 2A_aA_bH_{a1}H_{b2}\cos(\Delta\omega t + (\phi_{a1} - \phi_{b2}) + \varphi(\Delta t) + \omega_b\Delta t) \tag{4.8c}$$

$$i_{x2} = 2A_aA_bH_{b1}H_{a2}\cos(-\Delta\omega t + (\phi_{a2} - \phi_{b1}) + \varphi(\Delta t) + \omega_a\Delta t) \tag{4.8d}$$

Terms in (4.8) represent the interaction between the dual-wavelength source and the sensing network for two generic wavelengths ω_a and ω_b. We can conclude that direct terms, i_d in equations (4.8a) and (4.8b), are present at the frequency $\Delta\omega = \Omega$ and are affected by the phase of a unique sensing device. On the other hand, cross terms i_x occur at the same frequency and are affected by the phase component of different sensors $(\phi_{ak} - \phi_{bk})$. Cross-terms have two additional terms causing a phase delay: $(\varphi(\Delta t))$ is the phase noise inherent to the laser source, and $(\omega_{a,b}\Delta t)$ describes the interferometric phenomenon caused by the cavity formed between two overlapping sub-bands. The effect of these terms on the sensors measurement is addressed in the next section.

The interrogation method to retrieve the phase and amplitude response from the sensors (see figure 4.4) is performed by means of a vectorial network analyzer (VNA), which is used to measure the sensing network scattering parameter S_{21} at a fixed microwave frequency (Ω). In this way, the complete electro-optical frequency response from the system $H(\Omega, \lambda)$ is obtained at the modulation frequency. This is known as a 'zero-span' mode measurement, meaning that the power of the sensing network frequency response is displayed versus time, at the fixed frequency. When we set this frequency to be Ω, the
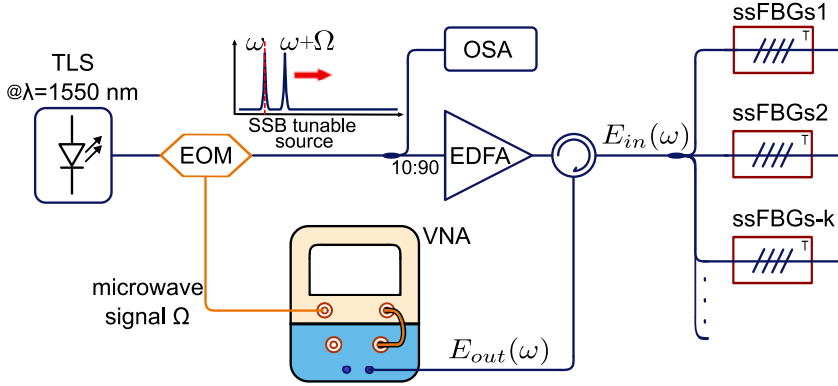
Figure 4.4: Interrogation setup to measure the frequency response of the sensing network. A dual-wavelength scanning source E_{in} is created by the single side band modulation of a tunable laser around 1550 nm. The reflected waves from the sensing array E_{out} are measured at the VNA to compute the sensing network frequency response at the fixed microwave frequency Ω

network frequency response is determined by the *direct* and *cross* terms, which are determined by the phase relationship between adjacent sub-bands of the K sensors present in the network (ϕ_{a_k}, ϕ_{b_k}).

4.3 Experimental Results and Discussion

4.3.1 Wavelength detection
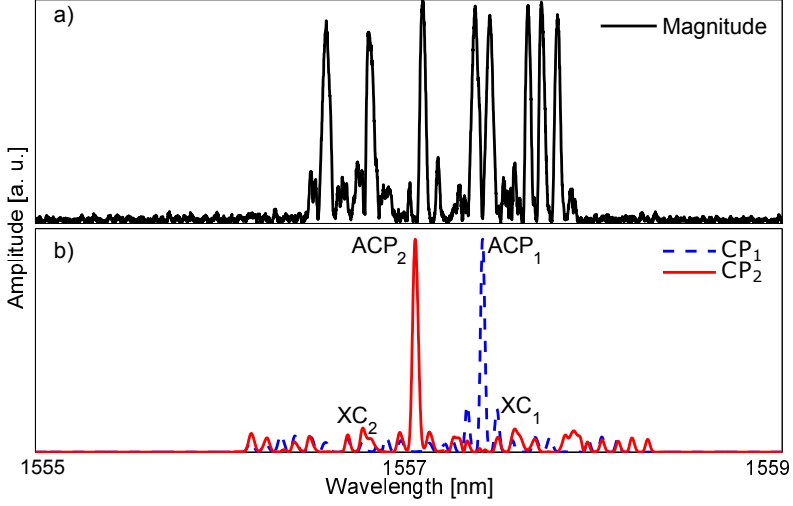
Figure 4.5: a) Shows the total reflected frequency response of the sensing network composed of two encoded FBG sensors. b) represents the correlation product CP_k computed for each sensor. The corresponding ACP value points at the matching wavelength location of each sensor in the spectrum. Cross-correlation values (XC) are obtained for the remaining wavelength points.

After obtaining the complete frequency response from the sensing array, the central wavelength that corresponds to each sensor in the network (λ_{B_k}) must be assessed. We use the correlation product between the sensing network frequency response $H(\Omega, \lambda)$, and the individual expected frequency response of each kth sensor in the network $H_{S_k}(\lambda')$. This can be written as in equation (4.9).

$$CP_k(\lambda') = \int H(\Omega, \lambda) \cdot H_{S_k}^*(\lambda') \, \delta\lambda \qquad (4.9)$$

Where the correlation product CP_k is computed for each sensor over the wavelength operational range λ'. The CP maximum point, known as the auto-correlation peak (ACP), occurs at the wavelength point of maximum co-incidence between the individual sensor and the compounded measurement. Therefore, it indicates the central Bragg wavelength λ_{B_k} for each sensor, see

figure 4.5 for illustration. The residual CP lower values constitute the cross-correlation signal (XC), which is constrained to a low value. This means that the sensor expected response does not match the measured spectrum at those specific wavelength values. In figure 4.5 a), the magnitude component of the retrieved frequency response for a set of two sensors is shown. Figure 4.5 b) shows the corresponding ACP and XC values for the two sensors encoded in the compounded measurement.
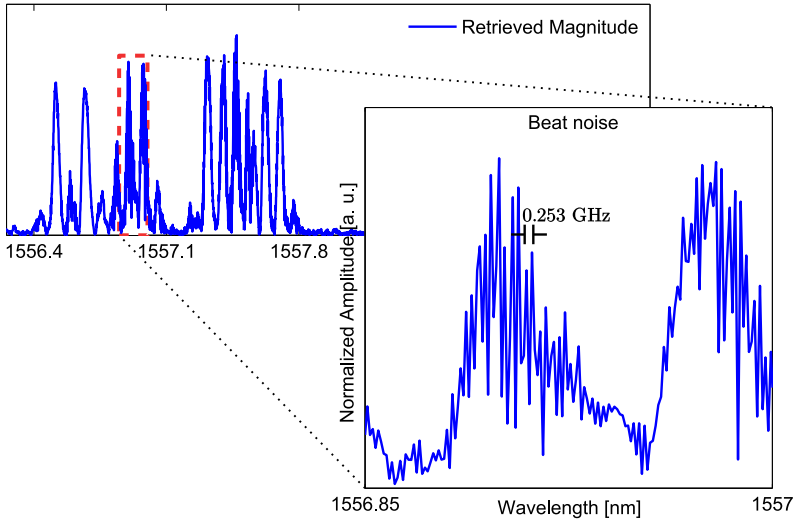
Figure 4.6: Zoomed-in region from a VNA readout. Ripple frequency due to overlapping between two sub-bands is measured to have a frequency of about 0.253 GHz, which is consistent with the placement distance between sensors of approximately 40 cm.

Hence, the correlation product is the ideal mechanism to find the wavelength location of each sensor in the network. Still, it also offers an important advantage because this 'moving product' between each sensor expected shape and the compounded measurement actually bypasses unwanted measured components coming from the *cross* terms (i_x in equations (4.8c), (4.8d)). Cross terms, as described in section 4.2.2, are produced when two sensors overlap and create a temporary cavity between the two reflection sub-bands. The travel time of the cavity is expressed in equations (4.8c) and (4.8d) by the terms $\omega_a\Delta t$ and $\omega_b\Delta t$. The effect of the cavity can be observed in the measurement as a oscillating signal with a ripple frequency that depends on the travel time distance between the two sensors. For instance, figure 4.6, shows a readout from an overlapping scenario between three encoded SSFBG sensors, the difference between 'clean' sub-bands (without ripple effect) and the overlapped sub-bands is noticeable.

The subplot details the ripple effect by zooming into two affected reflection sub-bands. The ripple frequency is determined by measuring the peak to peak distance in the measurement, obtaining a frequency of 0.253 *G*Hz equivalent to a round-trip travel time of 3.952 *n*s (i.e. the two overlapping sensors conform a cavity of approximately 40 *c*m).

4.3.2 SSFBG devices manufacturing and characterization
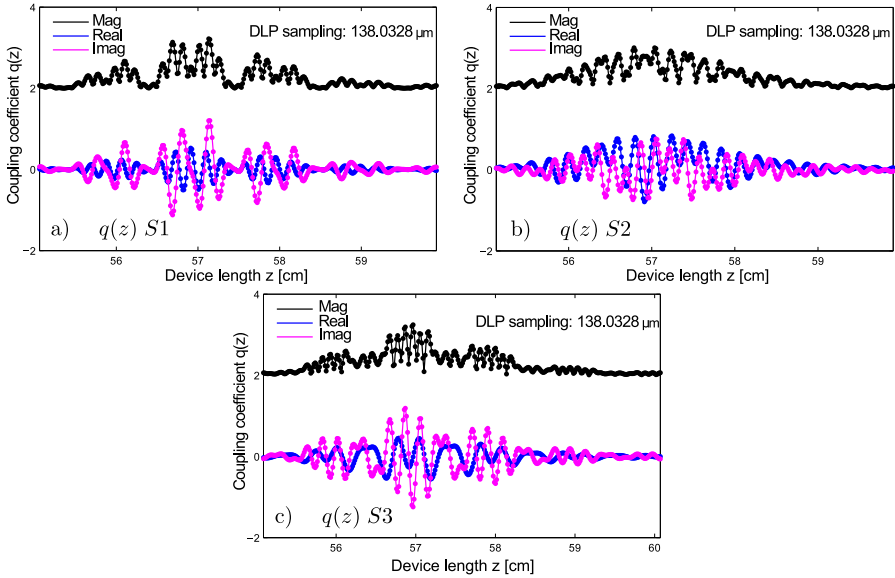
Figure 4.7: Complex coupling coefficient $q(z)$, for the three designed SSFBG sensing devices. The magnitude, real and imaginary components for each sensing device are shown in **a)**, **b)** and **c)**. The amplitude of the coupling coefficient is proportional to the *ac* index profile of the grating.

The manufacturing of the super-structured devices as designed in section 4.2.1 (see the codewords in table 4.2) was performed by using the Discrete Layer Peeling (DLP) synthesis method. The spectral profiles used as target are depicted in Figure 4.3. The design was performed with a linewidth of $FWHM = 40$ *p*m, spacing between sub-bands of $\delta\omega = 10$ *G*Hz and reflectivity set to the 50% in order to use a parallel configuration setup. As the result from the synthesis method we obtain the complex index profile $q(z)$, shown for each sensor in figure 4.7, where the coupling coefficient magnitude, real and imaginary components is depicted for each sensor. For all the devices the index profile is sampled at ~ 138 μm.

Figure 4.8: Design for the super-structured sensor S_1. **a)** depicts the magnitude spectrum in dB for the SSFBG S_1, **b)** shows the linear magnitude spectrum and its bi-evaluated shape. **c)** shows the relative phase of the device. Relative phase of each interrogated sub-band is emphasized with a red circle.
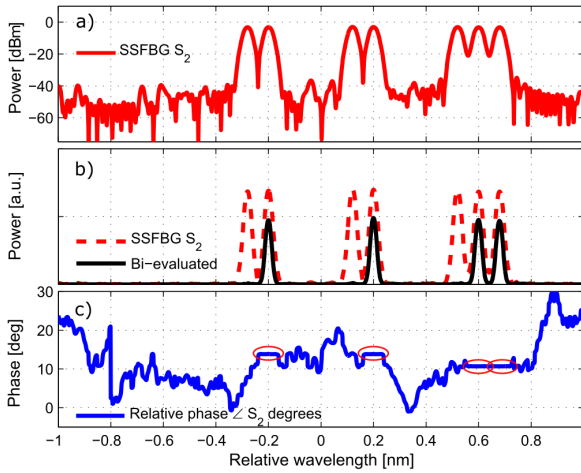
Figure 4.9: Design for the super-structured sensor S_2. **a)** depicts the magnitude spectrum in dB for the SSFBG S_2, **b)** shows the linear magnitude spectrum and its bi-evaluated shape. **c)** shows the relative phase of the device. Relative phase of each interrogated sub-band is emphasized with a red circle.
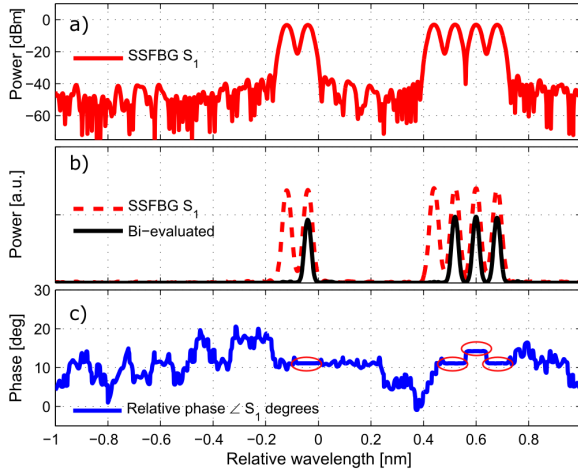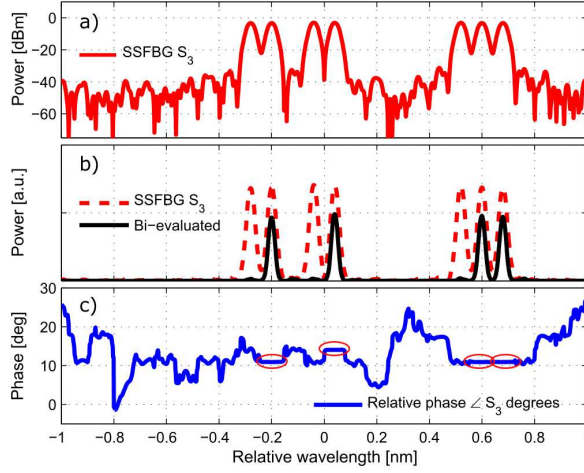
Figure 4.10: Design for the super-structured sensor S_3. **a)** depicts the magnitude spectrum in dB for the SSFBG S_3, **b)** shows the linear magnitude spectrum and its bi-evaluated shape. **c)** shows the relative phase of the device. Relative phase of each interrogated sub-band is emphasized with a red circle.

The manufacturing process is performed point by point through ultra-violet (UV) laser beam exposure using the phase mask (PM) method to produce the compounded Bragg pattern. Hence, the optical fiber was doubly exposed at each sampling point, to a UV beam focused to a diameter of $\sim 80\ \mu$m, with a power of $\sim 48\ m$W. In this way the construction of the grating is controlled by changing the relative alignment between the two consecutive exposures, maintaining the average UV flux and therefore the effective refractive index [13]. The manufacturing system available in the PRL labs is able to construct the fast changes of each custom shape in the $q(z)$ profile, each sampled point in figure 4.7 represents the theoretical location of a double UV exposure. Furthermore, each $q(z)$ profile was truncated at 5% of its amplitude, obtaining a total length for the sensing devices of $S_1 = 4.858\ cm$, $S_2 = 4.775\ cm$ and $S_3 = 4.983\ cm$. Values of $q(z)$ below this threshold have no significant effect in the device manufacturing. The physical length of the SSFBG devices presented here is considerably longer than for conventional FBG sensors. Therefore, they are suited for applications with uniform temperature along the size of the sensors.

The analysis of the complex index profile is presented in Figures 4.8-4.10 for the devices S_1, S_2 and S_3 respectively. For each sensor, it is shown the amplitude of the manufactured device (in dBm and linear representation), their bi-evaluated

amplitude which is the result of dual-wavelength interrogation of the sensors, and their phase component, displaying the relative phase change measured between consecutive sub-bands.

It is important to note, from literals **b)** in figures 4.8 to 4.10, that the 'bi-evaluated' response for each sensor is the expected result after the interrogation of the SSFBG devices with the dual-wavelength source as explained in Fig. 4.3. In the same way, the phase relationship is retrieved between consecutive sensor sub-bands (meaning that the measured phase component is not the actual phase of the component but the relative phase between the two interrogated points). Therefore, the correlation product is performed between the 'bi-evaluated' measured response and the 'bi-evaluated' expected response.
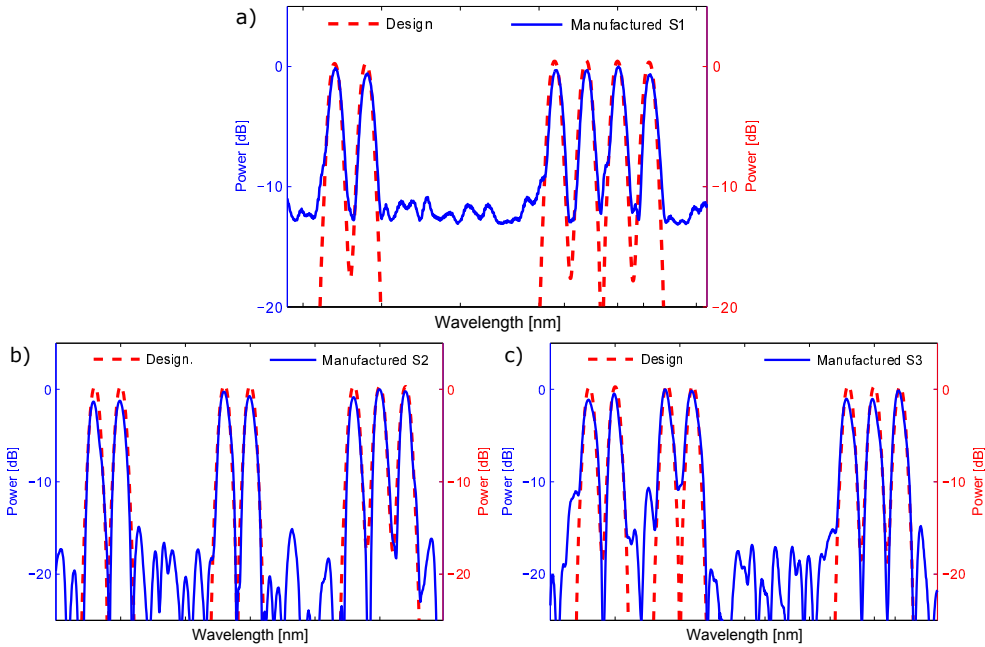
Figure 4.11: The measured Magnitude of the manufactured SSFBG devices is depicted for the devices S_1, S_2 and S_3. The designed magnitude of these sensors is shown for comparison.

Figure 4.11 shows, in magnitude, comparison between the designed and the experimental spectra for the SSFBG devices. In the measurement, performed with an Optical Spectral Analyzer (OSA), the reflectivity value slightly surpasses the 3 dB value due to the manual adjustment of the manufacturing setup. However, the manufactured devices show a very good agreement re-

garding the design. Of course, given the design of the sensors, the amplitude measurement is not enough to assess whether they are well manufactured or not. Therefore, characterization of the devices group delay must be performed and evaluated under the double-wavelength interrogation scheme. Because the design of the devices imposes a change in phase only between adjacent sub-bands, i.e. a relative phase change. Figures 4.12 to 4.14 (literal (a)) show the bi-evaluated expected amplitude response and phase for each one of the sensing devices S_1, S_2 and S_3. The measured amplitude and phase response of the three sensors (S_1, S_2, S_3) is represented in the literal (b) of Figures 4.12 to 4.14. These measurements have been performed using the optical frequency domain reflectometry (OFDR) technique, to do so, a custom OFDR setup available at the photonics research labs. (PRL), Universitat Politècnica de València was used [14], [15], as well as a commercial OFDR equipment (LUNA). The measured amplitude and phase of the devices were bi-evaluated to accurately obtain the expected amplitude and phase shift values.

Figure 4.12: (a) Expected differential amplitude and phase of the device S_1. (b) Full characterization of the manufactured SSFBG device S_1. In solid line, it is reproduced the amplitude response of the sensor $S1$. Dashed line represents the measured phase of the device after differentiation at the sub-bands separation: 10 GHz.
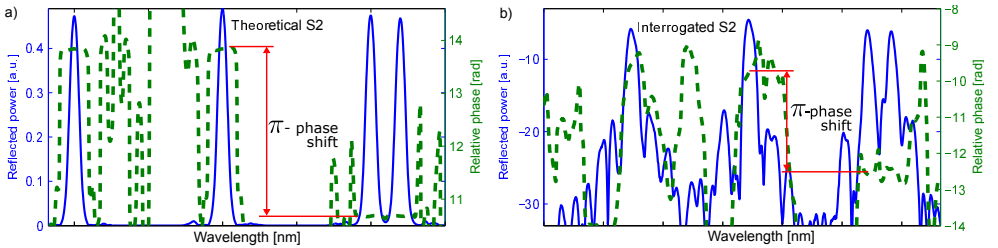
Figure 4.13: (a) Expected differential amplitude and phase of the device S_2. (b) Full characterization of the manufactured SSFBG device S_2. In solid line, it is reproduced the amplitude response of the sensor $S2$. Dashed line represents the measured phase of the device after differentiation at the sub-bands separation: 10 GHz.
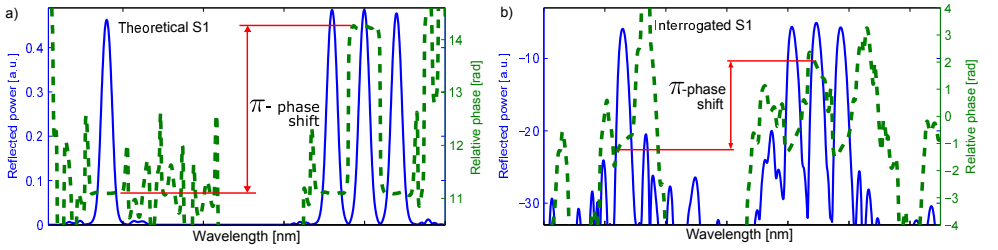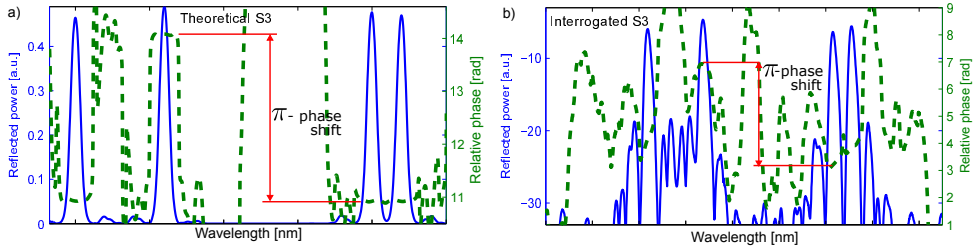
Figure 4.14: (a) Expected differential amplitude and phase of the device S_3. (b) Full characterization of the manufactured SSFBG device S_3. In solid line, it is reproduced the amplitude response of the sensor $S3$. Dashed line represents the measured phase of the device after differentiation at the sub-bands separation: 10 *G*Hz.

4.3.3   Experimental validation

To prove the behavior of the proposed sensors, an experiment with the three overlapping sensors was carried out with the setup proposed in Fig. 4.4. A narrow-linewidth tunable laser source (*Yenista TUNICS T100R*) was swept over the operating range of the sensors at 1 *n*m/s. During sweeping, the laser was SSB modulated at 10 *G*Hz to obtain the dual-wavelength interrogation signal.

The dual-wavelength source triggers the VNA to measure in time the complete network frequency response. Additionally, an Optical Spectrum Analyzer (OSA) is used to monitor the proper modulation of the interrogating signal.

The sensors are stabilized in temperature and strain shifted in order to create the overlapping scenario. At each point of the experiment, the readout from the sensing network is captured at the VNA and stored in a computer to get each sensor central wavelength.

As mentioned in section 4.3.1, the demodulation method, employed to retrieve the central wavelength of each sensing element in the network, consists in the correlation product between the bi-evaluated network frequency response measured in the VNA at 10 *G*Hz, and the expected frequency response for each manufactured sensor. Figures 4.15 **a)** to **d)**. depict four different readouts from the system, and their corresponding correlation product obtained for each one of the three sensors. Figure 4.16 depicts the central wavelength, measured for the three sensors at every step of the complete overlapping scenario. This plot shows that our measurement approach is able to totally identify the spectral position of three sensors that overlap in the same spectral region.
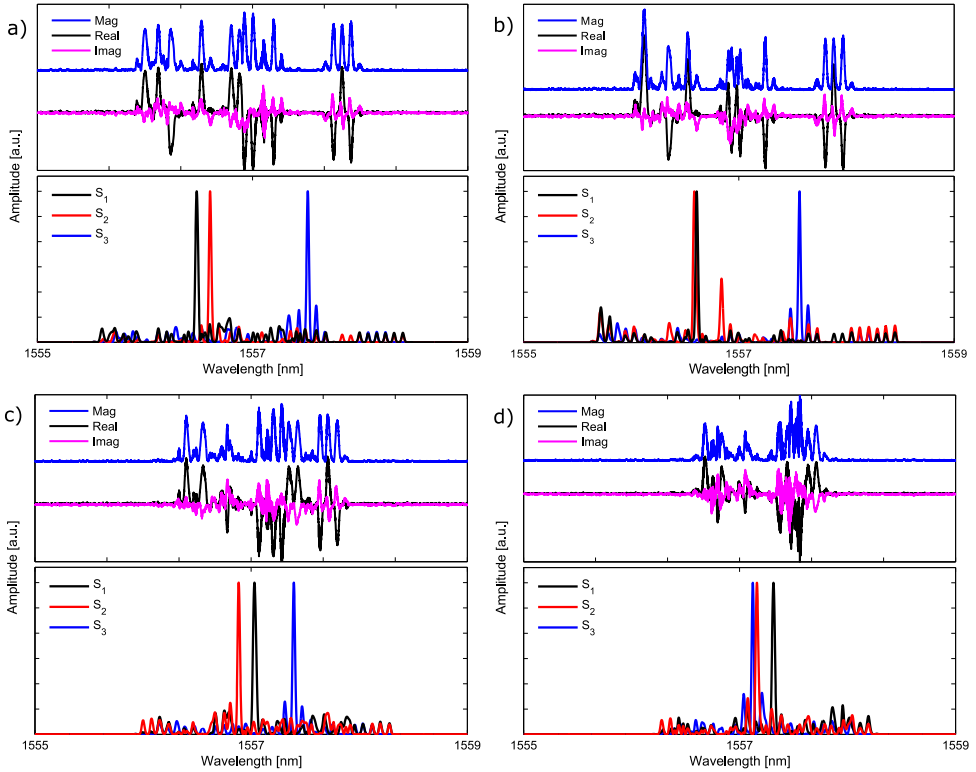
Figure 4.15: There are depicted four instantaneous readout captures from the sensing system, each figure in **a) - d)** shows in the upper plot, the sensing network readout (represented in its magnitude, real and imaginary components) while the lower plot presents the retrieved central wavelength obtained for each sensor after running the correlation algorithm. Magnitude representations have an offset in order to facilitate the visualization

Consequently, we can extrapolate the behavior of the proposed code-division multiplexing scheme to an hybrid CDM-WDM system, in which, for example, three sensors can be placed at each WDM channel. Thus, an enhancement in the number of sensors, proportional to the number of codewords used, 3 in our case, can be achieved.

The last stage of the experimental validation consists of the assessment of the error induced to the system when we add a number of sensors that actually share the same spectral range. In order to characterize the amount of induced error, we need to remove the effect of the additional sensors interfering within the readout. Consequently, we performed an experiment that recreates the
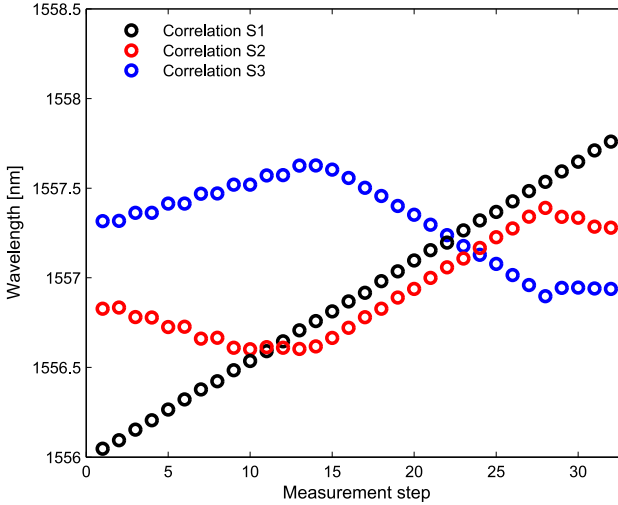
Figure 4.16: The detected central wavelength of each sensor is depicted for the whole overlapping experiment between the three sensors. Successful detection of the three sensors is achieved through the correlation procedure.

overlapping scenario, so that we could measure both, the individual contribution from each sensor and the compounded readout when two or three sensors are interacting with each other. In this way, we also neglect the human error from the measurements since we are taking the individual and compounded contributions at the same instant along the same experiment.

The individual wavelength was measured for the sensing device S_3, this measured wavelength was then contrasted against its measured wavelength in presence of sensor S_1 and finally against its wavelength when sensors S_1 and S_2 where sharing the spectral region. The point by point difference between the individual measured wavelength and the wavelength obtained in presence of an additional sensor is depicted in Figure. 4.17 a). Fig. 4.17 b) shows the point by point difference when two additional sensors are interacting with the individual sensor. The standard deviation due to the cross-correlation between two sensors is $\sigma_{xc2} = 2.68$ *p*m, and due to the interaction between three sensors: $\sigma_{xc3} = 3.92$ *p*m.
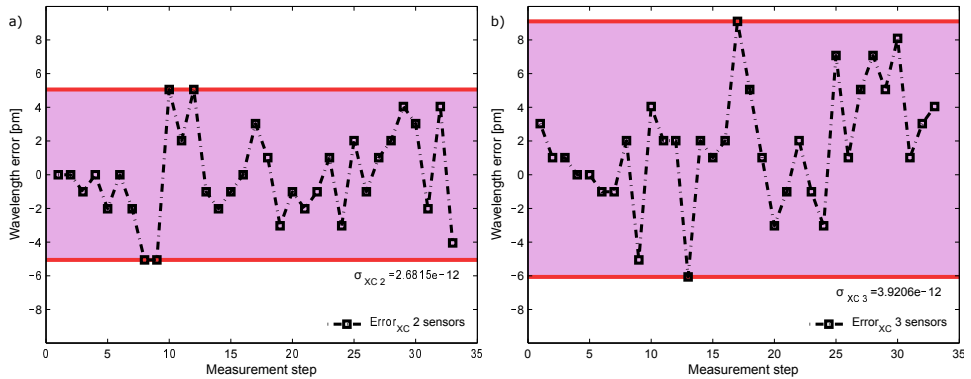
Figure 4.17: Error found for the isolated sensor after comparison with the detected wavelength in presence of a second sensor (a), and after comparison with two additional sensors interacting in the same spectral range (b).

4.4 Conclusions

In this chapter a novel multiplexing technique for fiber Bragg grating (FBG) sensors based on the use of optical code division multiplexing (OCDM) concepts has been studied and analyzed. This sensors design methodology adds a multiplexing dimension to the traditional wavelength division multiplexing (WDM) approach and therefore, allows the enhancement of the number of sensors deployed in the sensing network. Particularly, it has been proposed the encoding, in phase and amplitude, of super-structured FBG devices in such a way that more than two sensors can share their operational range in the spectrum. This is possible because with the encoding of the sensors, each sensor in the network is endowed with additional information (not only a wavelength peak) so that they can be identified even under overlapping conditions.

To achieve the wavelength identification of the designed sensing structures, the design of the sensors amplitude and phase profiles has been complemented with the design of a specialized interrogation technique. This interrogation technique uses a dual wavelength source and a vectorial network analyzer to retrieve the differential profile from each sensing device in the network. This technique and its interaction with the sensors was theoretically developed in order to better understand the measured terms from the network frequency response.

After successful manufacturing of the SSFBG devices via the phase-mask technique, experimental validation under spectral overlapping scenarios was achieved. Results showed that the system is capable of identifying each sensor wavelength even when three sensors are merging into each other spectrally. We also addressed the error added to the network due to the overlapping between the three devices. This additional error has a very low impact in the measurement. The worst case in standard deviation was of 3.9 pm when three sensors are sharing the same spectral region.

References

[1]   R. Dixon, *Spread Spectrum Systems with Commercial Applications*. Wiley, 1994, ISBN: 9780471593423 (cit. on p. 74).

[2]   A. Lam, S. Tantaratana, and R. Zaputowycz, *Theory and Applications of Spread-spectrum Systems: A Self-study Course*. IEEE, 1994, ISBN: 9780780303744 (cit. on p. 74).

[3]   W. Amaya, D. Pastor, R. Baños, and V. Garcia-Munoz, "Wdm-coherent ocdma over one single device based on short chip super structured fiber bragg gratings", *Opt. Express*, vol. 19, no. 24, pp. 24 627–24 637, Nov. 2011. DOI: `10.1364/OE.19.024627` (cit. on p. 74).

[4]   E. H. Dinan and B. Jabbari, "Spreading codes for direct sequence cdma and wideband cdma cellular networks", *IEEE Communications Magazine*, vol. 36, no. 9, pp. 48–54, Sep. 1998, ISSN: 0163-6804 (cit. on p. 74).

[5]   X. Wang, N. Wada, T. Hamanaka, T. Miyazaki, G. Cincotti, and K. Kitayama, "Ocdma over wdm transmission", in *2007 9th International Conference on Transparent Optical Networks*, vol. 1, Jul. 2007, pp. 110–113. DOI: `10.1109/ICTON.2007.4296043` (cit. on p. 74).

[6]   C. C. Yang, J. F. Huang, and I. M. Chiu, "Performance analyses on hybrid mqc/m-sequence coding over frequency/spatial optical cdma system", *IEEE Transactions on Communications*, vol. 55, no. 1, pp. 40–43, Jan. 2007, ISSN: 0090-6778. DOI: `10.1109/TCOMM.2006.887793` (cit. on p. 75).

[7]   R. Baños, D. Pastor, W. Amaya, and V. Garcia-Munoz, "Chromatic dispersion compensation and coherent direct-sequence ocdma operation on a single super structured fbg", *Opt. Express*, vol. 20, no. 13, pp. 13 966–13 976, Jun. 2012. DOI: `10.1364/OE.20.013966` (cit. on p. 75).

[8]   A. M. R. Pinto, O. Frazao, J. L. Santos, M. Lopez-Amo, J. Kobelke, and K. Schuster, "Interrogation of a suspended-core fabry-perot temperature sensor through a dual wavelength raman fiber laser", *Journal of Lightwave Technology*, vol. 28, no. 21, pp. 3149–3155, Nov. 2010, ISSN: 0733-8724. DOI: `10.1109/JLT.2010.2078490` (cit. on p. 77).

[9]   H. Jiang, J. Chen, T. Liu, and W. Huang, "A novel wavelength detection technique of overlapping spectra in the serial wdm fbg sensor network", *Sensors and Actuators A: Physical*, vol. 198, no. 1, pp. 31–34, 2013, ISSN: 0924-4247. DOI: `http://dx.doi.org/10.1016/j.sna.2013.04.023` (cit. on p. 78).

[10]   H. Jiang, J. Chen, and T. Liu, "Wavelength Detection in Spectrally Overlapped FBG Sensor Network Using Extreme Learning Machine", *Photonics Technology Letters, IEEE*, vol. 26, no. 20, pp. 2031–2034, Oct. 2014, ISSN: 1041-1135. DOI: `10.1109/LPT.2014.2345062` (cit. on p. 78).

[11]   D. Liu, K. Tang, Z. Yang, and D. Liu, "A Fiber Bragg Grating Sensor Network Using an Improved Differential Evolution Algorithm", *Photonics Technology Letters, IEEE*, vol. 23, no. 19, pp. 1385–1387, Oct. 2011, ISSN: 1041-1135. DOI: `10.1109/LPT.2011.2160992` (cit. on p. 78).

[12]   J. Chen, H. Jiang, T. Liu, and X. Fu, "Wavelength detection in FBG sensor networks using least squares support vector regression", *Journal of Optics*, vol. 16, no. 4, 2014 (cit. on p. 78).

[13]   R. Baños, V. Garcia-Munoz, D. Pastor, and W. Amaya, "Rectangular Global Envelope Super Structured FBGs for Multiband Coherent OCDMA", *Photonics Technology Letters, IEEE*, vol. 25, no. 5, pp. 512–514, Mar. 2013, ISSN: 1041-1135. DOI: `10.1109/LPT.2013.2242880` (cit. on p. 89).

[14]   L. Bru, B. Gargallo, G. Mico, R. Banos, J. Domenech, A. M. Sanchez, R. Mas, E. Pardo, D. Pastor, and P. Munoz, "Optical frequency domain reflectometry applied to photonic integrated circuits", in *Proc. European Conference on Integrated Optics*, 2016 (cit. on p. 91).

[15]   L. A. Bru, Z. Ye, D. Pastor, and P. Munoz, "Multi-parameter estimation of high-q silicon rich nitride resonators using optical frequency domain reflectometry", vol. 10535, 2018, pp. 10535 - 10535 - 8 (cit. on p. 91).

Chapter 5

Interrogation of complex sensing devices: Discrete Prolate Spheroidal Sequences

5.1 Introduction

In Chapter 4, phase and amplitude encoded sensors were designed and experimentally validated. Their mutually orthogonal behavior was proven to allow the total wavelength detection of the encoded sensors under overlapping scenarios.

The detection of such sensing devices required the proposition of a custom interrogation method: the dual-wavelength interrogation approach, which is able to characterize the working range of the sensors in a scanning fashion. In this Chapter, we use the dual-wavelength interrogation method to identify the wavelength of a different sensing structure, not specifically designed as a sensing device. The Discrete Prolate Spheroidal Sequences (DPSS) have been proposed as complex devices with very specific complex (amplitude and phase) patterns. Besides, DPSS have an interresting property that fits perfectly with

the desired features of encoded SSFBG sensors: All the elements in a DPSS family are bandwidth constrained. Meaning that a family of mutually orthogonal sensors can be extended in number without compromising the bandwidth of the devices.

DPSS have been proposed in the 70s [1] as an interesting set of orthogonal codewords. Recently, DPSS have been proposed [2] and experimentally validated [3] as en/decoding structures useful in OCDMA communications systems. Showing a high encryption potential and very suitable features for channeling in WDM systems due to their fixed optical bandwidth.

In this chapter, we propose and validate the use of DPSS-like structures as sensing devices. SSFBG devices are designed and manufactured after the shape of DPS sequences, which essentially are periodical series with amplitude and phase terms. Therefore, the interrogation method proposed in Chapter 4 can be used to retrieve the complex response of each DPSS device in the network. Thus, custom-manufactured DPSS-SSFBG devices are used as sensing elements in an encoded FBG-based sensing network.

This chapter is organized as follows. The principles of DPS sequences are introduced in Section 5.2 as well as the manufacturing considerations. The demodulation process is outlined in Section 5.2.1. Section 5.3 presents and analyzes the experimental validation of a sensing scenario with two DPSS-SSFBG sensors. Finally, some conclusions are drawn in Section 5.4.

5.2 DPSS structures: Principle and manufacturing

DPS sequences feature mutual orthogonality between the members of a family, this feature is very important from the point of view of OCDMA communications systems since large codewords families can be used to encode and decode the information transmitted between multiple users. Another interesting characteristic of the DPS sequences is their bandwidth limited nature, meaning that each member of the DPSS family is constrained to a delimited range of frequencies. This specific characteristic makes DPSS devices of great applicability as sensors given that a number of orthogonal devices can be designed guaranteeing that the spectral bandwidth will remain the same for all the devices. The creation of a set of DPSS codes [1] requires the definition of a symmetric tridiagonal matrix, whose eigen-vectors: $T(N, W)$ constitute the codewords family with length (N) and a discrete frequency covering range (W). The entries of the tridiagonal matrix are given by equation (5.1).
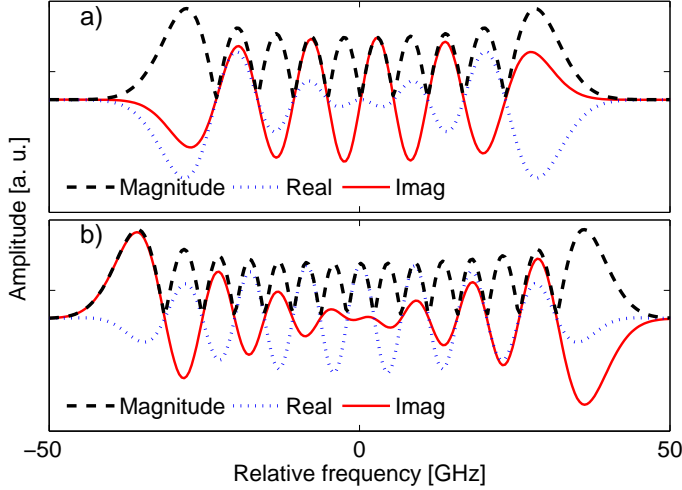
Figure 5.1: Theoretical frequency response of the DPS sequences; real part: blue (dotted line), imaginary part: red (continuous line), magnitude: black (dashed line). **a):** DPS Sequence with $k = 10$. **b):** DPS Sequence with $k = 15$.

$$T(i,j) = \begin{cases} \frac{1}{2}i(N-1), & j = i-1 \\ (\frac{N-1}{2} - i)^2 \cos(2\pi W), & j = i \\ \frac{1}{2}(i+1)(N-1-i), & j = i+1 \\ 0, & otherwise; \end{cases}$$

$$i, j = 0, 1, \ldots, N-1 \quad (5.1)$$

Using equation (5.1), with $N = 128$ and $W = 0.5$, we obtain a set of 128 codewords with a codeword length of 128 as well, band-limited to $[-W, W]$ (i.e. the energy of the sequence is finite and restricted to a certain bandwidth value W). In Figure 5.1 it is represented the spectral response of two codewords of the obtained family, hence the amplitude, imaginary and real components of the codewords number $k = 10$ and $k = 15$ are represented. The number of the sequence in the set, from $k = 1$ to N, corresponds with the concentration degree of the energy in the spectral and temporary domains and with the number of alternating lobes of the structure. Figure 5.1 also exemplifies the difference between even an odd DPS sequences.
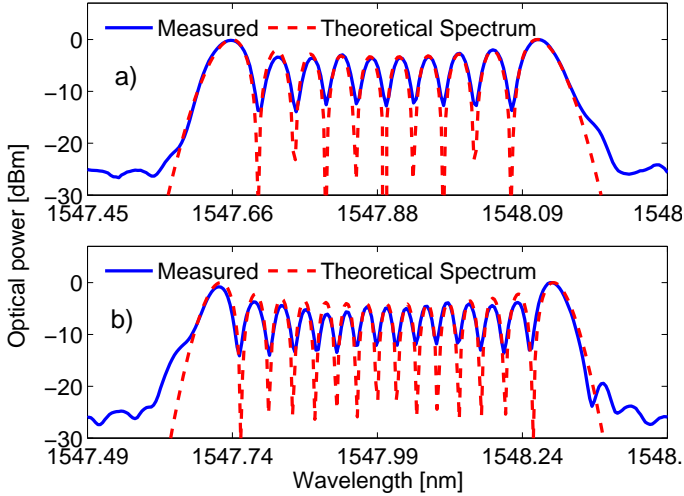
Figure 5.2: Measured spectrum for FBG-manufactured DPS sequences with **a):** $k = 10$ and **b):** $k = 15$. Manufactured spectrum, plotted in blue (continuous line), is compared with the theoretical expected spectrum in red (dashed line).

The manufacturing of the super-structured FBG devices with the shape of DPS sequences was carried out using the Discrete Layer Peeling (DLP) synthesis method in the same way as in the past approaches. The target is the theoretical response of the codewords number 10 and 15 as depicted in Figure 5.1, the bandwidth of the devices is constrained to 100 GHz ~ 0.8 nm; and the theoretical profile is sampled each ~ 85.6 μm to obtain the complex index profile $q(z)$. Manufacturing of these profiles in the optical fiber was performed through the continuous phase-mask method described in Chapter 2, magnitude and phase control of each sample of $q(z)$ was achieved by double UV exposure of 200 ms (with UV beam power of 50 mW), maintaining the average UV flux constant [4], [5]. Characterization of the manufactured devices was performed by measuring the spectral power with an optical spectrum analyzer (OSA) at 10 pm resolution. Figure 5.2 compares the manufactured and the theoretical spectra, showing very good results for the actual device regarding the design.
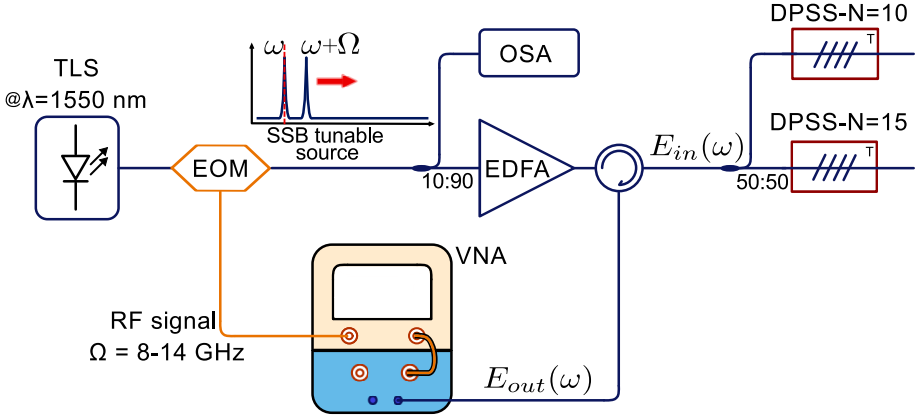
Figure 5.3: A parallel-schematic sensing setup is implemented to measure the central wavelength for each one of the DPSS-FBG sensors. A tunable dual-band source $E_{in}(\omega)$ is swept over the working spectrum; the reflected signals $E_{out}(\omega)$ are retrieved at the VNA to determine their frequency response at a fixed Ω. TLS, tunable laser source; SSB, single side band modulation; EOM, electro-optic modulator; OSA, optical spectrum analyzer; EDFA, erbium-doped fiber amplifier; DPSS, discrete prolate spheroidal sequence sensor; VNA, Vectorial Network Analyzer.

5.2.1   Demodulation

The main difference between DPSS and the custom designed sensors presented in Chapter 4 relies in the fact that the spacing between sub-bands in the custom designed SSFBG sensors was adjusted according to the distance between the two interrogating wavelengths, thus a differential demodulation of the sensors was performed. DPSS structures, on the other hand, does not have a specific separation between sub-bands (each codeword has a slightly different separation depending on its energy concentration). Nevertheless, the complex spectral response of DPSS codewords (amplitude and phase) is also needed to perform the identification of each device in the spectrum. So the dual-wavelength detection method is used but the separation frequency between the two wavelengths will not be determined by the design of the sensors. Still, due to the oscillating behavior of the sequences, the bi-evaluated response proved to maintain a good level of orthogonality between most part of the family members in the initial simulations.

A dual-wavelength tunable source is used to illuminate the sensing devices as depicted in the schematic of Figure 5.3, in this setup, the source is obtained through the SSB modulation of a tunable laser at 1550 nm. Also, a vectorial

network analyzer (VNA) is used to measure the frequency response of the network as a function of the source sweeping time. The measurement is carried out only at the specific modulation frequency of the source, i.e. 'zero-span' measurement, so that the electro-optical frequency response of the complete system $H(\Omega, \lambda)$ for a fixed microwave angular frequency Ω is obtained (i.e. the VNA measures the scattering parameter S_{21} of the sensing network).

In the interrogation setup presented in Figure 5.3, the dual wavelength source $E_{in}(\omega)$ can be modeled as in equation (5.2):

$$E_{in}(\omega) = a_1 \delta(\omega) + a_2 \delta(\omega + \Omega) \tag{5.2}$$

Where ω is the optical angular frequency, a_1, a_2 are the arbitrary amplitude constants of each wavelength and δ, which denotes the Dirac's delta function, represents the ideal wavelength form. Also in Figure 5.3, it is expressed the electrical field coming $E_{out}(\omega)$ arriving at the VNA after being reflected from the sensing network. This can be written as in equation (5.3):

$$E_{out}(\omega) = a_1 H_{net}^{O}(\omega)\delta(\omega) + a_2 H_{net}^{O}(\omega + \Omega)\delta(\omega + \Omega) \tag{5.3}$$

Where, H_{net}^{O} stands for the optical complex spectral response of the whole network. Then, the detected photo-current, in time domain, is given by equation (5.4):

$$i(t) \propto |H_{net}^{O}(\omega)||H_{net}^{O}(\omega + \Omega)|$$
$$\cos\left(\Omega t + \left[\angle H_{net}^{O}(\omega) - \angle H_{net}^{O}(\omega + \Omega)\right]\right) \tag{5.4}$$

As mentioned previously, the networks frequency response acquisition is performed under the 'zero span' configuration, meaning that the network response is only measured at the modulation frequency Ω. The remaining components are filtered out therefore the formulation given in equations (5.3), (5.4) does not include baseband terms at $\omega = 0$. In this way, a comparison could be made between the acquired network frequency response and the modulating signal used to generate the dual-wavelength interrogating source. The final result of this process is the complete electro-optical frequency response of the network (at the fixed RF value of Ω), written as in equation (5.5).

$$|H(\Omega, \omega)| \propto |H_{net}^{O}(\omega)||H_{net}^{O}(\omega + \Omega)|$$
$$\angle H(\Omega, \omega) = \angle H_{net}^{O}(\omega) - \angle H_{net}^{O}(\omega + \Omega) \tag{5.5}$$
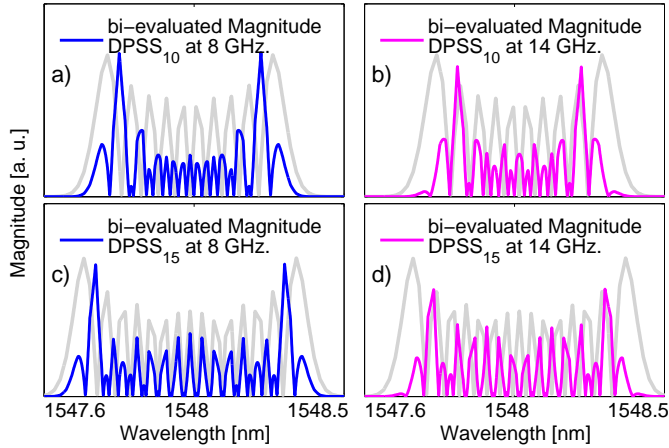
Figure 5.4: *Bi-evaluated* frequency response for the DPSS-FBG sensors studied in this work. These are the signals employed in the cross-correlation product to obtain DPSS-FBG sensors' central wavelength. **a), c):** Magnitude of the *bi-evaluated* frequency response at $\Omega = 8$ *G*Hz. for codewords 10 and 15 respectively **b), d):** Magnitude of the *bi-evaluated* frequency response at $\Omega = 14$ *G*Hz. for codewords 10 and 15 respectively (Watermark shows the magnitude of the actual DPSS-FBG sensors for clarity).

A critical aspect regarding the sensor detection with the dual-wavelength interrogation scheme has to do precisely with the separation of this two wavelengths. As explained above, the two wavelengths are necessary to find the complex network frequency response at the fixed frequency value (Ω). But, as opposed to the last encoding approach (Chapter 4), in this case the sub-bands separation is not designed to match the dual wavelength separation. Therefore, the interrogated shape will not be differential and will depend differently on each interrogated structure. Consequently, the correlation product used to identify the central wavelength should be performed having into account the *'bi-evaluated shape'* of each sensor in the spectrum. Each DPSS device will generate a different bi-evaluated spectral form and these shapes will also vary when different modulation frequencies are used. This is due to the fact that the correlation product is the moving product (convolution) between the dual-wavelength source and each DPSS shape.

Figure 5.4 exemplifies the magnitude of the *bi-evaluated* theoretical response for the DPSS-FBG sensors employed in the experimental demonstration (DPSS$_{10}$ and DPSS$_{15}$). For these structures the bi-evaluated product results in a specific shape that depends also on the wavelength separation of the source. In

Figure 5.4 a) and c), it is shown the *bi-evaluated* expected response when the source has a wavelength separation of $\Omega = 8$ *GHz*, on the other hand, Figure 5.4 b) and d) depict the *bi-evaluated* response of the same sensing devices when they are interrogated by a source with wavelength separation of $\Omega = 14$ *G*Hz. The differences between the *bi-evaluated* responses and the actual spectral shape of the DPSS-FBG sensors (represented as a watermark in Fig. 5.4) are noticeable.

In order to obtain the central wavelength of each sensor (λ_{B_k}), the correlation product CP_k (for each kth sensor) should be performed between the total frequency response measured from the sensing network and the *bi-evaluated* frequency response for each sensing device at the proper frequency (equation (5.6)).

$$CP_k(\omega') = \int H(\Omega, \omega) \cdot H_{biS_k}(\omega') \, d\omega \qquad (5.6)$$

Where the correlation product CP_k is the moving product relating the total frequency response of the network ($H(\Omega, \omega)$) and the *bi-evaluated* spectral shape of each sensor ($H_{biS_k}(\omega')$) The result of performing the correlation product of equation (5.6) is a correlation signal which is composed by the Auto-correlation peak (ACP) and the residual cross-correlation (XC) signal. The ACP points at the spectral position of the sensor (λ_{B_k}), it is produced at the point where the theoretical shape of the kth sensor coincides with the complex shape of the total measured frequency response. The XC values, on the contrary, are caused by all the positions in the spectrum where no coincidence is found.

The demodulation process, besides being the mechanism to identify the sensors position, can be seen as a post-processing stage. In this context, it is possible to perform additional tasks during the demodulation stage. For example, a common event that takes place during the overlapping process between two sensors is the beat noise. Beat noise is an issue in CDMA communication systems caused by two reflectors operating at the same wavelength range, when two reflective devices operate at the same frequency, they conform a cavity and therefore a ripple is added at the specific wavelength. The ripple frequency is determined by the physical distance between the two devices (see Section 4.3.1). In our case, two sensors (reflective devices based on FBGs) can interact in the spectrum, conforming therefore a cavity at the overlapping wavelength. However, the correlation product performed to identify the central position of the sensors neglects the ripple effect because it acts as a moving filter with the exact shape of the interrogated sensors.

As mentioned above, the shape of the detected complex spectrum from the sensors depends not only on the manufactured devices but also on the tunable source used to interrogate them. The dual-wavelength source is obtained as a single side band modulation of a tunable laser in the C-band ($\sim 1550nm$). Hence, using an external Electro-Optical modulator (EOM), the separation between the two wavelengths can reach 20 GHz. In order to elucidate how this variation affects the identification of the proposed sensors a simulation was performed, in which the ratio between the Auto- and the cross-correlation signals was analyzed as a function of the modulation frequency (swept from 0 to 20 GHz). Two cases are depicted: first, the worst case scenario, where the two sensors are located at the same spectral position as well as a scenario where the two sensors are starting to merge. Figure 5.5 a) depicts the simulation results for the former scenario (total overlapping of the two sensors), in this case the ratio XC/ACP is depicted for the two sensors $DPSS_{S1}$, $DPSS_{S2}$ against the modulation frequency Ω used to establish the separation between the two interrogating wavelengths. The results show a better XC/ACP ratio for the first sensor $DPSS_{S1}$ almost at all frequencies while the lower ratio reached by the second sensor $DPSS_{S2}$ is located around 8 and 12 GHz. It can be noticed also that for these frequency values, the XC/ACP ratio reach similar values for both sensing devices. Figure 5.5 b) shows the same analysis at a partial wavelength overlapping scenario for the two sensors; results show, as expected, a better behavior in the two cases. Again, similar relationships are obtained for the two sensors around the highlighted frequencies in the graph (8 and 14 GHz). From this figure it can be inferred, that the interrogation of this pair of sensors can be performed at 8 or 14 GHz, obtaining very similar results: a XC/ACP ratio around 44% to 60% at the worst case scenario, and values between 26% or 37% under partial overlapping of the two sensors. We can then conclude that identification of the central wavelength is feasible under overlapping conditions.
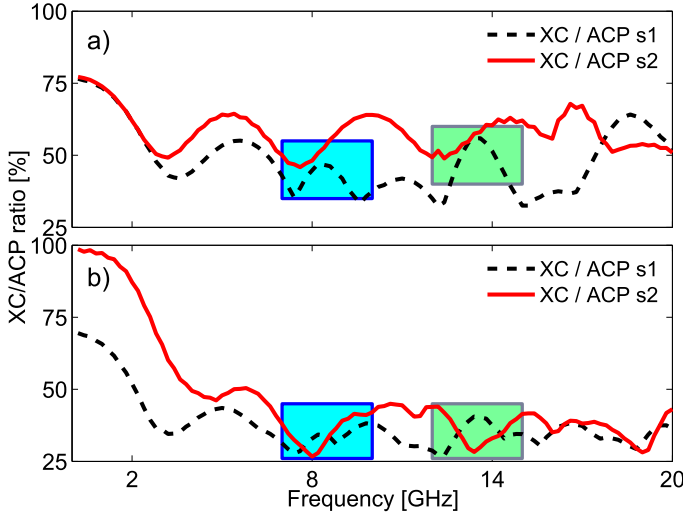
Figure 5.5: XC/ACP ratio calculated for sensors $S1$ and $S2$ at different values of the modulation microwave frequency Ω. Highlighted regions show the selected Ω values utilized in the experimental validation. a) shows the XC/ACP ratio for both sensors at the *worst-case-scenario:* identification of two sensors at the same spectral location. b) shows the calculated XC/ACP ratio for the two sensors when their spectral positions are barely overlapping.

5.3 Experimental validation

Validation of the manufactured sensors was performed in a proof of the concept setup between the two sensors $DPSS_{S1}$ and $DPSS_{S2}$. The setup is depicted in Figure 5.3, where a tunable laser source in the C-band is modulated in SSB configuration to obtain a dual-wavelength scanning source. The modulation frequency is set at 8 and 14 GHz to establish the wavelength separation of the dual-wavelength source. The dual-wavelength TLS is amplified and scanned at 1 nm/s over the operational spectrum of the sensors. This field $(E_{in}(\omega))$ is sent to the sensing devices, from which it is generated the reflected signal that goes to the vectorial network analyzer (VNA). The reflected signal, $E_{out}(\omega)$ is then acquired in what is known as a zero-span measurement. Hence, the reflected frequency response from the sensing devices (in both, amplitude and phase terms) is acquired as a function of the sweeping time in the dual-wavelength source. Two passive splitters are used in the setup, the first one is a 10:90 splitter to monitor the dual-wavelength signal at the OSA and the second one is a 50:50 splitter used to establish parallel configuration between two DPSS-FBG sensors. The two $DPSS$ sensors are arranged inside temperature chambers in
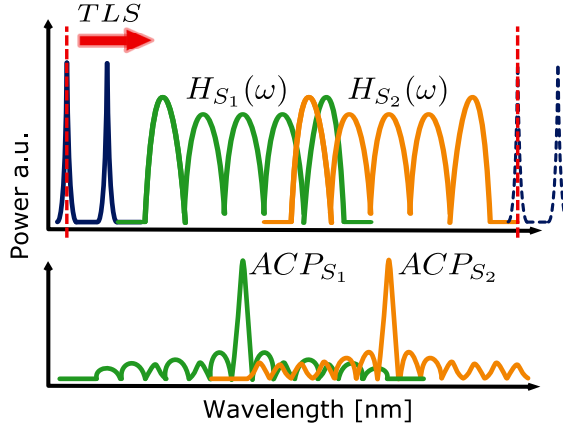
Figure 5.6: The cross-correlation product is computed to obtain the central wavelength ACP of each sensor in the network. $H_{S_k}(\omega)$ is the frequency response for the kth sensor in the network.

order to shift their central wavelength. To prove their behavior under overlapping conditions, the first sensor is maintained at a fixed temperature while the second one is shifted in wavelength.

Figure 5.6 describes theoretically the interrogation method based on the dual-wavelength sweeping over the sensors operational spectrum. Basically, the dual-wavelength source scans the total spectrum and it gets reflected according to the complex form of the arranged sensors. The reflected signal is measured at the VNA only at the specific modulation frequency Ω (this is the frequency that imposes the wavelength separation of the dual-wavelength source).

As mentioned in section 5.2.1, due to the specific design of the DPSS structures there is no a single optimal frequency to interrogate the sensing devices. Through simulation, we have found that the behavior between the ACP and the XC signals is enhanced at certain modulation frequencies, meaning that the wavelength spacing of the dual-wavelength source can be fixed at those frequencies that boost the detection results. In the next subsections we present the experimental results obtained when performing the detection of the sensors at two specific modulation frequencies: 8 and 14 GHz.
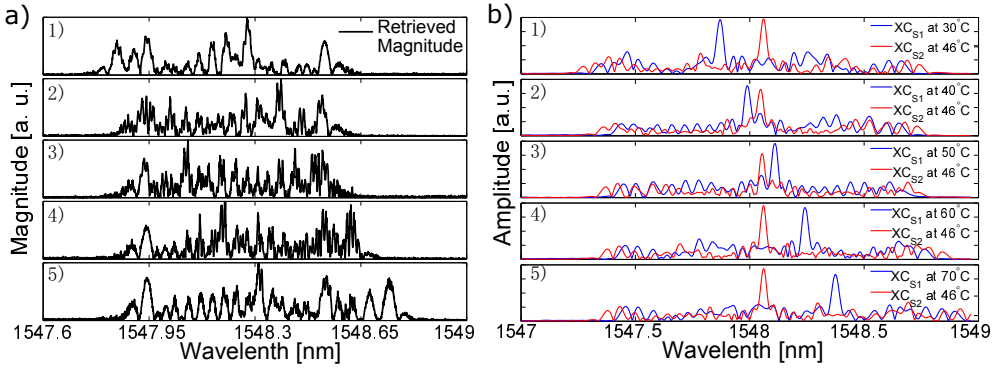
Figure 5.7: (a) Experimental measurement of the frequency response of a sensing network composed of two DPSS-FBG sensors at 8 *G*Hz. Numerals 1) to 5) show different captures of the system as one of the sensors is wavelength shifted while the second one is maintained at a fixed wavelength. (b) The correlation product is computed for the frequency response of the sensing network taken at 8 *G*Hz. The obtained ACP determines the central wavelength for each sensor deployed in the network.

5.3.1   *Frequency modulation at* 8 *GHz*

Figure 5.7 a) depicts the measured frequency response (in magnitude) measured at 8 *G*Hz in the VNA. Figure 5.7 a), numerals 1) to 5) represent different readouts in the process of overlapping between the two sensors. These measurements were taken and then processed through the correlation algorithm in order to obtain the central wavelength location for each one of the overlapping sensors. Although the readout is shown in magnitude, the correlation is the complex product between theoretical and measured spectrum, i.e. the correlation process includes also the phase terms.

In Figure 5.7 b) it is depicted the obtained correlation product for each one of the readouts presented in Figure 5.7 a), as expected, the ACPs point at the central wavelength location of each sensor while one of the sensors is swept and the second one remains at a fixed wavelength Figure 5.7 a) 1) - 5).
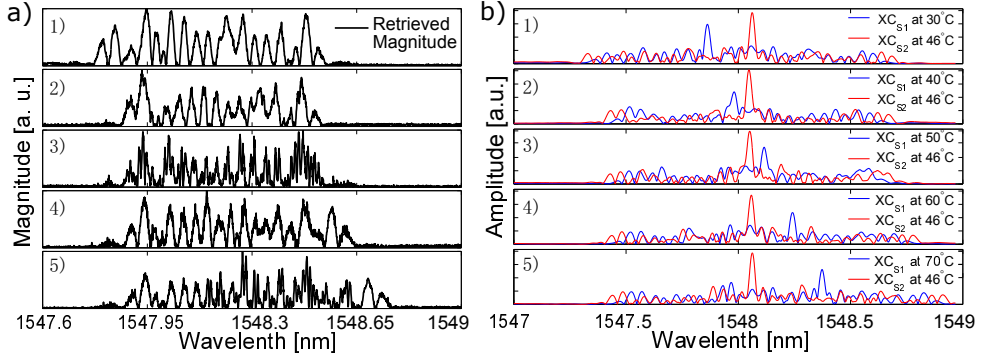
Figure 5.8: (a) Experimental measurement of the frequency response of a sensing network composed of two DPSS-FBG sensors at 14 *G*Hz. Numerals 1) to 5) show different captures of the system as one of the sensors is wavelength shifted while the second one is maintained at a fixed wavelength. (b) The correlation product is computed for the captured 14 *G*Hz. frequency response of the sensing network. The obtained ACP determines the central wavelength for each sensor deployed in the network.

5.3.2   Frequency modulation at 14 GHz

The detection experiment was also performed with a different separation value in the dual-wavelength interrogating signal. Having into account the simulation results presented previously, the modulation frequency was set to 14 *G*Hz. Introducing a change in the dual-wavelength interrogating signal produces a totally different retrieved signal, Figure 5.8 a) 1)-5) show the retrieved magnitude of the frequency response at different stages of the overlapping process. The same principle was employed in the experiment, one of the sensors is swept over the spectral position of the second sensor. Figure 5.8 b) numerals 1) - 5) depict the resultant cross-correlation signals. Total detection of both sensors is successful with this configuration.

5.3.3   Discussion

When comparing the experimental demodulation results obtained for different modulation frequencies (see Figures 5.7 and 5.8), it is clear that the ratio XC/ACP has a dependence due to the change in the distance between the two wavelengths. Although the two sensors are identified with a good ratio between the ACP and the XC, the results show a slightly better performance when generating the dual-wavelength signal by using a modulating signal at 8 *G*Hz. This experimental result agrees with the simulation presented at Section 5.2.1.

In the worst case scenario (see Figure 5.5), the XC/ACP ratio shows almost equal value for the two sensors when interrogated with $\Omega = 8$ GHz. Contrarily, at $\Omega = 14$ GHz the XC/ACP ratio is around 10 % better for the sensor S_1 than for sensor S_2. Therefore, a worst identification margin will be obtained in this case. Nevertheless, it is possible to see this relationship between the XC/ACP ratio and the spacing of the dual-wavelength signal as an advantage rather than a difficulty because it adds some flexibility to the interrogation scheme, i.e. with a previous simulation of the DPSS sensors arranged in the system, one can select the modulation frequency that offers better results for the specific sensing system. It also opens up the possibility to interrogate the system using different frequencies in order to enhance the response of any given sensor at each system readout.

The demodulation results obtained at 8 and 14 GHz are summarized as a function of the measurement steps in Figure 5.9. Figure 5.9 a) shows the obtained wavelength for the experiment performed with modulation frequency $\Omega = 8$ GHz; Figure 5.9 b) shows the same results with modulation frequency $\Omega = 14$ GHz. The overlap-proof behavior of the system is proved, in both experiments the sensor S_1 (represented with black circles) is temperature-swept over the sensor S_2 (red squares) showing a linear behavior with determination coefficients of $R^2_{8G} = 0.9992$ and $R^2_{14G} = 0.9997$ respectively. Which confirms the fact that the super-structured DPSS-FBG sensors maintain the sensitivity of conventional sensors, i.e. the whole structure is affected harmonically by the surrounding physical variables. Additionally, the temperature sensitivity of the sensors was computed to be 11.657 pm in Figure 5.9 a), and 11.855 pm in Figure 5.9 b), which agrees with the temperature sensitivity of conventional FBG sensors.
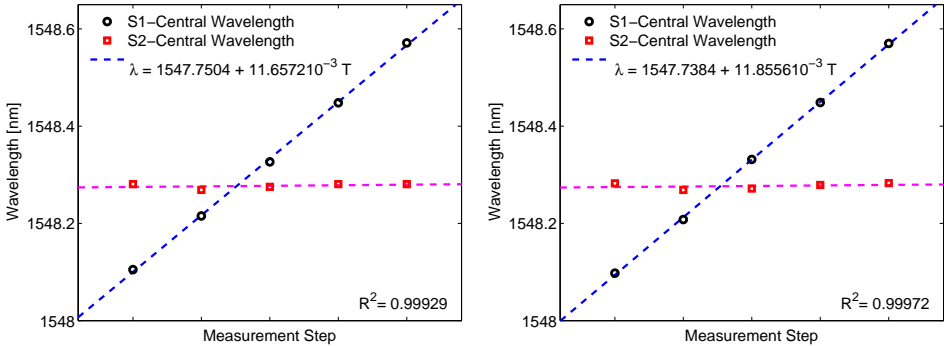
Figure 5.9: In a), the measured wavelength of two DPSS-FBG sensors in an overlapping scenario with separation of the dual-wavelength interrogating signal obtained through a modulation frequency of 8 GHz is shown, the sensor S_2 remains steady while the sensor S_1 is temperature shifted in the same operational wavelength region. b) shows the same experiment results obtained with a modulation frequency of 14 GHz. Complete identification of the two sensors is achieved under overlapping conditions.

5.4   Conclusion

In this chapter, the Discrete Prolate Spheroidal Sequences (DPSS) were proposed to shape the spectral shape of FBG sensors manufactured as superstructured FBG sensors. Taking advantage of the orthogonal nature of the DPS sequences, and also knowing that these devices are restricted to a limited bandwidth, we added the concept of code division multiplexing (CDM) to the optical fiber sensing systems. Note that this CDM concept is compatible with WDM multiplexing schemes so the scenario can be extended to CDM-WDM multiplexing networks where each DPSS-FBG sensor would have a unique spectral shape regarding the neighboring sensors that share the same WDM channel. In this way, with the simplest scheme, which allows two sensors per channel, the number of sensors deployed in the network can be doubled. In our work, we designed DPS sequences within a bandwidth of 0.8 nm thus we can guarantee CDM-WDM compatibility since all the DPSS-FBG sensors will have approximately the same bandwidth.

Simulations and experiments were performed in order to validate the feasibility of a sensing system based on the proposed sensors. Through simulation, the optical interrogation signal were found by analyzing the effect of different separation values in the dual-wavelength source over the detection ratio XC/ACP. As a result, the fixed microwave frequencies used were $\Omega = 8$ GHz.

and $\Omega = 14$ GHz. Experiments were carried out at these frequencies to show how the Ω enhances the correlation product in the measurement of certain sensors profiles. Total identification of the overlapping sensing structures has proven to be feasible, showing a worst case scenario relationship between the XC and the ACP of 60%, i.e. the maximum XC value reachs the 60% of the ACP value when the two sensors are one on top of the other spectrally.

References

[1] D. Slepian, "Prolate spheroidal wave functions, fourier analysis, and uncertainty - v: The discrete case", *Bell System Technical Journal, The*, vol. 57, no. 5, pp. 1371–1430, May 1978, ISSN: 0005-8580. DOI: `10.1002/j.1538-7305.1978.tb02104.x` (cit. on p. 100).

[2] I. B. Djordjevic, A. H. Saleh, and F. Küppers, "Design of dpss based fiber bragg gratings and their application in all-optical encryption, ocdma, optical steganography, and orthogonal-division multiplexing", *Opt. Express*, vol. 22, no. 9, pp. 10 882–10 897, May 2014. DOI: `10.1364/OE.22.010882` (cit. on p. 100).

[3] D. Pastor, C. Triana, and R. Baños, "Coherent optical en/decoding employing discrete prolate spheroidal sequences based super structured fbgs", in *Optical Communication (ECOC), 2015 European Conference on*, 2015 (cit. on p. 100).

[4] R. Baños, V. Garcia-Munoz, D. Pastor, and W. Amaya, "Rectangular Global Envelope Super Structured FBGs for Multiband Coherent OCDMA", *Photonics Technology Letters, IEEE*, vol. 25, no. 5, pp. 512–514, Mar. 2013, ISSN: 1041-1135. DOI: `10.1109/LPT.2013.2242880` (cit. on p. 102).

[5] R. Baños, D. Pastor, W. Amaya, and V. Garcia-Munoz, "Chromatic dispersion compensation and coherent direct-sequence ocdma operation on a single super structured fbg", *Opt. Express*, vol. 20, no. 13, pp. 13 966–13 976, Jun. 2012. DOI: `10.1364/OE.20.013966` (cit. on p. 102).

Chapter 6

Conclusions and future work

6.1 Conclusions

This PhD thesis is focused on the development and performance evaluation of new fiber Bragg grating devices, to be used as sensors. The main goal of the research is to endow fiber Bragg grating sensors with additional information, i.e. a specific code that characterizes each sensor in the network. In this way, a new multiplexing dimension is introduced to the sensing systems. Namely, code division multiplexing (CDM).

By designing and manufacturing customized grating-based sensors, the identity of each sensor in the network is encoded. Hence, two or more sensors are able to operate, interacting, in the same spectral range. The unique shape associated to each sensor allows the unequivocal identification of its central wavelength even under spectral overlapping between multiple sensors.

One part of this PhD thesis is devoted to the amplitude-based encoding of FBG sensors. The other part proposes the encoding of FBG sensors using both, the amplitude and phase of the devices.

6.1.1   Amplitude encoding of FBG sensors

We have developed a fiber Bragg gratings (FBGs) design methodology based on the concepts of optical code division multiple access (OCDMA) communication systems, aiming at creating a new kind of FBG sensors enhanced with additional information that can be used to identify each sensor in the network accurately.

In chapter 2, optical orthogonal codewords (OOCs) were used to tailor the amplitude shape of FBG sensors in order to provide each sensor with a distinctive code inside the network. Since the OOCs are a family of binary - mutually orthogonal codewords, the design methodology consisted in translating the binary codeword to an equi-spaced arrangement of reflection sub-bands manufactured as super-structured FBGs (SSFBGs). The main advantages of manufacturing SSFBGs devices is that all the sub-bands are manufactured at the same spatial location in the optical fiber, meaning that all the device gets affected in the same proportion by external changes in the fiber. The manufacturing of SSFBG devices with complex refractive index profile has been performed by exposing the optical fiber to an ultra violet (UV) radiation pattern using the phase-mask technique in a point by point fashion.

The main advancement we have achieved in the area of FBG sensing networks is the possibility of detecting the central wavelength of the encoded sensors when there is partial or total overlapping between their spectral shapes. By assigning each sensor in the network with a definite shape, orthogonal from neighboring sensors in the spectrum, we allow the sensors to share their working spectral range. This automatically translates into an improvement in the capacity of the network. Combining a simple code division multiplexing scheme (CDM) with the traditional wavelength division multiplexing approach (WDM) it is possible to double or triple the number of sensors deployed in the network.

The decoding process (wavelength identification of each device in the network) of the system is performed through the straightforward correlation method which basically computes the point by point product between the original amplitude shape of the sensors and the total measurement from the system (where the shape of the sensors is merged). As a result from the correlation procedure we extract the auto-correlation peak (ACP) signal, pointing at the wavelength location of each sensor. And the cross-correlation signal (XC) for the remaining locations in the spectrum where no coincidence is found. The ratio XC/ACP is the main criterion to validate the system operation. Since the design of the sensors is based on orthogonal codewords, the XC signal is constrained to a percentage of the ACP and will never reach higher values.

We have discussed the two configuration possibilities of arrangement of the sensors: serial and parallel structure. Both structures were analyzed, by means o simulation and experimental validation, from the point of view of their identification ratio (XC/ACP), regarding the main design parameters:

(a) Reflectivity
(b) Sub-bands width
(c) Sub-bands wavelength offset
(d) Codewords length

Serial configuration was proven to have a strong dependency between the XC/ACP ratio and the reflectivity of the devices. As the reflectivity increases, the detection ratio worsens because of the shadowing effect between two or more devices operating at the same wavelength. Therefore, low reflectivity values shall be considered specially for serial typologies. Both, the serial and parallel approaches are affected without distinction by the sub-bands width, in general, a 2:1 ratio was found to be a good design advice between the sub-bands distance and their width.

Another major advancement achieved in this thesis is the quantification of the error added to the network by allowing the sensors to get overlapped (XC-error). Experimentally, we have isolated the XC-error from the systemic error which is inherent to any system and is caused by noise sources, stability of the components, among others. A good figure of ~ 3 pm was obtained for the XC-error, meaning that a limited accuracy penalty should be considered in the system at the cost of multiplying its capacity.

6.1.2 *Amplitude* & *Phase encoding of FBG sensors*

Generally, bipolar codewords (with sign $\pm$ 1) offer better correlation characteristics, often with shorter codewords length, than unipolar or binary $(0, 1)$ codewords. We have extended the concept of amplitude (unipolar), developed in the first part of the thesis, to include the phase of the FBG devices as an additional codeword. Using two codewords (a_k for the amplitude and f_k for the phase components of the device) we designed a bipolar encoding methodology that translates the positive/negative features of the device into the presence or not of a phase-shift between consecutive sub-bands of the device.

In this thesis, we discuss two types of phase & amplitude encoding:

(1) *Custom designed devices:* featuring discrete phase distribution according to the phase codeword.
(2) *Discrete prolate spheroidal sequences:* complex orthogonal shapes with specific profiles in phase & amplitude.

In (1), we devised custom amplitude and phase codewords that satisfied the orthogonal properties, thus, the amplitude codeword was translated to a multi-band super-structured FBG device with reflection bands at the codeword positions marked as '1', and the phase-shift between consecutive sub-bands was interpreted in the sign of the reflection sub-bands as follows: the presence of a phase shift (i.e. (0 to π) or (π to 0)) is assigned with a negative sign, on the contrary, no phase-shift between consecutive sub-bands (i.e. (0 to 0) or (π to π)) is understood as a positive sign of the codeword.

In order to interrogate the sensors in the system and to decode properly their encoded information, an interrogation system was specially designed to evaluate the sensing network in a differential way, i.e. by using a dual-wavelength tunable source composed of two tones that are wavelength-spaced according to the spacing between the sensors sub-bands. The conception of this specific interrogation technique, is fundamental for the success of the encoding approach. Since the essence of the encoding design is the relative phase between two adjacent sub-bands, the interrogation method was designed to compute automatically the differential measurement at the fixed wavelength separation.

In Chapter 4, both aspects, the design of the sensors and their interrogation methodology were evaluated for a system with three encoded sensing devices, namely $S1, S2, S3$ by means of simulation. The results confirmed the orthogonal behavior of the system even under a total overlapping scenario between the three devices. Hence, the encoded SSFBG devices were manufactured in order to perform a validation of the proposed system in real conditions. Experimentally, we tested the interrogation setup to effectively decode the information of the sensors, i.e. the measured frequency response from the system contained the amplitude and phase information required to completely identify each sensor. Therefore, we have been able to identify the central wavelength of the sensors under overlapping conditions. The XC-error in the system was also measured to be of ~ 3.9 pm in a overlapping scenario with the three sensors.

The encoding approach based on the DPSS-FBG devices (2) is presented in Chapter 5 of this document. The main contribution of this chapter is related to the use of the dual-wavelength interrogation methodology (created for the custom sensors designed in Chapter 4) to interrogate other type of sensors

which also exhibit a complex profile in both, their amplitude and phase components. Since DPSS have been designed as a family of sequences mutually orthogonal between them with a complex profile, they are a good candidate to further investigate our interrogation technique.

Although the dual-wavelength interrogation technique was created to decode the specific sensor design of (1), it offers some flexibility that allows their use to interrogate other sensing profiles like the DPSS-FBG devices (2). We have assessed by simulation the optimal frequency separation between the two interrogating tones regarding the detection ratio when using a pair of DPSS-FBG sensors. As a result, we obtained two possible frequencies that allowed the sensors to be identified maintaining a good ratio between the XC and the ACP of their identification signals. DPSS-FBG devices were accurately manufactured with a bandwidth constrained to $\sim$ 0.8 nm and a consistent result regarding their design.

Experiments confirmed the detection feasibility for an overlapping scenario between two sensors, which thanks to the bandwidth-limited nature of the DPSS structures is easily compatible with wavelength division multiplexing schemes. Two dual-wavelength sources were selected to be experimentally tested (with distance between the two tones of 8 and 14 GHz), the experimental results confirmed the detection margins obtained in the simulation. The sensitivity and linearity of the DPSS-FBG sensors was confirmed to be analogous to that of conventional FBG sensors.

6.2   Future work

The encoding of FBG-based devices reported in this thesis has demonstrated the possibility to increase the number of sensors by combining the proposed code division multiplexing methodology with the traditional wavelength division multiplexing approach. Still, there are many open questions that can be addressed, these open lines include:

- Explore the implementation of alternative unipolar codewords families to encode sensing devices in amplitude (to be interrogated with a broadband source).

- Improve the simulation platform to eventually include larger WDM + CDM scenarios, with the ability to interactively select the placement and encoding scheme of the sensors.

- Develop a miniaturized and cost effective version of the interrogation schemes carried out in this thesis which were implemented in the laboratory. It is of special interest to develop a cost-effective version of the dual-wavelength tunable interrogation setup presented in Chapter 4.

- Explore the implementation of additional phase and amplitude encoding schemes by using different encoding approaches.

- Implement an in-situ measurement system using the proposed encoding techniques to evaluate their performance in real life operation.

- Further study and improve the performance of the presented sensors in terms of accuracy, resolution or operational range.

List of publications

6.3 Journal papers

[1] A. Triana, D. Pastor, and M. Varón, "Code division multiplexing applied to fbg sensing networks: Fbg sensors designed as discrete prolate spheroidal sequences (dpss-fbg sensors)", *Journal of Lightwave Technology*, vol. 35, no. 14, pp. 2880–2886, Jul. 2017, ISSN: 0733-8724. DOI: `10.1109/JLT.2017.2705283`.

[2] A. Triana, D. Pastor, and M. Varón, "A code division design strategy for multiplexing fiber bragg grating sensing networks", *Sensors*, vol. 17, no. 11, 2017, ISSN: 1424-8220. DOI: `10.3390/s17112508`.

[3] A. Triana, D. Pastor, and M. Varon, "Overlap-proof fiber bragg grating sensing system using spectral encoding", *IEEE Photonics Technology Letters*, vol. 28, no. 7, pp. 744–747, Apr. 2016, ISSN: 1041-1135. DOI: `10.1109/LPT.2015.2508743`.

[4] C. A. Triana, D. Pastor, and M. Varón, "Enhancing the multiplexing capabilities of sensing networks using spectrally encoded fiber bragg grating sensors", *Journal of Lightwave Technology*, vol. 34, no. 19, pp. 4466–4472, Oct. 2016, ISSN: 0733-8724. DOI: `10.1109/JLT.2016.2537362`.

[5] ——, "Optical code division multiplexing in the design of encoded fiber bragg grating sensors", *Optica pura y aplicada*, vol. 49, no. 1, pp. 17–28, Feb. 2016, ISSN-e 2171-8814. DOI: `10.7149/OPA.49.1.17`.

6.4   Conference papers

[1] D. Pastor, C. Triana, and R. Baños, "Coherent optical en/decoding employing discrete prolate spheroidal sequences based super structured fbgs", in *Optical Communication (ECOC), 2015 European Conference on*, 2015.

[2] C. A. Triana and D. Pastor, "Optical codification employing discrete prolate spheroidal sequences", in *Proc. IX Reunión Española de Optoelectrónica Optoel2015*, 2015.

[3] C. A. Triana, M. Varon, and D. Pastor, "Spectrally encoded fibe bragg grating sensors using optical code division multiplexing", in *Proc. IX Reunión Española de Optoelectrónica Optoel2015*, 2015.

[4] C. A. Triana, M. Varón-Durán, and D. Pastor, "Fibre bragg grating sensor interrogation system using a vcsel and correlation techniques", in *2015 European Conference on Lasers and Electro-Optics - European Quantum Electronics Conference*, Optical Society of America, 2015.

[5] C. Triana, M. Varón, and D. Pastor, "Optical code division multiplexed fiber bragg grating sensing networks", in *Proc. SPIE, 24th International Conference on Optical Fibre Sensors*, vol. 9634, 2015, pp. 963478-963478-4. DOI: `10.1117/12.2194995`.

[6] C. A. Triana, G. A. Á. Botero, M. Varón, and D. Pastor, "Determining the temperature performance of encoded fiber bragg grating sensors", in *Latin America Optics and Photonics Conference*, Optical Society of America, 2016, LW2C.4. DOI: `10.1364/LAOP.2016.LW2C.4`.

[7] C. A. Triana, M. Varon, and D. Pastor, "Interrogation of fiber bragg grating sensors using a vcsel and correlation techniques", in *Proc. SPIE, 24th International Conference on Optical Fibre Sensors*, 2015.

[8] C. Cano, F. Galarza, J. D. Cepeda, C. A. Triana-Infante, C. A. Perilla, M. Varon, and D. Pastor, "Reliability of strain and temperature measurements based on fiber bragg gratings sensors in the early age of concrete shrinkage", in *Latin America Optics and Photonics Conference*, Optical Society of America, 2014, LTu4A.23.